MReadings: Prostate MRI

Contributions from our MAGNETOM users

siemens-healthineers.com/magnetom-world

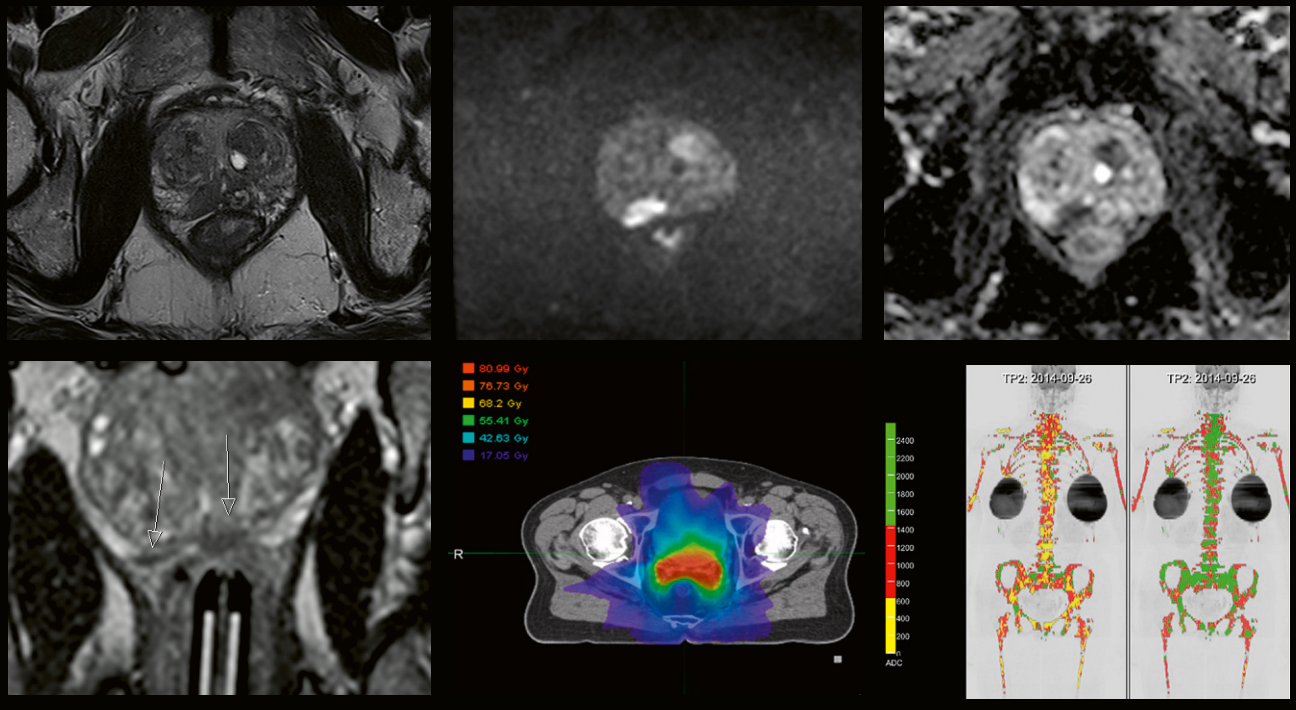

Prostate cancer care pathway

Screening & Early Detection → Diagnosis & Therapy Decision → Treatment Planning & Delivery → Follow-up & Survivorship

SIEMENS Healthineers

Elisa Roccia, Ph.D.
Global Segment Manager Oncology

MReadings: Prostate MRI

Dear Readers,

This edition of **MReadings: Prostate MRI** is dedicated to exploring the MR solutions and innovations that have improved and continue to improve each step of the prostate cancer patient pathway. You will have the opportunity to learn about success stories from the radiology and radiation oncology departments of eight different countries, highlighting the impact of MR technology on prostate cancer diagnosis, treatment planning, and patient outcomes.

If we look at **Screening & Early Detection**, a significant breakthrough has been the integration of multiparametric MRI to screen men prior to biopsy. Evidence has shown that such an approach can reduce the number of unnecessary biopsies and increase the detection of clinically significant cancers. This has resulted in a shift towards more personalized and targeted approaches to prostate cancer diagnosis and management, but also in an increased demand for prostate MRI exams. Solutions like assisted scanning and deep learning-based image reconstruction can deliver high-quality and standardized MRI exams in radically shortened acquisition times, helping to address the challenge of increasing referrals and staff shortages, with the aim of achieving operational excellence.

The increased demand for multiparametric MRI exams comes hand in hand with an increased workload in reading and interpretation. Fortunately AI-based solutions for automatic lesion detection and classification[1] have now entered the scene in the **Diagnosis & Therapy Decision** step, showing how radiologists and AI can work together to reduce reading times and inter-reader variability.

Beyond making the initial diagnosis, MRI has also tremendously gained relevance in the management of the disease. In recent years, there have been numerous success stories on the integration of MRI into the radiotherapy workflow. Indeed, the use of MRI in radiotherapy planning has revolutionized the way **Treatment Planning & Delivery** are performed, enabling clinicians to visualize and contour tumors with confidence.

In the **Follow-up & Survivorship** step of the pathway, it is instrumental to accurately monitor patients undergoing treatments such as chemotherapy or hormonal therapy. Quantitative tools based on whole body diffusion-weighted imaging offer the possibility to visualize functional changes, which enables to assess in a timely manner if a treatment is effective or if it is necessary to change the therapeutic approach. This opens up new possibilities for improving patient outcomes and quality of life, paving the way for more targeted and personalized approaches to cancer care.

In summary, the field of MRI remains dynamic and ever evolving, with new breakthroughs that improve cancer patient outcomes and transform the system of care.

We are very grateful to the authors for sharing their expertise, experience, and enthusiasm with other MAGNETOM users.

I wish you all an enjoyable read!

Elisa Roccia

[1] *The product is not commercially available in some countries, e.g., the U.S. Due to regulatory reasons their future availability cannot be guaranteed. Please contact your local Siemens Healthineers organization for further details.*

Prostate cancer care pathway

Screening & Early Detection

Diagnosis & Therapy Decision

Treatment Planning & Delivery

Follow-up & Survivorship

The Prostate Dot Engine – a System-Guided and Assisted Workflow to Improve Consistency in Prostate MR Exams

Wilhelm Horger, Gregor Thoermer, Elisabeth Weiland, Bernd Kuehn, Berthold Kiefer

Siemens Healthineers, Magnetic Resonance Imaging, Erlangen, Germany

The "PROMISe" of mpMRI

PROMIS, PRECISION, 4M and MRI-FIRST [1–4] are four landmark studies that are changing the way we screen for prostate cancer.

Evidence presented in these studies has already impacted guidelines on imaging prostate cancer issued by the European Association of Urology and national guidelines in the UK (NICE) and the Netherlands toward a scheme where prostate MRI serves a first-line triage test in biopsy-naïve men with elevated PSA levels.

These studies consistently provide Level 1A evidence that using multiparametric MRI (mpMRI) of the prostate can reduce the number of biopsies required in men with elevated PSA levels.

Due to the excellent negative predictive value of prostate mpMRI, men without suspicious MRI findings do not require further examinations. At the same time, the mpMRI pathway does not result in an under-detection of clinically significant cancer, but will reduce the number of clinically insignificant cancers picked up by chance in a "systematic TRUS-biopsy-only" care scheme (see Table 1). It has been shown for – quite differently organized – healthcare systems that the MRI pathway will reduce the overall healthcare expenditure per clinically significant cancer diagnosed. This advantage is largely driven by the reduced number of biopsies [5–7], resulting in fewer infections and sepsis, the latter presenting a huge financial burden [8]. The potential long-term effects on patient management of reduced detection of clinically insignificant disease have not even been modelled in studies of this kind.

Performance of mpMRI pathway in comparison with TRUS-bx pathway	PRECISION[1] (500 men)	MRI-FIRST[2]	4M Study[3]	PROMIS[4]
Avoid biopsy after negative mpMRI in (%) of patients	28 %	18 – 21 %	49 %	27 %
Increase in detection of significant cancers (%)	+12 %	No difference in significant cancer (+2 %)	No difference in significant cancer (+2 %)	No difference in significant cancer (+2 %)
Diagnosis of insignificant cancer	-13 %	-14 %	-11 %	-5 %
Reduction of biopsy cores per patient (relevant for infections and side effects	11 → 4 (= -64 %)	12 → 3 (= -75 %)	12 → 3 (= -75 %)	n.a.

Table 1: Summary of recently published landmark mpMRI prostate cancer detection studies and their impact on patient management.

The challenge in scaling up mpMRI

Expert panels are, however, aware that the MRI pathway puts an additional burden on radiologists and imaging providers and the potential risks and challenges associated with the increasing demand. Most radiologists have limited expertise in interpreting and reporting prostate MRI, and the consistent acquisition of high-quality mpMRI prostate examinations is a challenge for technologists not used to performing the exam routinely according to the PI-RADS recommendations.

In 2019, Engels et al. [9] and Barrett et al. [10] published excellent papers on how to perform high-quality mpMRI and which pitfalls to consider. They concluded that training of skilled professionals is key; but also that imaging vendors should provide tools and workflows that help tailor and optimize the exam for the individual patient, to maximize scan quality and consistency.

Respective software automatically detecting characteristic landmarks with machine learning trained algorithms to adjust size and angulation of FOVs to the individual anatomical conditions with high consistency and reproducibility has been successfully established for various applications, literarily ranging from head to toe with the Brain, Spine, Hip, Knee, Breast, Cardiac, Abdomen, and Whole-Body Dot Engines. Studies specifically investigating the value of such software for assisted and guided brain, liver and whole-body examinations have clearly shown relevant reduction of examination time compared to standard workflows [11–13]. In addition, for liver examinations, assisting features including automated bolus detection (ABLE) with an automatically positioned bolus tracker in the descending aorta allow technologists to achieve optimal arterial phase quality in dynamic contrast-enhanced scans in 94% of cases, where a fixed-time approach only achieves 73% of optimally timed arterial phase images [12].

Prostate Dot Engine – from prototype to product

Such novel automated scanner software has recently been prototyped and evaluated for MRI examinations of the prostate. The aim is to standardize scan volume positioning, tilting and coverage, in order to ensure high consistency between operators, and to better support Active Surveillance with repeated MR scans [14]. Although the evaluation did not show a statistically significant time advantage of the assisted workflow over the manual workflow (26 versus 28 minutes median examination time), the overall imaging quality was superior with the assisted MRI scans, achieving an average rating of 4.6 out of 5 versus 3.8 out of 5 points for the manual workflow.

In the light of developing evidence and changing guidelines, the planned introduction of the Prostate Dot Engine as part of the software version *syngo* MR XA30A is timely.

The Prostate Dot Engine is designed for fast, reproducible and standardized prostate MR examinations and supports multi-parametric, multi-plane MR imaging according to the latest PI-RADS v2.1 recommendations [15]. The operator is guided through one comprehensive workflow with decision points to adapt the strategy to individual patient conditions (see Figure 1), while artificial intelligence aids in planning and performing the procedure steps.

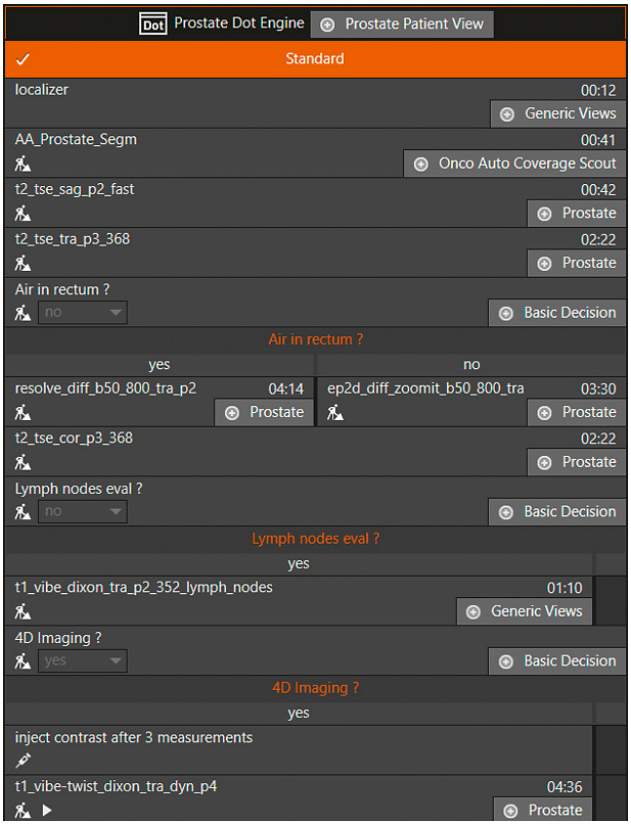

1 Workflow of the Prostate Dot Engine with different decision points.
For example, based on initial morphological scans the operator may be asked to decide whether a patient has a lot of gas in the rectum. If there is considerable gas, a highly robust RESOLVE DWI scan is acquired. If not, zoomed diffusion-weighed images are acquired. These are more prone to distortions, but offer higher spatial resolution and better contrast in shorter time.

AI-assisted planning, angulation, and coverage

Before image acquisition, the operator has the choice between two general approaches for acquiring the data. In "Patient View" (Fig. 2) slice orientation can be chosen to be either "Anatomical" or "Axial". Anatomical means that the acquisition volumes are tilted to match the actual, individual angulation of the prostate in the body, which can be affected by factors such as bladder and rectal filling, or how the patient lies on the bed. Most recommendations and committees suggest acquiring either axial scans "perpendicular to the long axis of the prostate" or "true axial" images, the latter aimed at improving reproducibility in Active Surveillance [9, 15, 16].

A recent study has investigated the robustness of AI-derived axial slice angulation with the Prostate Dot Engine. Subjects underwent MRI scans of the prostate with full and empty bladder, with excellent reproducibility of the angulation [17], indicating that the assisted planning approach might increase consistency in Active Surveillance without compromising fidelity in anatomical coverage. The preferred angulation strategy can be predefined and set as a default, so it does not have to be selected in every patient.

The short AutoAlign prostate segmentation scan at the beginning of the exam facilitates the detection of certain landmarks in the small pelvis to derive the angulation and coverage required for the subsequent mpMRI of the prostate. For the angulation, the entry point of the bladder neck into the prostate and the exit of the urethra from the apex of the prostate are used as highly reproducible landmarks. In addition, the prostate gland is automatically segmented, and if the PSA value has been specified an estimate of PSA density (ng/ml) is provided in the generated report. Another feature of the Prostate Dot Engine is to support asymmetric anatomical coverage or a shift in the field-of-view direction as illustrated in Figure 3.

By default, images in the sagittal plane are acquired before the axial T2-weighted and diffusion-weighted images. This approach has repeatedly been reported to be beneficial as it gives the patient some time to relax and calm down, so they are less likely to move during the most relevant axial scans.

Diffusion-weighted imaging

After acquiring T2-weighted images in sagittal and transverse orientation, diffusion-weighted images are automatically pre-planned and acquired, using either RESOLVE or a

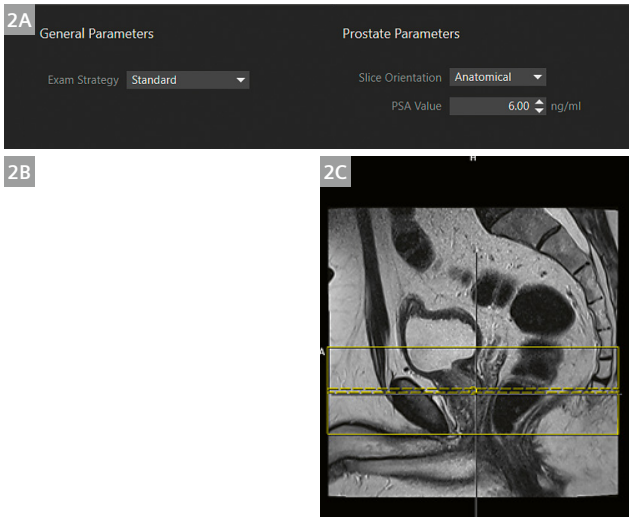

2 The Patient View of the Prostate Dot Engine **(2A)** is displayed before the examination. The operator can specify the desired slice orientation ("Anatomical" or "Axial"), which will result in the acquisition orientations shown in **2B** and **2C**, respectively. Coronal and sagittal acquisitions are acquired perpendicular to the chosen axial orientation. The PSA value can be entered in order to get an automated estimation of the PSA density.

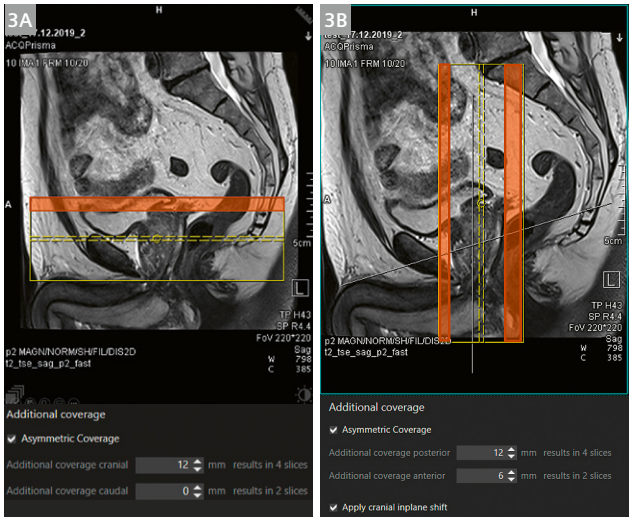

3 Based on the segmentation of the prostate gland, the required number of slices to cover the entire organ is automatically derived and adjusted. In particular with straight axial acquisitions, the seminal vesicles may expand more in the cranial direction than the prostate base **(3A)**. To ensure complete coverage of the seminal vesicles, the user interface allows to specify additional "asymmetric coverage", for example with 4 more slices in the cranial direction (corresponding to the orange area). The same can also be applied to other orientations, e.g., to coronal planes **(3B)**. In addition, a FOV shift to better cover lymph nodes in the small pelvis can be achieved by ticking the option "Apply cranial inplane shift" thus ending the FOV 5 cm below the apex of the prostate.

single-shot EPI method with reduced FOV (ZOOMit^{PRO}). The strengths of both techniques are specified in Table 2 and an illustrative case can be found in Figure 4.

Following the PI-RADS v2.1 recommendation, two *b*-values (b = 50 s/mm^2 and b = 800 s/mm^2) are scanned and ultra-high *b*-value images at b = 1400 s/mm^2 are automatically calculated. The often-suggested additional acquisition of a supporting *b*-value in the range of 400–500 s/mm^2 for improved ADC calculation is not recommended here, since a linear fitted ADC value is hardly influenced by this choice and the scan time may more effectively be invested in additional averages at the higher *b*-value.

With regards to the ultra-high *b*-value (> 1400 s/mm^2) there is some disagreement in the international community whether to acquire or extrapolate images, and on the optimal choice of the ultra-high *b*-value [18]. UK consensus guidelines are most specific in proposing b ≥ 1400 s/mm^2 at 1.5T and b ≥ 2000 s/mm^2 at 3T, both "preferentially acquired". Rosenkrantz et al. [20] provide some guidance on the choice of an optimal *b*-value, suggesting that "computed *b*-values in the range of 1500–2500 s/mm^2 (but not higher) are optimal for prostate cancer detection" providing high sensitivity for lesions and sufficient anatomical clarity.

The Prostate Dot Engine provides a flexible framework where protocol steps can be modified and added to best serve individual institutional expectations.

Dynamic contrast-enhanced imaging

After acquiring diffusion-weighted and coronal T2-weighted images, T1-weighted scans of the small pelvis and dynamic contrast-enhanced (DCE) images may be acquired. Some studies [20, 21] suggest that the detection rate of clinically significant cancer may not be negatively affected with a bi-parametric screening protocol, but the detection rate of insignificant cancer and the number of biopsies may go up due to a tendency to upgrade indecisive cases without DCE information. On the other hand, bi-parametric protocols have the clear advantage of being completely non-invasive and substantially shorter, there-

	ZOOMit^{Pro}	RESOLVE
TE (ms)	72	51
FOV (mm x mm)	100 x 100	200 x 200
Resolution (mm^3)	0.82 x 0.82 x 3.0	0.85 x 0.85 x 3.0
Acquisition time (min:sec)	3:30	4:14

Table 2: Comparison of protocol parameters of ZOOMit^{Pro} and RESOLVE with b = 50, 800 s/mm^2 at 3T (MAGNETOM Prisma). While ZOOMit provides higher SNR and resolution in shorter acquisition time, the readout segmented RESOLVE is more robust in patients with susceptibility issues (especially caused by gas in rectum) due to a substantially shorter echo train.

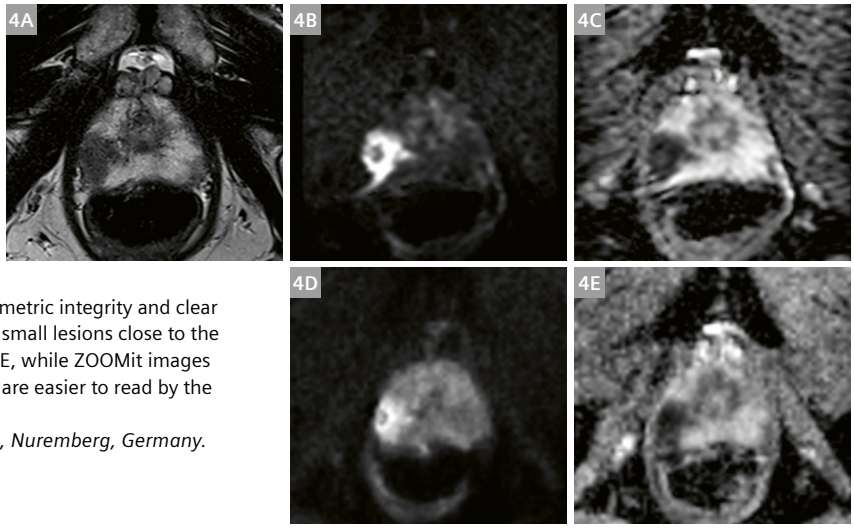

4 72-year-old patient with suspected prostate cancer. A clearly visible lesion in the right peripheral zone in the apical aspect of the prostate **(4A)** represented with a corresponding diffusion restriction in calculated high *b*-value images and ADC maps. Due to a substantial amount of gas in the rectum, ZOOMit images **(4B, D)** suffer from a distortion in phase-encoding-direction (here: L-R), sometimes also referred to as "comet tail sign" while the RESOLVE images **(4C, E)** expose high geometric integrity and clear lesion delineation. It can be argued that very small lesions close to the capsule may only be seen properly in RESOLVE, while ZOOMit images appear to have higher lesion conspicuity and are easier to read by the radiologists.
Images courtesy of Prof. Karlheinz Engelhard, Nuremberg, Germany.

fore more cost efficient. While the role of DCE in prostate cancer detection is debated and may be subject to change in a later version of PI-RADS, DCE remains integral part of PI-RADS v2.1 conform mpMRI for now. This is also reflected in the workflow of the Prostate Dot Engine: by default, DCE imaging is included but may be deselected (i.e. in follow-ups) or removed if this is the institutional preference. As for the other scans, positioning of the imaging volume is automatically adjusted and imaging parameters, such as temporal and spatial resolution, are kept constant to fulfill the requirements of the PI-RADS standard.

Summary

The Prostate Dot Engine aims to standardize mpMRI of the prostate, to assist less experienced users in performing the scans with consistent high quality, and to facilitate high reproducibility in repeated scans, for example in Active Surveillance. The Prostate Dot Engine is one of several intelligent solutions designed to scale up prostate MRI in the light of a globally rising demand for this procedure.

References

1 Kasivisvanathan V, Rannikko AS, Borghi M, et al. PRECISION Study Group Collaborators. MRI-Targeted or Standard Biopsy for Prostate-Cancer Diagnosis. N Engl J Med. 2018;378(19):1767-1777.
2 Rouvière O, Puech P, Renard-Penna R, et al. Use of prostate systematic and targeted biopsy on the basis of multiparametric MRI in biopsy-naive patients (MRI-FIRST): a prospective, multicentre, paired diagnostic study. Lancet Oncol 2018; http://dx.doi.org/10.1016/S1470-2045(18)30569-2.
3 van der Leesta M, Cornelb E, Israëla B, et al. Head-to-head comparison of transrectal ultrasound guided prostate biopsy versus multi-parametric prostate resonance imaging with subsequent MR-guided biopsy in biopsy-naïve men with elevated PSA; a large prospective multicenter clinical study. Eur Urol. 2018; in press.
4 Ahmed HU, El-Shater Bosaily A, Brown LC, et al. Diagnostic accuracy of multi-parametric MRI and TRUS biopsy in prostate cancer (PROMIS): a paired validating confirmatory study. Lancet. 2017;389: 815–22.
5 de Rooij M, Crienen S, Witjes JA, et al. Cost-effectiveness of magnetic resonance (MR) imaging and MR-guided targeted biopsy versus systematic transrectal ultrasound-guided biopsy in diagnosing prostate cancer: a modelling study from a health care perspective. Eur Urol. 2014;66(3):430-436.
6 Pahwa S, Schlitz NK, Ponsky LE, et al. Cost-effectiveness of MR Imaging-guided Strategies for Detection of Prostate Cancer in Biopsy-Naive Men. Radiology. 2017;285(1):157-166.
7 Faria R, Soares MO, Spackman E, et al. Optimising the Diagnosis of Prostate Cancer in the Era of Multiparametric Magnetic Resonance Imaging: A Cost-effectiveness Analysis Based on the Prostate MR Imaging Study (PROMIS). Eur Urol. 2018;73(1):23-30. doi: 10.1016/j.eururo.2017.08.018. Epub 2017 Sep 19.
8 Gross MD, Alshak MN, Shoag JE, et al. Healthcare Costs of Post-Prostate Biopsy Sepsis. Urology. 2019;133:11-15.
9 Engels RRM, Israël B, Padhani AR, et al. Multiparametric Magnetic Resonance Imaging for the Detection of Clinically Significant Prostate Cancer: What Urologists Need to Know. Part 1: Acquisition. Eur Urol. 2019 in press; DOI: https://doi.org/10.1016/j.eururo.2019.09.021.
10 Caglic I, Barrett T. Optimising prostate mpMRI: prepare for success. Clin Radiol. 2019 ;74(11):831-840.
11 Moenninghoff C, Umutlu L, Kloeters C, et al. Workflow efficiency of two 1.5T MR scanners with and without an automated user interface for head examinations. Acad Radiol. 2013;20(6):721-30.
12 Sharma P, Kalb B, Kitajima HD, et al. Optimization of single injection liver arterial phase gadolinium enhanced MRI using bolus track real-time imaging. J Magn Reson Imaging. 2011;33(1):110-8.
13 Stocker D, Finkenstaedt T, Kuehn B, et al. Performance of an Automated Versus a Manual Whole-Body Magnetic Resonance Imaging Workflow. Invest Radiol. 2018;53(8):463-471.
14 Esser M, Zinsser D, Kündel M, et al. Performance of an Automated Workflow for Magnetic Resonance Imaging of the Prostate: Comparison With a Manual Workflow. Invest Radiol. 2019. doi: 10.1097/RLI.0000000000000635
15 American College of Radiology. PI-RADS® Prostate Imaging – Reporting and Data System 2019, Version 2.1. https://www.acr.org/-/media/ACR/Files/RADS/Pi-RADS/PIRADS-V2-1.pdf
16 Appayya MB, Adshead J, Ahmed HU. National implementation of multi-parametric magnetic resonance imaging for prostate cancer detection – recommendations from a UK consensus meeting. https://doi.org/10.1111/bju.14361.
17 Cui Y, Han S, Li C, et al. Performance and Reproducibility of a Day Optimizing Throughput (Dot) Workflow Engine in Automated Prostate MRI Positioning. Proceedings of the 28th Annual Meeting of the ISMRM, Abstract No. #4546.
18 Kordbacheh H, Seethamraju RT, Harisinghani MG, et al. Image quality and diagnostic accuracy of complex-averaged high b value images in diffusion-weighted MRI of prostate cancer. Abdominal Radiology. 2019 June;44(6):2244-2253.
19 Brizmohun AM, Adshead J, Ahmed HU, et al. National implementation of multi-parametric magnetic resonance imaging for prostate cancer detection – recommendations from a UK consensus meeting. BJU Int. 2018;122:13-25. https://doi.org/10.1111/bju.14361.
20 Rosenkrantz AB, Parikh N, Kierans AS, et al. Prostate Cancer Detection Using Computed Very High b-value Diffusion-weighted Imaging: How High Should We Go? Acad Radiol. 2016;23(6):704-11.
21 Kuhl CK, Bruhn R, Krämer N, et al. Abbreviated Biparametric Prostate MR Imaging in Men with Elevated Prostate-specific Antigen. Radiology. 2017;285(2):493-505.
22 Van der Leest M, Israël B, Cornel EB, et al. High Diagnostic Performance of Short Magnetic Resonance Imaging Protocols for Prostate Cancer Detection in Biopsy-naïve Men: The Next Step in Magnetic Resonance Imaging Accessibility. Eur Urol. 2019;76(5):574-581.

Contact

Wilhelm Horger
MR Application Development
Siemens Healthineers
wilhelm.horger@siemens-healthineers.com

Optimization of Pre-biopsy bp-MRI of the Prostate

Lynn Doy[1]; Niall MacKenzie[1]; Salman A. Siddiqui[1]; Gautham Mukerjhee[2]; Rebecca Sands[1]

[1]Department of Radiology, North West Cancer Centre, Altnagelvin Area Hospital, Londonderry, Northern Ireland
[2]Department of Radiotherapy Physics, North West Cancer Centre, Altnagelvin Area Hospital, Londonderry, Northern Ireland

Interprofessional teamwork and collaboration between diagnostic and therapeutic radiographers in the evolution of an MR radiotherapy-planning (MR RTP) service was pivotal to the success of this study, and to the eventual implementation of our current standard prostate-imaging protocol.

Key points

- Escalating demands in the early diagnosis and management of prostate cancer is placing considerable pressure on MRI departments across the UK.
- Adopting a combined approach to image optimization and investing in both technical and patient-related aspects to reduce artifacts can improve image quality and reduce scan times.
- Learning experiences in the development of an MR RTP service led to research to ascertain whether adminstration of a micro-enema before prostate imaging could influence image interpretation in diagnostics.
- Micro-enema administration demonstrates a significant benefit to image quality in bp-MRI of the prostate and should be considered as an integral part of the imaging procedure.

Introduction

Prostate cancer is now the most common malignancy in men and the second leading cause of cancer in the UK [1]. The clinical behavior of prostate cancers can range from low-grade cancers that do not progress to lethal disease, to invasive tumors that rapidly progress and become metastatic [2]. With the incidence of prostate cancer expected to double by 2030 [3], early diagnosis of clinically significant disease, performed at reasonable cost and in achievable time frames, is of increasing importance.

The publication of the Prostate Imaging Reporting and Data System (PI-RADS) in 2012 [4] brought together the importance of standardizing optimal sequences, now widely known as multi-parametric MRI (mp-MRI), with structured reporting systems to aid interpretation and diagnostic evaluation of the prostate. The publication of PI-RADS v2 in 2015 [5] aimed to further standardize image acquisition and interpretation in mp-MRI, providing guidance on technical optimization, detailing the minimal acceptable sequences and parameters in image acquisition, with the current emphasis on the more widely available sequences. Accurate interpretation and staging of disease with mp-MRI is now considered to play an additional key role in identifying prognostic factors, such as extracapsular extension, seminal vesicle extension, and lymphovascular invasion. These significant image findings indicate a higher risk of recurrence [2], aiding in risk

stratification of cases and defining optimal treatment pathways for the large cohort of diagnosed patients.

Pre-biopsy mp-MRI now plays a central role in the management pathway of prostate cancer in the UK, being performed on up to 75% of men with a clinical suspicion of prostate cancer [6], so it is essential that diagnostic mp-MRI of the highest quality is increasingly accessible.

PI-RADS v2 does acknowledge that there are many challenges in achieving standardization of image acquisition. Equipment availability and capability, patient factors, and radiology interpretation all differ across imaging sites. To achieve excellence in clinical performance, diagnostic processes need to be robust, encompassing high-quality imaging by radiographers and accurate image interpretation by radiologists working together with urologists in multidisciplinary teams.

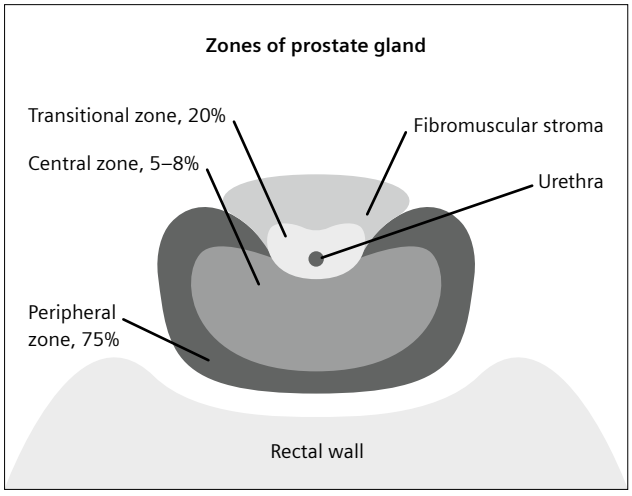

1 Anatomy of the zones of the prostate gland: schematic diagram in transverse plane with rectal wall at posterior aspect.

Zonal anatomy and key sequences

At least 75% of all prostate cancers occur in the peripheral zone (PZ), but when differentiating benign and malignant disease, and determining prognostic factors, special attention should also be given to the transitional zone (TZ), prostate capsule, seminal vesicles, neurovascular bundles, and rectoprostatic angles to identify any extracapsular extension [7]. Zonal anatomy of the prostate gland and MRI appearances of extracapsular structures are shown in Figures 1 and 2, respectively.

Sequence choice in prostate MRI is widely debated, but T2-weighted (T2W) high-resolution imaging is considered to be the preferable sequence for local staging and identification of cancers in the TZ, as it also identifies the presence of extracapsular extension and seminal vesicle involvement [7]. Diffusion-weighted imaging (DWI) provides functional information based on the tissue cellularity, measuring the movement of water molecules within tissue. DWI is considered to be the best-performing sequence for detection of cancers in the PZ, with a restricted water diffusion playing a key role in defining

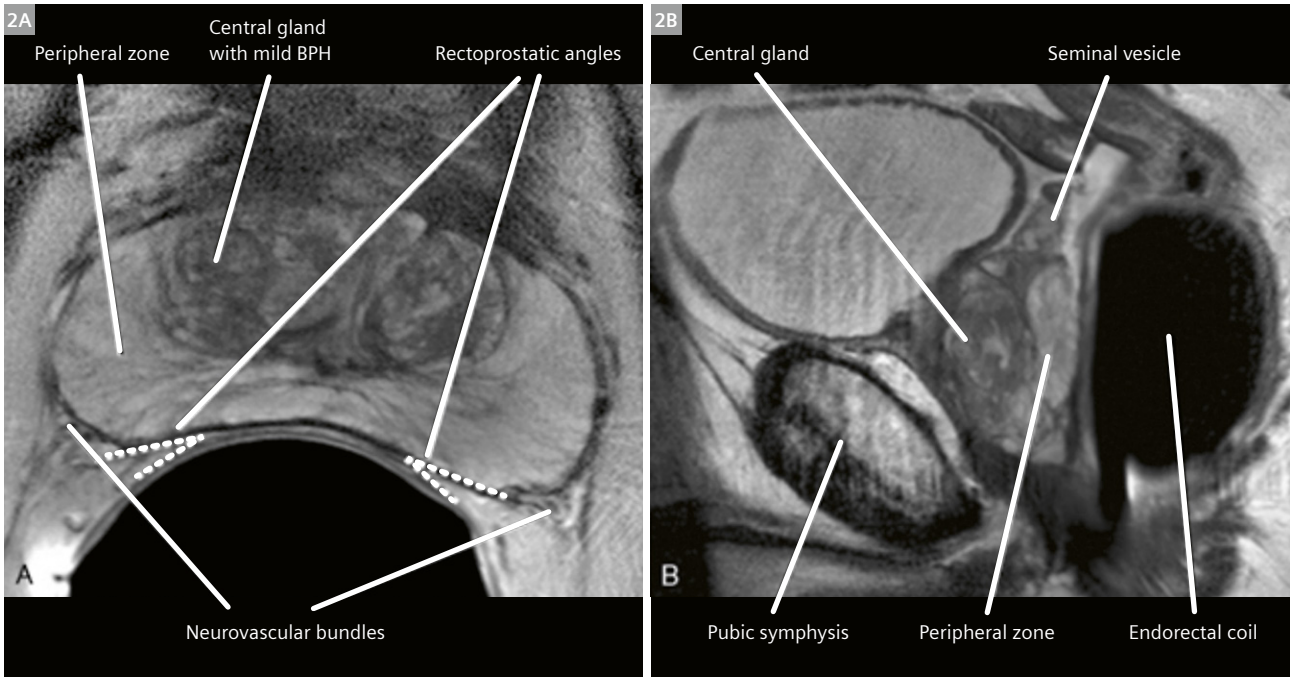

2 MR images of extracapsular structures: **(2A)** sagittal T2W and **(2B)** axial T2W showing anatomical landmarks.
Reproduced with permission from https://radiologykey.com/male-reproductive-system-2.

high-grade cancers [7]. PI-RADS v2.1, which was published in 2019 [8], now places most emphasis on DWI for PZ lesions and on T2W for TZ lesions; additional sequences like dynamic contrast-enhanced (DCE) are considered to play a limited role in lesion characterization, and MR spectroscopy is considered to be impractical for widespread use. As such, the term bi-parametric MRI (bp-MRI) is rapidly gaining favor, and although effectively reducing overall examination time, achieving a fully optimized examination becomes even more important to the overall clinical outcome.

Combined approach to optimization

As MR radiographers working as an integral part of a multidisciplinary approach to cancer services, we must ensure that image quality is of the highest standard we can achieve, whilst also managing increasing clinical demand, often with limited scanner capability or resources. We have an array of tools at our disposal to optimize image quality. Primarily we consider image optimization to be technical in its approach, aiming to utilize a vast choice of sequences and imaging parameters to achieve artifact-free, high SNR and high-resolution images in reasonable scan times to provide good clinical outcomes, but this can be very dependent on the capability of the equipment available.

However, an important, yet often forgotten factor in overall image optimization can be the patient themselves. In prostate imaging, patient-related factors can be anything from gross patient movement or bowel peristalsis, to air and feces within the rectum. By addressing patient-related issues that may affect overall image quality due to artifacts or distortion, we can directly improve outcomes for our patients. The rest of this article will look at using a combined approach to image optimization.

Technical optimization of sequences

In focusing our efforts on bp-MRI only, it is imperative that the key sequences are fully optimized. The MAGNETOM Aera 1.5T system can easily achieve PI-RADS v2-compliant sequences in terms of SNR and resolution, but some specific sequence and parameter options are worth further consideration to ensure consistency across a wide range of patients.

All T2W and DWI sequences utilize GRAPPA to reduce scan times with relatively little compromise in SNR.

Where administration of an antispasmodic is contraindicated and the risk of motion artifacts from bowel movement is increased, T2W sequences are simply acquired with a lower resolution for speed, and interpolation is chosen to increase the apparent resolution. This has proved to be a robust alternative to BLADE, with radiology being more confident when tissue contrast is consistent with our standard protocol.

In DWI, distortion from metallic implants[1] may prove problematic. EPI sequences are usually preferred as they are more readily available and have the advantage of a higher SNR than some alternatives. However, in patients where distortion from metallic implants – e.g., total hip replacement (THR) – cannot be avoided, options like RESOLVE DWI may be preferred to take advantage of the superior distortion reduction and hopefully provide some correlation with the image appearances of T2W lesions.

Choice of b-value in DWI is widely debated, with longer b-values ≥ 1400 s/mm^2 being considered optimal in prostate imaging. Some systems will have the option to calculate or extrapolate higher b-value images from multiple acquired data sets with lower b-values and higher SNR. However, Grant et al. [9] conclude that the image quality of calculated high b-value DWI relative to corresponding acquired DWI decreases with an increase in b-value, and the radiology preference in our department is to invest in acquiring data with a b-value of 1400 s/mm^2.

Reduction of patient-related artifacts

Bowel peristalsis: The use of anti-peristaltic drugs to reduce artifacts from bowel movement in the pelvis and abdomen does have implications for the overall service: There are additional costs to consider, additional time is required for cannulation, and medical support is often needed for administration and prescription. However, Slough et al. [10] conclude that the IV administration of hyoscine butylbromide (HBB) immediately prior to MRI significantly improves the image quality of T2W images, a key sequence in mp-MRI. They advocate its use in routine patient preparation prior to prostate MRI, with the acquisition of T2W sequences during a short window of effectiveness, usually approximately 20 minutes.

Rectal distention: There is wide acceptance in diagnostic MRI that an air-filled rectum can lead to considerable geometric distortion on DWI at air-tissue interfaces. Recent publications [11, 12] discuss the negative impact that rectal distention and loading can have on the quality of both T2W and DW images. Caglic et al. [12] propose the use of bowel preparation prior to prostate mp-MRI to optimize image quality. However, they also note that PI-RADS v2 highlights a lack of evidence to specifically inform on patient preparation prior to mp-MRI.

[1] *The MRI restrictions (if any) of the metal implant must be considered prior to patient undergoing MRI exam. MR imaging of patients with metallic implants brings specific risks. However, certain implants are approved by the governing regulatory bodies to be MR conditionally safe. For such implants, the previously mentioned warning may not be applicable. Please contact the implant manufacturer for the specific conditional information. The conditions for MR safety are the responsibility of the implant manufacturer, not of Siemens Healthineers.*

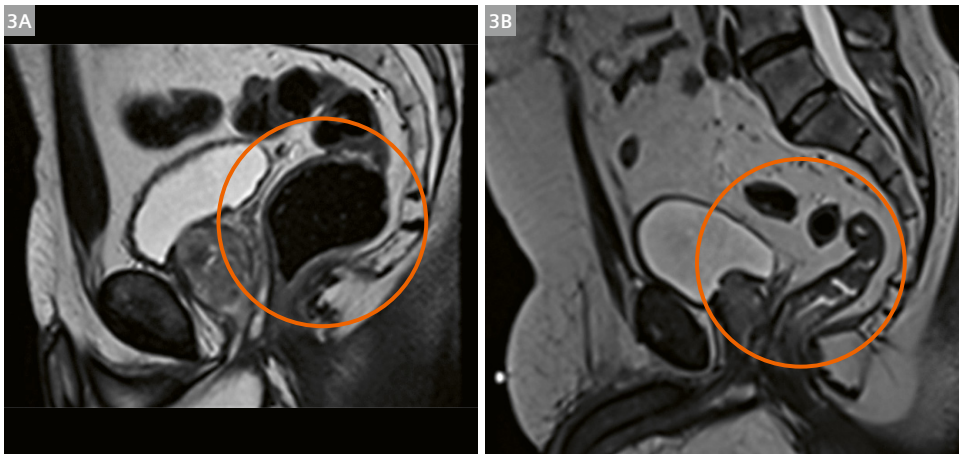

3 Comparison of rectal distension in diagnostic MRI (3A) and RTP MRI (3B): **(3A)** sagittal T2W diagnostic image with rectal distension; **(3B)** sagittal T2W RTP image with no rectal distension.

Research study: Optimization of bp-MRI of the prostate using a self-administered enema

Background

During our collaborative MR radiotherapy-planning (RTP) sessions, a significant reduction in air-filled rectal distension was observed in sagittal RTP images (see Fig. 3). This led to local discussions about the standard procedure for the imaging and treatment of all prostate patients undergoing radiotherapy at NWCC. Minimal bowel preparation in the form of a self-administered micro-enema is used just prior to all RT imaging and treatment to evacuate the rectum prior to all scans. This facilitates accuracy in gross-tumor-volume (GTV) contouring for RT treatment planning, and during all subsequent treatments to ensure reproducibility of the anatomical position of the prostate gland and promote positional accuracy of the treatment beam. RT experiences, including evidence in the literature [13], have proven this to be a cost-effective and minimally invasive patient procedure that is easily tolerated by patients. MR radiographers were keen to explore any potential benefit to diagnostic MRI protocols, and a local study was set up.

Rectal distention on Sag T2		Distortion on DWI + ADC		Confidence in lesion conspicuity	
Clear	0	None	0	Poor	0
Minimal	1	Minimal	1	Fair	1
Partial	2	Moderate	2	Good	2
Fully	3	Severe	3	Excellent	3

Table 1: Radiological scoring criteria

Aims and objectives

The aim of this research was to ascertain whether using a micro-enema before prostate imaging influences image interpretation. The main objectives were to collect data on prostate image interpretation with and without use of a micro-enema, to compare data, and to reach a conclusion on the efficacy of micro-enema use with respect to image quality in bp-MRI for pre-biopsy imaging.

Methodology

Thirty consecutive pre-biopsy referrals for prostate MRI were asked to attend their MRI appointment 45 minutes early to self-administer a micro-enema approximately 30 minutes prior to MRI scanning. Thirty consecutive patients scanned prior to the trial period, without preparation, acted as the control. To ensure comparable findings, exclusion criteria were applied to both groups and included patients with THR in situ and patients who presented with any contraindications to IV antispasmodic drugs. A standard NWCC high-resolution, PI-RADS v2-compliant protocol was carried out on all patients. Two consultant radiologists experienced in reporting prostate bp-MRI individually scored all images according to the criteria shown in Table 1. Cases were randomized on reporting workstations, with both radiologists blinded to use of micro-enema and their colleague's scoring.

Results

- Scores for rectal distension are highly correlated between the two radiologists for prepared and unprepared patients ($r = 0.82$ and $r = 0.86$, respectively). This indicates improved visibility of the prostate bed when a micro-enema is administered compared to unprepared patients ($p = 0.16$ and $p = 0.04$).
- Scores for distortion on DWI demonstrated moderately correlated scores ($r = 0.76$ and $r = 0.67$), with statistically high significance for prepared patients compared to unprepared patients ($p = 0.0$ and $p = 0.28$).

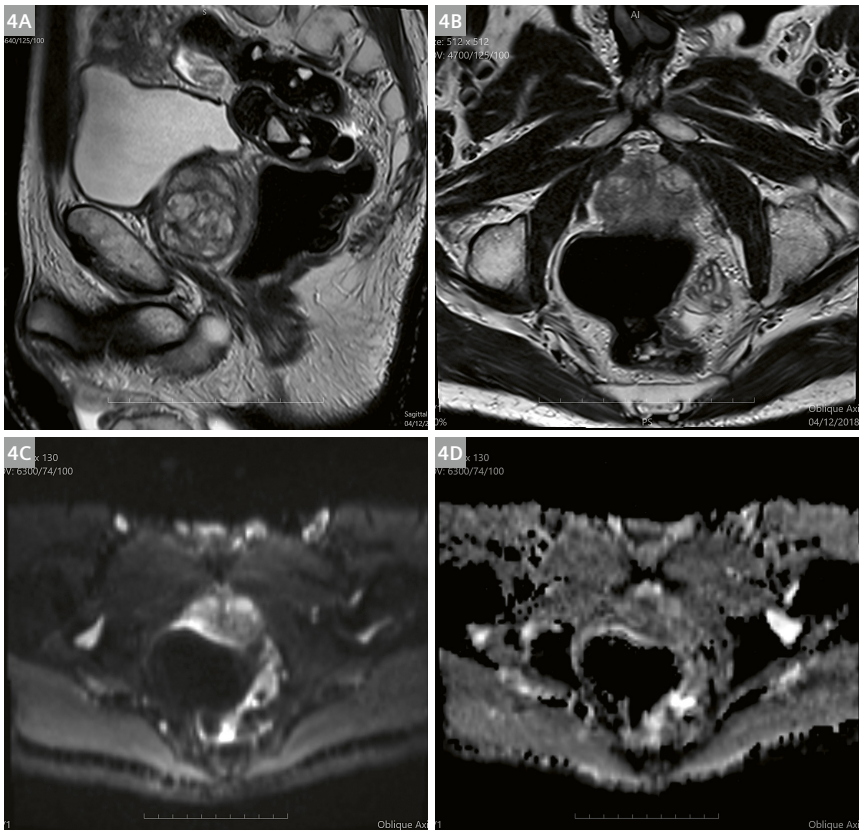

4 Sample images from control group (no bowel preparation):
(4A) Sag T2w TSE; **(4B)** Tra T2w TSE;
(4C) Tra DWI b-value = 800 s/mm²;
(4D) ADC map.

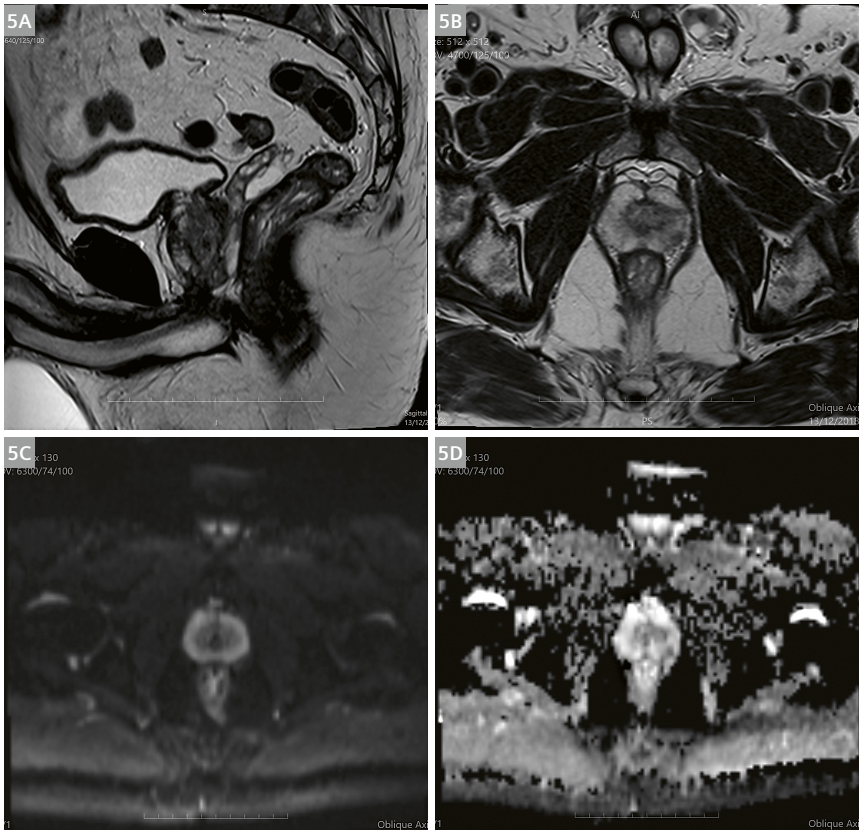

5 Sample images from study group (bowel preparation administered):
(5A) Sag T2w TSE; **(5B)** Tra T2w TSE;
(5C) Tra DWI b-value = 1400 s/mm²;
(5D) ADC map.

- Scores for distortion on apparent diffusion coefficient (ADC) maps also demonstrated agreement on moderately correlated scores (r = 0.54 and r = 0.59), and also high significance (p = 0.0), which proves that visibility for identifying distortion is better in the case of prepared patients.
- There is a high correlation in lesion visibility on DWI (r = 0.50) and an overall improvement in confidence (p = 0.36) for prepared patients.
- Radiologist 2 has a higher variance in scoring than Radiologist 1, irrespective of whether patients were prepared or not. However, variance in scoring is reduced in prepared patients, which indicates a higher level of confidence in lesion visibility among the radiologists (see Fig. 6).

Conclusion

Micro-enema administration demonstrates a significant benefit to image quality in bp-MRI of the prostate and should be considered as an integral part of the imaging procedure.

Study outcomes

Improvements in image quality and the clinical effectiveness of the radiological report, for both clinically significant and insignificant disease, were demonstrated in prepared patients. This led to a change in standard practice for bp-MRI prostate imaging at NWCC. Improved radiological confidence has reduced the imaging protocol, with the emphasis now on fully optimized bp-MRI rather than mp-MRI, leading to shorter scan times for patients and the potential for increased patient capacity. Improved confidence in the radiology findings at multidisciplinary meetings (MDMs) is proving especially beneficial for patients with insignificant or benign disease confirmed on MRI, and the potential to ensure progression to targeted biopsy is limited to equivocal cases only, e.g., PI-RADS 3. This places fewer clinical demands on the urology service overall. Utilizing a low cost, established technique that is easily tolerated by patients and involves minimal operational issues for staff has greatly improved the quality of our prostate imaging service.

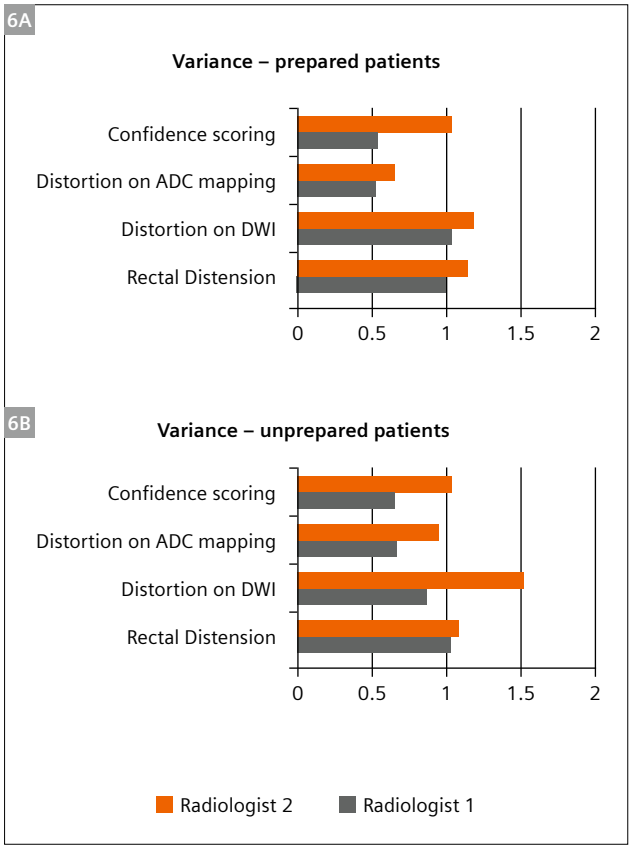

6 Comparison of variance in radiologist scoring in prepared (micro-enema) and unprepared patients.

Patient Information on Use of Micro-enema prior to MRI
You will be asked to use a form of bowel preparation called a micro-enema on arrival for your MRI. It falls within a group of medicines called laxatives, and is administered as a single dose to patients as a self-administered enema. It is being used before your MRI scan to empty your rectum of stools and air to get better images of the prostate gland, and help the doctors plan any treatment you may need more carefully. It may not be advisable to use if you suffer from any inflammatory bowel conditions, such as Crohn's disease, IBS, or colitis, so please make the staff aware of this. A micro-enema allows the insertion of a liquid into your back passage to help your lower bowel empty. Instructions will be given to you by the MRI staff on arrival, and it is usually effective within 15 mins. Toilets are nearby for use.
How to Use a Micro-enema
• Sit on the toilet • Pull or twist the cap off the plastic tube • Squeeze a drop of the liquid onto the nozzle to help lubricate it. • Put the full length of the nozzle into your back passage, and gently squeeze the tube until it is empty. • Wait for 15 mins for the laxative to work.
As it's a single dose, there is no risk of using too much and there should be no risk of prolonged diarrhoea. Staff will be happy to answer any questions you may have.

Table 2: Patient information on use of micro-enema prior to MRI.

How we do it: NWCC's current standard procedure and MR imaging protocol

Referral

Patients are all pre-biopsy urology referrals based on raised prostate-specific antigen levels (PSA) > 5.

Patient preparation

Patients are asked to arrive 45 minutes before their appointment time, so the only scheduling complication is around the first slot of the day. Information leaflets are sent out with appointment letters to advise patients of the need for bowel preparation on arrival (see Table 2). On patient arrival, MR radiographers go through the patient safety checklist to ensure there are no contraindications to MRI scanning that may negate the need for the enema. A drug checklist is also completed to ensure there are no inflammatory bowel conditions that could be aggravated by the enema, and no contraindications to the antispasmodic drug HBB 20 mg/mL (Buscopan), which is administered intravenously by radiographers guided by a local patient group directive (PGD). Radiologists are asked to prescribe the enema and, if PGD conditions are not met, the intravenous Buscopan.

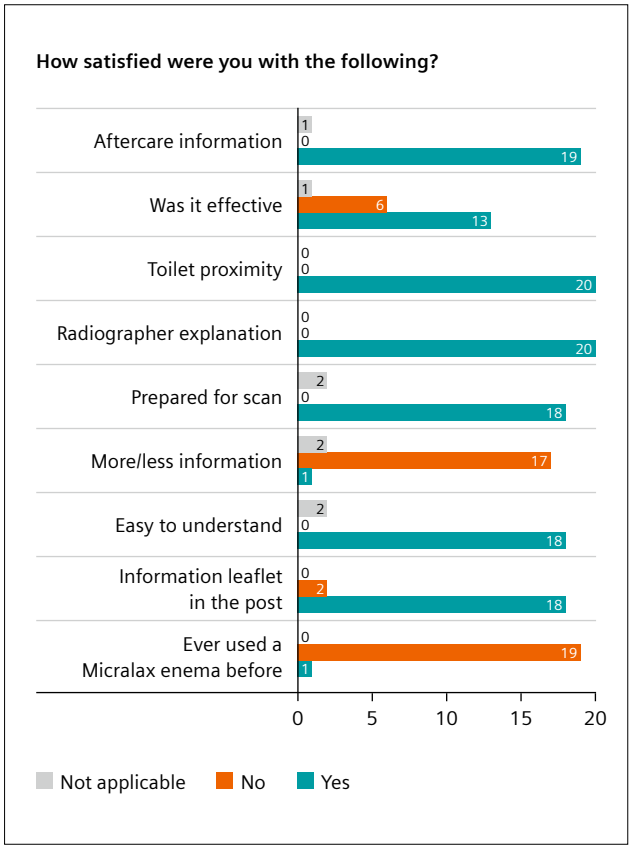

7 Outcomes of patient feedback audit.

An explanation of the procedure and its benefits for the imaging is provided to the patient in a private subwait area. If verbal consent is given, the patient is asked to proceed. Toilets are adjacent. A subsequent patient feedback audit demonstrated that most patients were well informed and tolerated the procedure well (see Fig. 7).

After 15–30 minutes, patients are brought in to have their IV cannulation for the Buscopan, which is administered once the patient is positioned on the scanner, due to its short-lived effect of only 15–20 minutes.

Additional patient preparation could be perceived as preventing radiographers from performing actual MR scans. However, as the bowel preparation is explained along with our MRI safety checklisting on arrival, and as radiographers insert all our cannulas anyway, it is seen as an integral part of the overall patient preparation procedure.

Equipment

Images were performed on a 24-channel 1.5T MAGNETOM Aera using an 18-channel Body Coil.

Patient positioning

Patients are always positioned supine, preferably head first unless claustrophobic, to ensure that whole-body SAR deposition is more accurately calculated.

The 18-channel Body Coil is positioned longitudinally on the patient's abdomen. This is acceptable as most of the anatomy to be imaged is midline, and it allows additional upper abdominal coverage for para-aortic nodes whilst providing improved patient comfort. Two transversely positioned body array coils would take longer to position, add extra weight on the patient's abdomen, and restrict the space available for their arms within the bore. Additional straps and coil size would also restrict access to the IV cannula for administration of Buscopan immediately prior to isocenter positioning.

Acquisition

The Dot Cockpit is fundamental to conducting these examinations efficiently and with an easily reproducible protocol of sequences that achieve consistency when multiple operators rotate through the department. Decision strategies built into the workflow are utilized to allow radiographers to adapt the protocol to patient-related scanning needs – e.g., when antispasmodic drug administration is contraindicated, or choosing the RESOLVE DWI option when THR is in situ. Orthogonal slice orientations are preferred by radiology, as they are easily reproduced to ensure consistency in imaging and to enable optimal calculation of gland volume. Imaging parameters are detailed in Table 3, and examples of images are shown in Figure 8.

Sequence	TR	TE	FOV	Slices			Matrix	Voxel size	iPAT	b-values s/mm²	Averages	Scan time min.sec
				Number	mm	Gap						
Sag T2W TSE	5200	122	200 x 100	30	3	0	320 x 80%	0.6 x 0.6 x 3.0	2		3	4.48
Cor T2W TSE	5200	122	200 x 100	30	3	0	320 x 80%	0.6 x 0.6 x 3.0	2		3	4.48
Tra T2W TSE	5200	122	200 x 100	34	3	0	320 x 80%	0.6 x 0.6 x 3.0	2		3	4.48
TRA DWI (1) + ADC	5800	66	300 x 100	34	3	0	120 x 80%	2.5 x 2.5 x 3.0	2	50 400 800	1 4 6	4.46
TRA DWI (2)	7100	72	300 x 100	34	3	0	120 x 80%	2.5 x 2.5 x 3.0	2	1400	12	6.18

Table 3: Standard bp-MRI sequences and parameters; total acquisition time < 30 minutes.

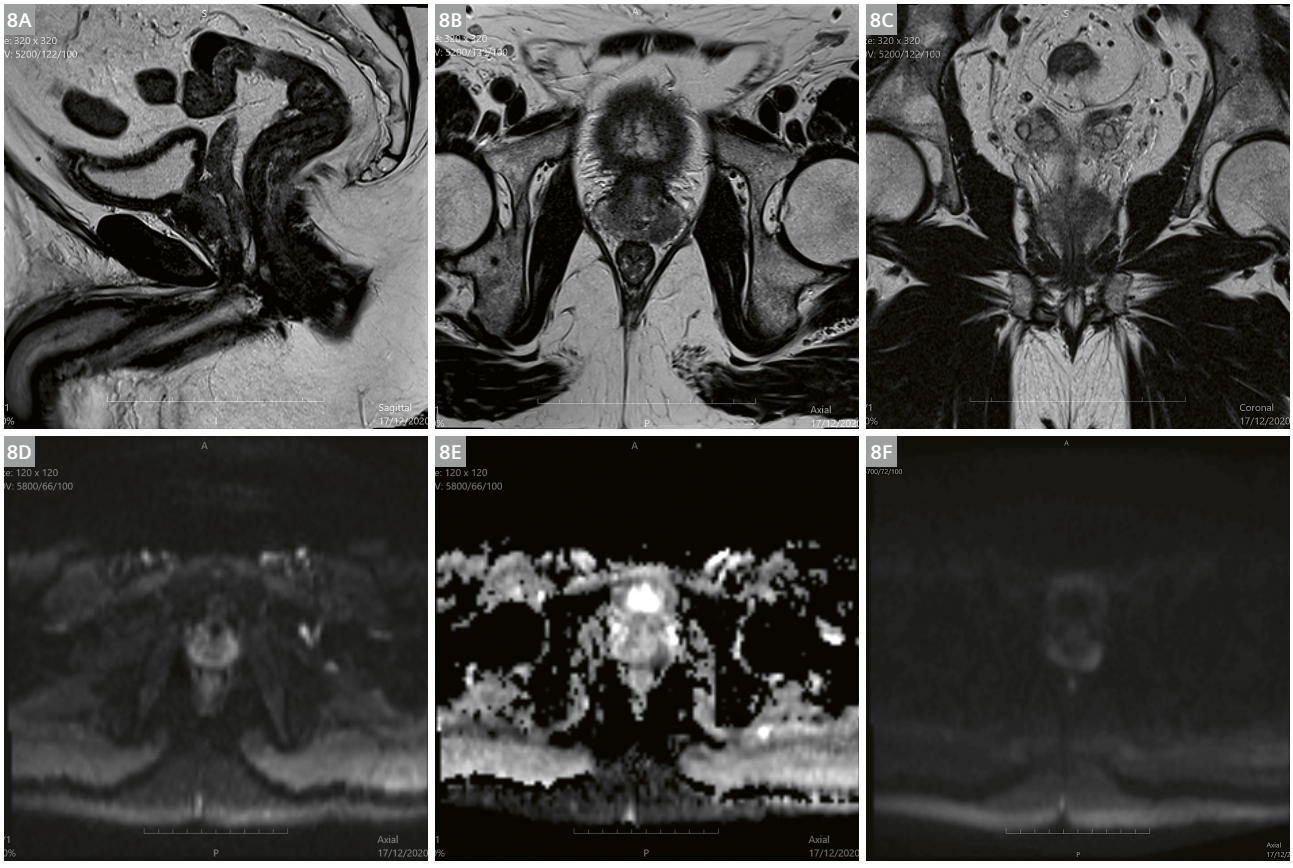

8 Examples of standard optimized protocol: **(8A)** Sag T2W, no rectal distension; **(8B)** Tra T2W; **(8C)** Cor T2W; **(8D)** Tra DWI b-value = 800 s/mm²; **(8E)** Tra DWI ADC map; **(8F)** Tra DWI b-value = 1400 s/mm².

Conclusion

Fully optimizing bp-MRI in the assessment of prostate cancer using a combined technical and patient-focused approach has greatly increased our performance in several ways:

- A low-cost operational change with minimal impact on staff and patients has delivered a significant improvement in image quality, with reduced scan times.
- Dot delivers an efficient workflow to ensure a robust, easily reproduced protocol, which is acquired within 30 minutes and maximizes capacity.
- It has optimized patient flows within the department, minimizing the time patients spend on the scanner.
- Increased time spent with clinical staff prior to MRI has boosted patient confidence in the overall process and experience, and although no evidence is currently available, we do have a very low rate of claustrophobia and anxiety-related refusals.
- Much-improved and consistent image quality with minimal artifacts has increased confidence in diagnostic accuracy for radiologists, and in the decision strategies adopted for patient management at urology MDMs.

Acknowledgments

Huge thanks to all our dedicated NWCC colleagues, past and present, from radiology, radiotherapy, and urology. We are grateful for all their support and for their involvement in the research study and the development of this imaging procedure. Particular thanks go to the diagnostic MR radiographers at NWCC for their enthusiasm about changing practice.

References

1 Prostate cancer: Diagnosis and Management, NICE guideline 131 [document on the Internet]. The National Institute for Health and Care Excellence; 2019 [cited October 21 2020]. Available from: https://www.nice.org.uk/guidance/ng131

2 Kizilay F, Çelik S, Sözen S, Özveren B, Eskiçorapçı S, Özgen M, et al. Correlation of Prostate-Imaging Reporting and Data Scoring System scoring on multiparametric prostate magnetic resonance imaging with histopathological factors in radical prostatectomy material in Turkish prostate cancer patients: a multicenter study of the Urooncology Association. Prostate Int. 2020;8(1):10–15.

3 Maddams J, Utley M, Møller H. Projections of cancer prevalence in the United Kingdom 2010–2040. Br J Cancer. 2012;107(7):1195–202.

4 Barentsz JO, Richenberg J, Clements R, Choyke P, Verma S, Villeirs G, et al. ESUR prostate MR guidelines 2012. Eur Radiol. 2012;22(4):746–57.

5 PI-RADS Prostate Imaging – Reporting and Data System: 2015 Version 2. [document on the Internet]. Reston, VA: American College of Radiology. 2015 [cited October 21 2020]. Available from: https://www.acr.org/-/media/ACR/Files/RADS/Pi-RADS/PIRADS-V2.pdf

6 Caglic I, Barrett T. Optimising prostate mpMRI: prepare for success. Clin Radiol. 2019;74(11):831–840.

7 Purysko AS, Rosenkrantz AB. Technique of Multiparametric MR Imaging of the Prostate. Radiol Clin North Am. 2018;56(2):211–222.

8 PI-RADS Prostate Imaging – Reporting and Data System: 2019 Version 2.1. [document on the Internet]. Reston, VA: American College of Radiology. 2019 [cited October 21 2020]. Available from: https://www.acr.org/-/media/ACR/Files/RADS/Pi-RADS/PIRADS-V2-1.pdf

9 Grant KB, Harsh KA, Shih JH, Bernardo M, Pang Y, Daar D, et al Comparison of calculated and acquired high b value diffusion-weighted imaging in prostate cancer. Abdom Imaging. 2015;40(3):578–586.

10 Slough RA, Caglic I, Hansen NL, Hansen NL, Barrett T. Effect of hyoscine butylbromide on prostate multiparametric MRI anatomical and functional image quality. Clin Radiol. 2018;73(2):216e9-216e14.

11 van Griethuysen JJM, Bus EM, Hauptmann M, Lahaye MJ, Maas M, Ter Beek LC, et al. Gas-induced susceptibility artifacts on diffusion-weighted MRI of the rectum at 1.5 T – Effect of applying a micro-enema to improve image quality. Eur J Radiol. 2018;99:131–137.

12 Caglic I, Hansen NL, Slough RA, Patterson AJ, Barrett T. Evaluating the effect of rectal distension on prostate multiparametric MRI Image quality. Eur J Radiol. 2017;90:174–180.

13 Padhani AR, Khoo VS, Suckling J, Husband JE, Leach MO, Dearnaley DP. Evaluating the effect of rectal distension and rectal movement on prostate gland position using cine MRI. Int J Radiat Oncol Biol Phys. 1999;44(3):525–33.

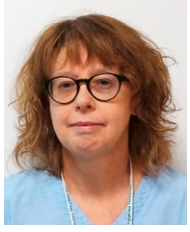

Contact

Lynn Doy, DCR(R) MSc
Department of Radiology
North West Cancer Centre
Altnagelvin Area Hospital
Glenshane Road, Londonderry, BT46 6SB
Northern Ireland
Lynn.Doy@westerntrust.hscni.net

High-Resolution Accelerated Prostate TSE Axial Imaging with Deep Learning Reconstruction at 3 Tesla

Edouard Reizine, M.D.[1]; Wafa Boughanmi, M.D.[1]; Aurélien Massire, Ph.D.[2]; Elisa Roccia, Ph.D.[3]; Dominik Nickel, Ph.D.[3]; Thomas Benkert, Ph.D.[3]; Alain Luciani, Ph.D., M.D.[1,4,5]

[1]Service d'Imagerie Médicale, AP-HP, Hôpitaux Universitaires Henri Mondor, Créteil, France
[2]Siemens Healthcare SAS, Saint-Denis, France
[3]Siemens Healthineers, Erlangen, Germany
[4]Faculté de Santé, Université Paris-Est Créteil, Créteil, France
[5]INSERM IMRB, U 955, Equipe 18, Créteil, France

Introduction

Multiparametric MRI is a crucial tool for prostate cancer detection, staging, active surveillance, and now also prior to biopsies (MRI-targeted biopsies). The guidelines for prostate imaging (PI-RADS [1]) currently recommend a protocol that consists of several MR sequences: T2-weighted (T2w), diffusion-weighted imaging (DWI), and dynamic contrast-enhanced (DCE) imaging. Notably, the T2w turbo spin echo (TSE) sequence should be acquired in the axial plane, with a slice thickness of 3 mm without gaps, and high in-plane spatial resolution. The increased demand for prostate MRI examinations observed in the past years requires to adequately respond by reducing the examination times in order to increase throughput on the one hand and to minimize the table time for the patient on the other. Indeed, this is especially problematic as prostate cancer commonly affects elderly men, who may have difficulties remaining motionless during long MRI examinations.

Deep learning reconstruction has played a key role in tackling this challenge, as it has been proven to reduce acquisition times with comparable, and often improved, image quality and diagnostic accuracy compared to standard reconstruction techniques [2–4]. Initially Siemens Healthineers' deep learning reconstruction solution, Deep Resolve, consisted of Deep Resolve Gain and Deep Resolve Sharp.

- Deep Resolve Gain [5] mitigates thermal noise by incorporating prior knowledge of the noise characteristics into the image reconstruction, performing denoising of the data in image space. The enhanced SNR can be used to accelerate the acquisition by either increasing the acceleration factor in parallel imaging or by reducing the number of averages.
- Deep Resolve Sharp improves the image sharpness by reconstructing a high-resolution image from low-resolution data using a deep neural network. In particular it suppresses truncation artifacts in *k*-space and allows to avoid conventional *k*-space filtering. This enables to achieve image resolutions that would not be possible to achieve using conventional reconstruction.

When we first tested Deep Resolve Gain and Sharp at the Henri Mondor hospital, we were convinced by the results and decided to immediately implement it in our clinical practice. Deep Resolve is indeed now the standard of operation for prostate MR imaging at our institution.

This deep learning reconstruction technology has now gone one step further with the introduction of Deep Resolve Boost, which is even more powerful, bringing the results to a new level.

Deep Resolve Boost for TSE

Deep Resolve Boost replaces the conventional image reconstruction with a deep neural network [2]. The network architecture has similarities to an iterative image reconstruction and receives undersampled raw data as well as pre-estimated coil sensitivity maps as input. High quality images are then obtained by alternating between a parallel imaging model that relates images to acquired data and a deep learning-based regularization that enhances image quality. The main benefit of this technology is the ability to reduce the acquisition time without compromising SNR or image quality, as described in several publications [3, 6]. The outcome of the reconstruction can be further improved by combining Deep Resolve Boost with Deep Resolve Sharp.

Materials and methods

At our institution we had access to a research implementation of Deep Resolve Boost for TSE[1]. All patients underwent a prostate examination in our clinical 3T MR system (MAGNETOM Vida; Siemens Healthcare, Erlangen, Germany) with XT gradients, an 18-channel body array and a 72-channel spine array. We acquired three MR sequences:

- Transverse 2D T2w TSE reconstructed with Deep Resolve Gain and Sharp
- Transverse 2D T2w TSE reconstructed with the research implementation of Deep Resolve Boost[1]
- Transverse 2D diffusion single-shot EPI with 3 b-values (50, 1000, 1500 s/mm^2)

The acquisition parameters of the T2-weighted sequences are shown in Table 1.

We present a series of clinical cases which show that Deep Resolve Boost for TSE provides at least similar image quality and diagnostic information as the more time-intensive Deep Resolve Gain and Sharp TSE acquisition, which is now the clinical standard at our institution.

[1] *With software version syngo MR XA50 Deep Resolve Boost is available for MAGNETOM Vida.*

	Deep Resolve Gain and Sharp TSE	Deep Resolve Boost TSE
Scan time (min:s)	**3:16**	**1:50**
FOV (mm^2) / phase oversampling	160 × 160 / 145%	180 × 180 / 200%
TE (ms)	116	104
TR (ms)	3380	3850
Reconstructed voxel size (mm^3)	0.26 × 0.26 × 3	0.24 × 0.24 × 3
Nb excitations	**2**	**1**
Matrix size	304 × 304 × 26	368 × 368 × 26
Acceleration technique	GRAPPA 2 (Auto -32)	GRAPPA 3 (TSE/Sep -24)
Flip angle (°)	133	160
Turbo factor	23	25
Phase resolution (%)	85	85
Bandwidth (Hz/Px)	201	200
Nb concatenations	2	2

Table 1: Acquisition parameters of the T2-weighted sequences.

Cases

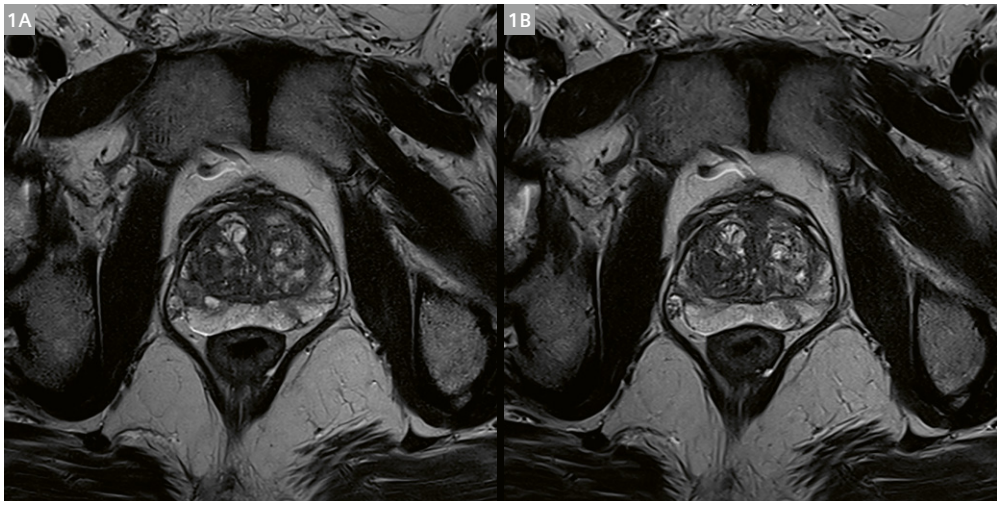

1 A 72-year-old patient (Density PSA = 0.09 ng/ml²) with bilateral PI-RADS 2 lesions in the middle peripheral zones of the prostate. T2-weighted TSE using **(1A)** Deep Resolve Gain and Sharp and **(1B)** Deep Resolve Boost. Deep Resolve Boost provides comparable image quality with a 41% scan time reduction.

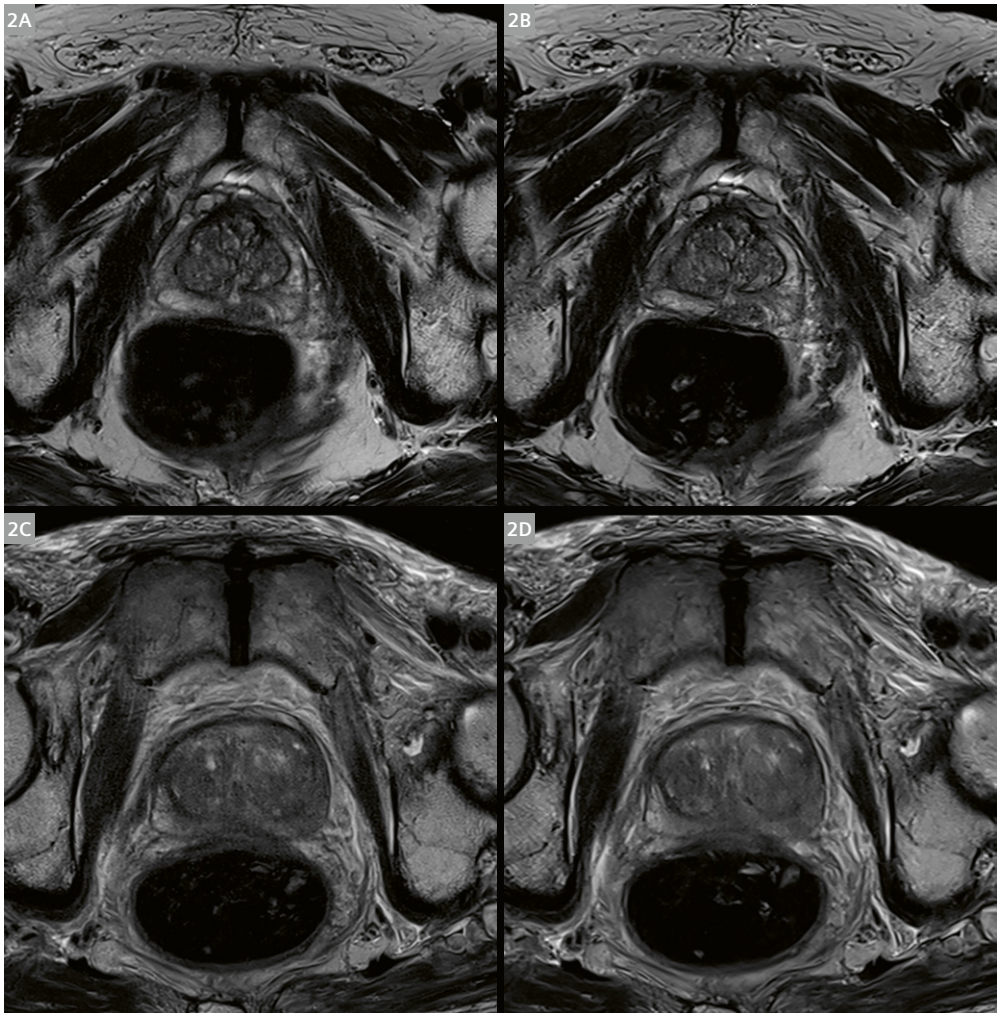

2 A 77-year-old patient (PSA = 1.7 ng/ml; density PSA = 0.05 ng/ml²) with bilateral PI-RADS 2 lesions in the middle peripheral zones of the prostate. T2-weighted TSE using **(2A)** Deep Resolve Gain and Sharp and **(2B)** Deep Resolve Boost.

An 83-year-old patient (PSA =14.8 ng/ml; density PSA = 0.29 ng/ml²) with a PI-RADS 4 lesion in the right postero-medial middle peripheral zone of the prostate. T2-weighted TSE using **(2C)** Deep Resolve Gain and Sharp and **(2D)** Deep Resolve Boost.

For both patients, motion artefacts in the Deep Resolve Boost images are reduced thanks to the shorter acquisition time (1 average), allowing sharper delineation of the anatomical structures.

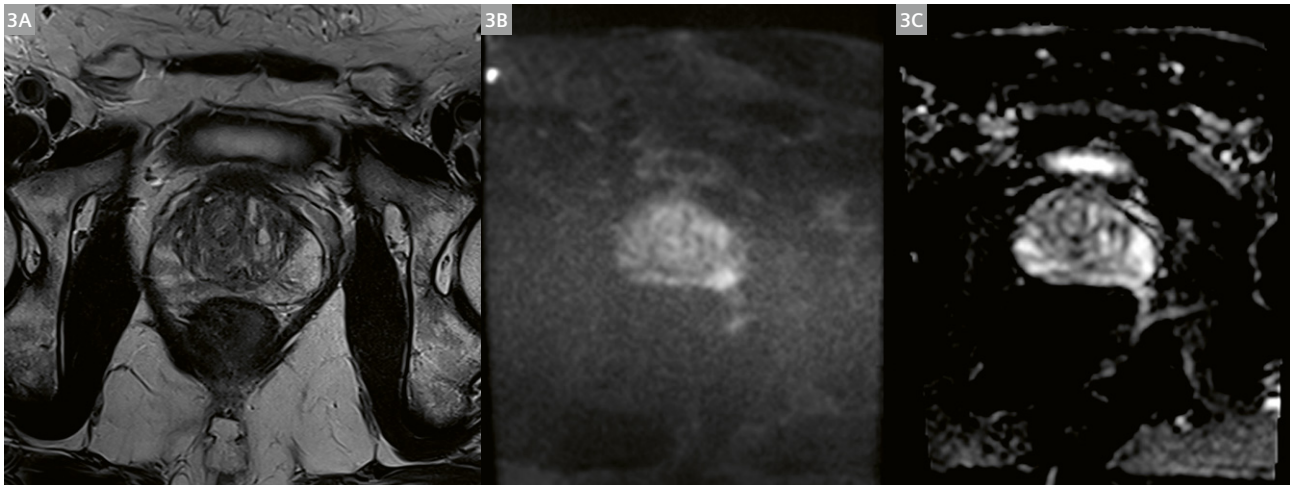

3 A 59-year-old patient (PSA: 4.2 ng/mL; density PSA = 0.10 ng/ml^2) with bilateral PI-RADS 2 lesions in the middle peripheral zones of the prostate. T2-weighted TSE using **(3A)** Deep Resolve Boost. **(3B)** Trace DWI image with b-value 1500 s/mm^2, **(3C)** ADC map.

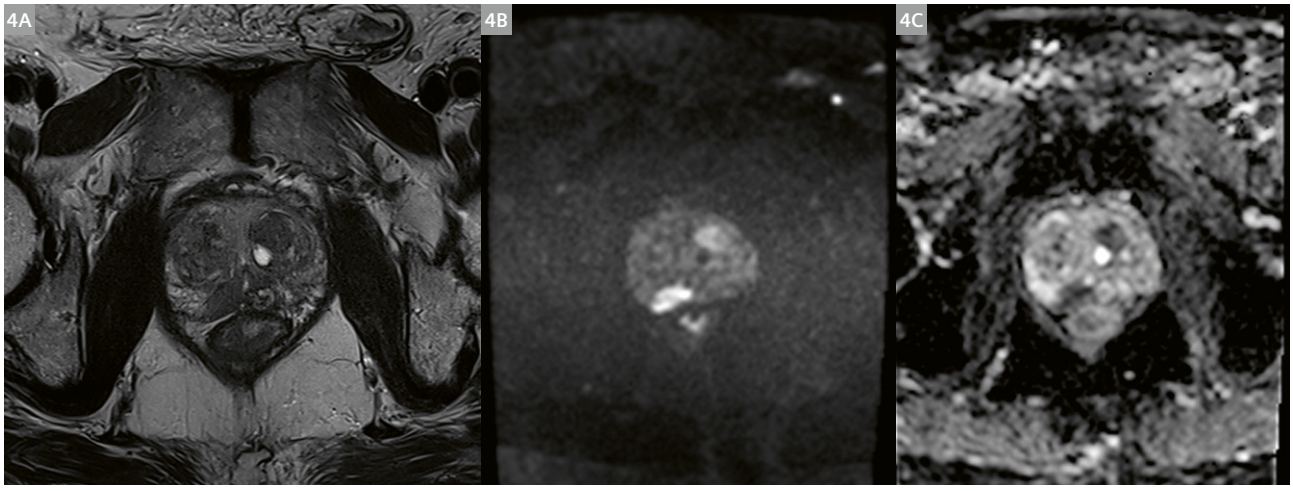

4 A 81-year-old patient (PSA: 12 ng/mL; density PSA = 0.33 ng/ml^2) with a PI-RADS 5 lesion in the right posteromedial apical peripheral zone of the prostate. T2-weighted TSE using **(4A)** Deep Resolve Boost. **(4B)** Trace DWI image with b-value 1500 s/mm^2, **(4C)** ADC map.

Conclusion

Compared to Deep Resolve Gain and Sharp, Deep Resolve Boost allowed us to decrease the acquisition time of the T2w TSE acquisition by 41% (Fig. 1), as only 1 average was acquired compared to the 2 averages of the Deep Resolve Gain and Sharp scan, with comparable image quality. One of the benefits of the shorter acquisition time was the reduction of artefacts due to either voluntary or involuntary patient motion (Fig. 2), which is one of the challenges of prostate imaging. No evident artefacts were observed. There is an increasing body of evidence from clinical studies and scientific publications that these physics-guided deep learning reconstruction approaches provide reliable and robust image information with anatomical fidelity.

These results are also in line with the published literature, which has reported significant time savings, as well as comparable image quality and diagnostic confidence for staging prostate lesions when compared to conventional acquisitions [2–4, 7].

The adoption of Deep Resolve in our clinical workflow has helped us to match the increased demand of prostate MRI examinations at our institution and we are confident that further improvements in acquisition time and spatial resolution can be achieved.

References

1 Weinreb JC, Barentsz JO, Choyke PL, Dornud F, Haider MA, Macura KJ, et al. PI-RADS Prostate Imaging – Reporting and Data System: 2015, Version 2. Eur. Urol. 2016, 69, 16–40.
2 Gassenmaier S, Afat S, Nickel D, Mostapha M, Herrmann J, Othman AE. Deep learning-accelerated T2-weighted imaging of the prostate: Reduction of acquisition time and improvement of image quality. Eur J Radiol. 2021;137:109600.
3 Gassenmaier S, Afat S, Nickel MD, Mostapha M, Herrmann J, Almansour H, Nikolaou K, Othman AE. Accelerated T2-Weighted TSE Imaging of the Prostate Using Deep Learning Image Reconstruction: A Prospective Comparison with Standard T2-Weighted TSE Imaging. Cancers (Basel). 2021;13(14):3593.
4 Kim EH, Choi MH, Lee YJ, Han D, Mostapha M, Nickel D. Deep learning-accelerated T2-weighted imaging of the prostate: Impact of further acceleration with lower spatial resolution on image quality. Eur J Radiol. 2021;145:110012.
5 Dehem J, Kannengießer S, Hoelscher UC. Initial Clinical Experience with an Iterative Denoising Algorithm Applied to Reduced-data 2D Turbo Spin Echo Acquisitions. ↗MAGNETOM Flash. 2021;(78)2:22-28.
6 Herrmann J, Gassenmaier S, Nickel D, Arberet S, Afat S, Lingg A, et al. Diagnostic Confidence and Feasibility of a Deep Learning Accelerated HASTE Sequence of the Abdomen in a Single Breath-Hold. Invest Radiol. 2021;56(5):313–319.
7 Johnson PM, Tong A, Donthireddy A, Melamud K, Petrocelli R, Smereka P, Qian K, Keerthivasan MB, Chandarana H, Knoll F. Deep Learning Reconstruction Enables Highly Accelerated Biparametric MR Imaging of the Prostate. J Magn Reson Imaging. 2022;56(1):184-195.

Contact

Professor Alain Luciani, Ph.D., M.D.
HU Henri Mondor
Medical Imaging Department
APHP, UPEC University
51 Avenue Mal De Lattre De Tassigny
94000 Créteil
France
alain.luciani@aphp.fr


Alain Luciani, Ph.D., M.D.


Edouard Reizine, M.D.

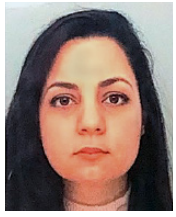
Wafa Boughanmi, M.D.

An automated, end-to-end prostate MRI pathway solution

Screening & Early Detection

myExam Prostate Assist
Assistance for consistent and reproducible scanning

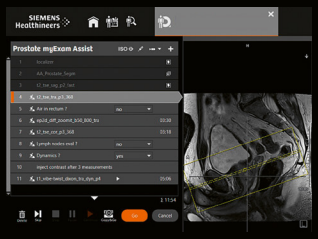

Deep Resolve and ZOOMit[PRO]
Robust bi-parametric PI-RADS 2.1 prostate exams in 5 minutes[1]

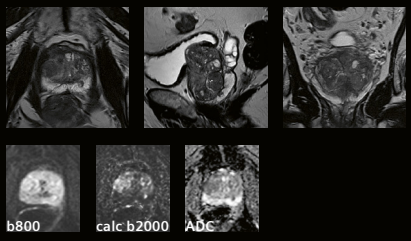

2aaaa2767

Diagnosis & Therapy Decision

Prostate MR[2]
AI detection and classification of prostate lesions

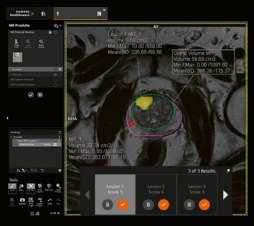

Prostate MR – for biopsy support
Export of segmentations for MR/US-fusion biopsy support

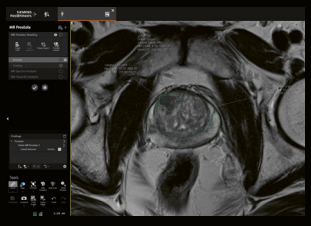

Treatment Planning & Delivery

MR-based Synthetic CT
MR-only workflow for RT planning

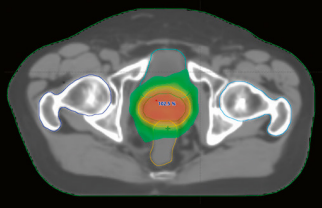

Profound TULSA-PRO[3]
Focal treatment under real-time MR-temperature control

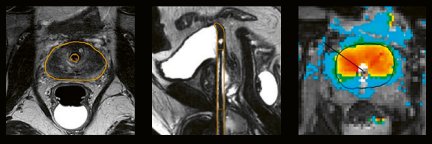

Follow-up & Survivorship

syngo.MR OncoTrend
Accurate therapy response monitoring

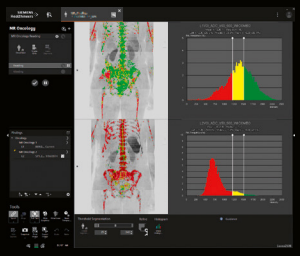

[1] Deep Resolve for DWI is still under development and not commercially available.
[2] The product is not commercially available in some countries, e.g. the US. Due to regulatory reasons their future availability cannot be guaranteed. Please contact your local Siemens Healthineers organization for further details.
[3] The information shown herein refers to products of 3rd party manufacturers and thus are in their regulatory responsibility. Please contact the 3rd party manufacturer for further information.

Order your own PI-RADS poster here

SIEMENS Healthineers

Environmental Sustainability in Magnetic Resonance

MRI is the major contributor in radiology to energy consumption

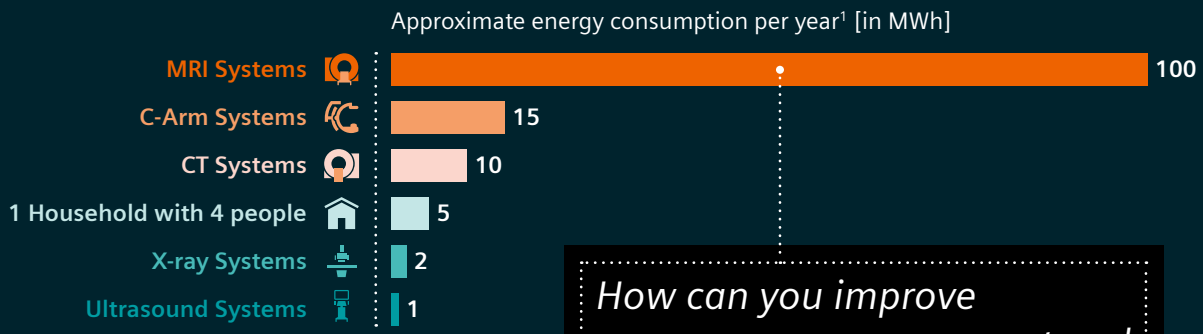

How can you improve your energy management and save electricity in MRI?

Did you know? We're also working on saving helium!

Zero Helium Boil-off Technology

It was first introduced in 2004 and prevents helium boil-off throughout your scanner's lifetime. It is available for all our MAGNETOM systems.

Up to 37% reduction in helium inventory

A significant reduction in helium inventory is possible with our latest scanner generation.

- Improved magnet & gradient architecture
- Strong reduction of conductive materials
- More efficient cooling

DryCool Technology

Our new class of MRI systems offers you the most compact whole-body MRI with virtually helium-free infrastructure and radically simplified infrastructure requirements:

- Only 0.7 liters liquid helium
- Sealed-for-life magnet design
- No quench pipe
- New benchmark in ramp-up times

Values are computed for a 1.5T MAGNETOM Sola system for illustration purposes.

1 Data Siemens Healthineers own measurements and assumptions; Actual consumption can vary depending on use pattern, system type, and configuration.

2 Assuming the system is turned on during the weekends and overnight.

3 Results are quantified assuming scanning operations as per COCIR standards.

How to save energy with your MRI system:

Energy consumption for an MRI system in one year, if the scanner is always on[2]: **100 MWh**

Save ~20% energy by turning off your scanner when not in use[3] **~80 MWh**

Did you know?

The start-up time for our scanners is only approx. 5.5 minutes and with our System Start-Up Timer you can enable automatic start-up of your scanner. So your system is ready when the workday starts!

Save ~12% energy by using Eco Power mode[3] **~70 MWh**

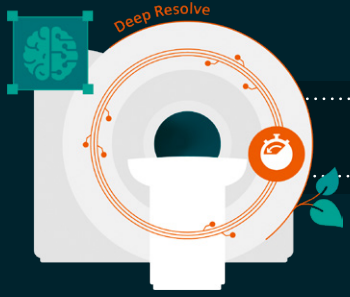

Save ~13% energy by using Deep Resolve **~60 MWh**

Make the most of our innovations and save **~40%** energy!

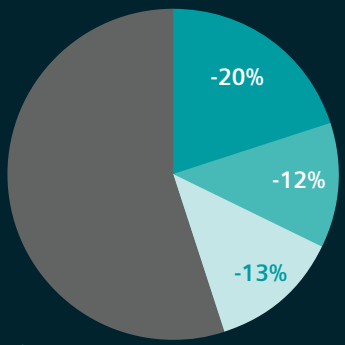

A Fully Automated, End-to-End Prostate MRI Workflow Solution Incorporating Dot, Ultrashort Biparametric Imaging and Deep-Learning-based Detection, Classification, and Reporting

David J. Winkel, M.D.[1]; Robert Grimm, Ph.D.[2]; Thomas Benkert, Ph.D.[2]; Berthold Kiefer, Ph.D.[2]; Daniel T. Boll, M.D.[1]

[1]Department of Radiology, University Hospital Basel, Switzerland
[2]MR Applications Predevelopment, Siemens Healthineers, Erlangen, Germany

Introduction

For more than a decade, magnetic resonance imaging (MRI) has been established as a powerful tool for prostate cancer diagnosis. The PROMIS study has demonstrated that prostate MRI is a suitable triage tool for biopsy-naïve men, reducing the number of unnecessary biopsies by a quarter while improving the detection of clinically significant cancer [1]. The PRECISION study randomized patients to either systematic biopsies or MRI; with no biopsy if MRI was negative, and targeted biopsy if MRI was positive. Targeted biopsies guided by MRI detected significantly more clinically significant cancers while reducing the number of clinically insignificant cancers [2]. Because of these findings, MRI for prostate cancer diagnosis has been integrated into established guidelines [3].

Increasing demand for prostate MRI examinations can be expected, as the incidence of prostate cancer increases with age and life-expectancy in developed countries is rising. Furthermore, prostate MRI has been discussed in the literature as a screening tool, similar to breast cancer screening [4]. However, several limitations need to be addressed in order to prepare for this increasing prostate MRI workload. Variation in MRI data acquisitions could be reduced [5]. Another limitation is the relatively long acquisition time of multiparametric MRI examinations (mpMRI) employing T2-weighted (T2w), diffusion-weighted imaging (DWI) and dynamic-contrast enhanced (DCE) MRI. Several studies have shown that an approach without DCE MRI, called biparametric MRI (bpMRI), yields comparable results to mpMRI of the prostate [6]. Potentially even more important topic is the varying interpretation performance based on the expertise level. However, even among expert radiologists, agreement on prostate cancer classification based on established guidelines is imperfect [7, 8].

This all points to a clear need for

1. Efficient, reproducible, and robust data acquisition workflow
2. Optimized and fast sequence design
3. Automated detection, classification, and reporting workflows in prostate MRI examinations

1 Image acquisition using the Prostate Dot Engine[1] including automated prostate contour detection, prostate centering, field of view adaption and three-dimensional correction of spatial axes.

This is a chain of independent, yet highly interlinked stages. Well-registered and reformatted images with reproducible high image quality are a key prerequisite for optimal and reproducible artificial intelligence-based analyses.

In this article, we outline an end-to-end solution that addresses all the limitations above, incorporating day optimizing throughput (Dot), ultrashort bpMRI and deep-learning-based lesion detection, classification and reporting. We present two example cases using the proposed workflow in order to illustrate its feasibility.

Material and methods

Prostate Dot Engine

The Prostate Dot Engine is a prototype software tool designed to provide a fast, robust, and standardized image acquisition workflow. After acquiring the Turbo-Spin Echo (TSE) scout, the Prostate Dot automatically centers the prostate in the field of view, adapts the size of the field of view and performs a three-dimensional correction of spatial axes. Slices can be aligned either strictly orthogonal or automatically defined by the orientation of the urethra, i.e., perpendicular to the urethra for the axial planes. Furthermore, the prostate is segmented for standardized volume assessment. After coil placement, the Dot workflow does not require further adaptations by technicians, and it allows interruptions and corrections of the scan process at any time. A screenshot of the Prostate Dot Engine can be found in Figure 1.

Sequence specifications

The biparametric protocol consists of a T2-weighted turbo spin-echo (TSE) pulse sequence in axial, sagittal and coronal orientations and an improved single shot DWI EPI sequence (ZOOMit^{PRO}, Siemens Healthcare, Erlangen, Germany) with consecutive computation of the apparent diffusion coefficient. Unlike other DWI techniques, ZOOMit^{PRO} magnifies the prostate (in the phase-encoding direction) and is free of infolding artifacts. Either a smaller quadratic FOV or only a reduced FOV in the phase-encoding direction ('stripe') is excited (see Figure 2A). As there is no signal from the non-excited regions, only the small stripe needs to be encoded (see Figures 2B, C). That means the encoding time can be decreased while maintaining spatial resolution, or the spatial resolution can be increased, or a combination of the two. Furthermore, decreased encoding time reduces spatial distortion.

Prostate AI

The output of the Prostate Dot Engine goes into the AI prototype (Prostate AI[1], Siemens Healthcare, Erlangen, Germany) for fully automatic prostate lesion detection, classification and reporting.

As illustrated in Figure 3, Prostate AI contains two parts:

1. A preprocessing pipeline
2. A component for lesion detection and classification, based on deep learning

The preprocessing pipeline takes the acquired bpMRI sequences and generates the required well-formatted and transformed data volumes. From the DWI series, a logarithmic extrapolation method is adopted to compute a new DWI volume with *b*-value of 2000 s/mm^2. This step

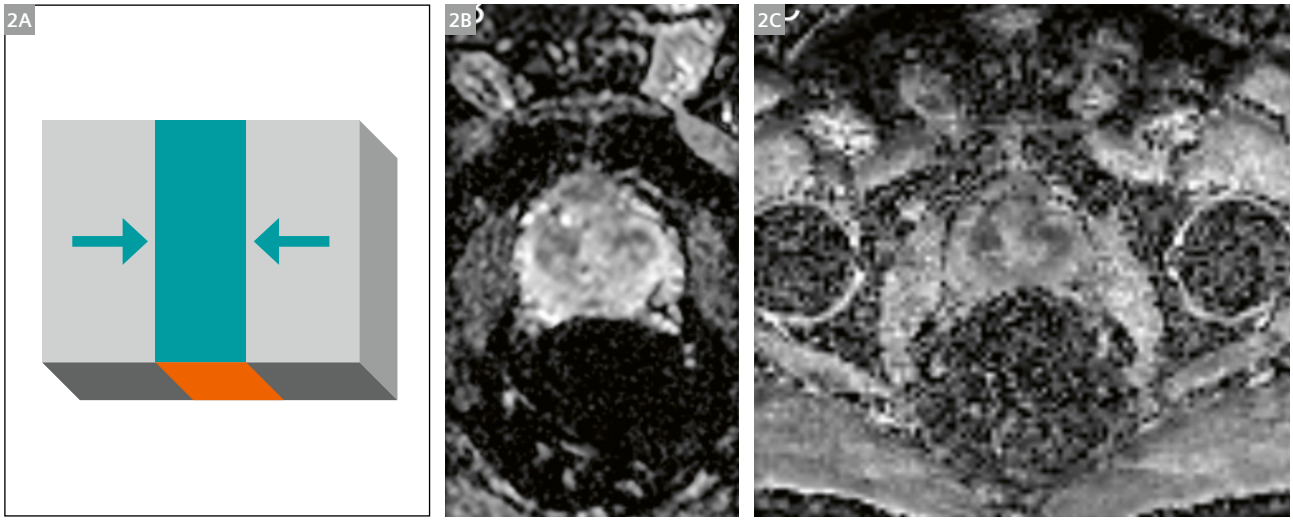

2 Single-shot DWI EPI sequence (ZOOMit^{PRO}) with image examples from one study object: **(2A)** reduced FOV in phase-encoding direction (blue stripe); **(2B)** resulting image in comparison to **(2C)** the conventional RESOLVE technique.

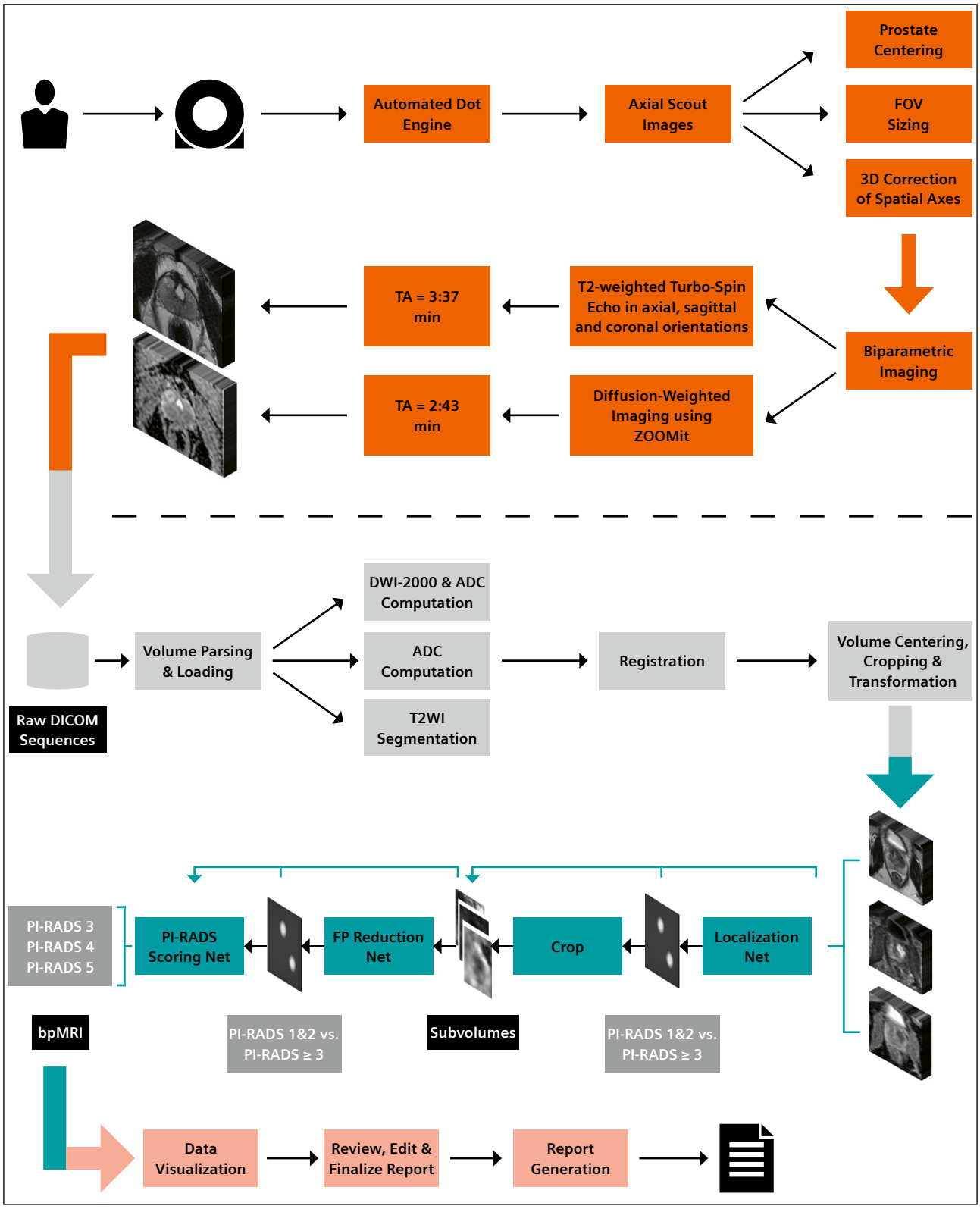

3 Image acquisition workflow using the automated Prostate Dot Engine and biparametric imaging (orange); deep learning architecture with preprocessing pipeline (gray); deep learning-based lesion detection and classification component (blue).

Dot = day optimizing throughput, FOV = field of view, 3D = three-dimensional, TA = time of acquisition, DICOM = Digital Imaging and Communications in Medicine, ADC = apparent diffusion coefficient, FP = false positive, PI-RADS = Prostate Imaging Reporting- and Data System

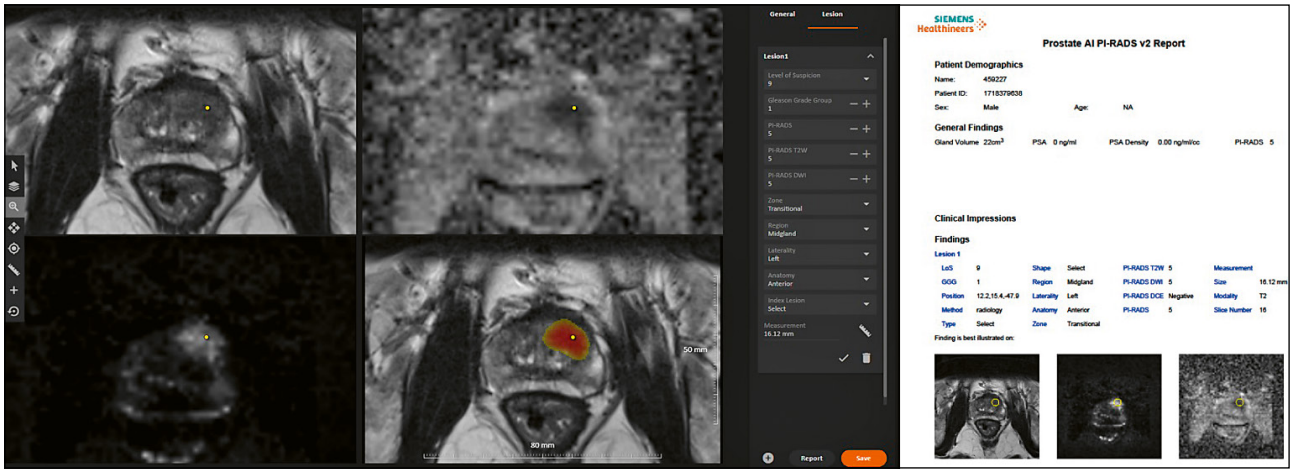

4 Data visualization platform with the T2w images, ADC map, and high *b*-value image as well as the T2w image overlaid with the AI-generated heatmap (in red and yellow). Prostate AI automatically detected the suspect lesion in the transition zone (TZ, yellow dot) and pre-populated all relevant information according to current PI-RADS guidelines. Next, a machine-readable report based on this information is generated.

can eliminate the *b*-value variances among the datasets and also improve lesion detection performance [10]. Also, apparent diffusion coefficient (ADC) maps are computed. Next, whole-organ gland segmentation is performed on the T2w volume using a learning-based method as presented in Yang et al. [11]. After segmentation, a rigid registration is conducted to align T2w and DWI images. The preprocessing pipeline can eliminate both geometric and intensity variances across sequences and patient studies.

Prostate AI then automatically detects clinically relevant lesions and classifies each detected lesion according to PI-RADS categories. This is achieved by a sequence of coupled deep neural networks that are trained separately. First, a fully convolutional localization net is able to generate a semantic lesion candidate heatmap (see Figures 5 and 6); then a sub-volume-based false positive reduction net further improves detection accuracy by removing the false positives; finally another sub-volume-based PI-RADS scoring net stages the level of malignancy for each detection according to PI-RADS categories.

In a last step, Prostate AI displays the detection and classification results on a dedicated platform. As the ability of the interpreting radiologist to accept or reject AI-based findings has been identified as a prerequisite for adoption of these techniques [12], these capabilities have been implemented. The user is then able to create a machine-readable report with all relevant information for the referring physician (see Figure 4). This report can be sent to the local RIS/PACS system.

Cases

Case 1

Figures 5A-D demonstrate a lesion in the right midgland PZpl/PZa of a 62-year-old man, with a maximum diameter of 30.2 mm and a mean ADC-value of 758 µm²/s. Prostate AI detected the lesion and assigned a PI-RADS 5 category. Biopsy results revealed a Gleason 4+3 = 7 pattern.

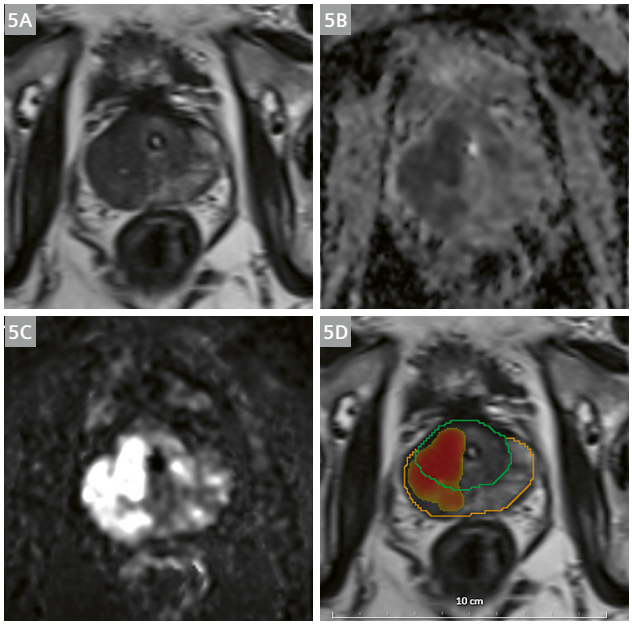

Case 2
Figures 6A-D demonstrate a lesion in the left apical PZpl of a 51-year-old man, with a maximum diameter of 10.2 mm and a mean ADC-value of 961 µm²/s. Prostate AI detected the lesion and assigned a PI-RADS 4 category. Biopsy results revealed a Gleason 3+3 = 6 pattern.

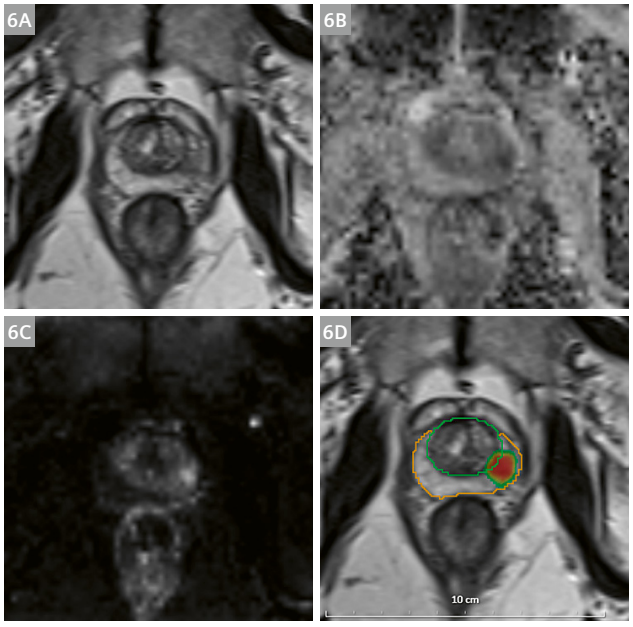

Conclusion

In this article, we outlined an end-to-end concept to allow a standardized workflow with a reproducible and fast data acquisition with optimized imaging sequences and an AI-empowered data analysis including automated detection, classification and reporting of suspicious lesions in biparametric prostate MRI examinations.

Reproducible and fast data acquisition concepts are not only contributing to a standardized reporting performed by human readers but would also help artificial intelligence-based solutions to reliably process input data. Preliminary results from a study conducted at the University of Innsbruck in Austria including 50 patients referred for a prostate MRI examination, compared the tilting angle of the auto-alignment of the Prostate Dot Engine against axes determined manually by an experienced radiologist, serving as the reference-standard. The investigators were able to show a mean ± SD deviation of the tilting angle of 5.5 ± 4.4 degrees (Ch. Kremser, W. Judmaier, Med. Uni Innsbruck, unpublished results). However, to date, there is no study investigating workflow differences, such as time-saving metrics, between Dot-guided and conventional, technician-guided workflows. Those studies are currently planned, and their results will contribute to reveal the value of Dot engines in clinical routine.

Concerning the use of abbreviated protocols consisting of T2-weighted and DWI only – so-called biparametric prostate MRI – several studies [6, 13, 14] have shown comparable results as obtained with conventional, mpMRI protocols including DCE-MRI. We added another component to our suggested workflow, that is performing DWI with the ZOOMit^{PRO}. As shown in Figure 2, ZOOMit^{PRO} uses a reduced FOV in the phase-encoding direction compared with either standard single shot DWI EPI or RESOLVE (REadout Segmentation Of Long Variable Echo trains). The resulting decreased acquisition time can be invested in a superior spatial resolution. Future studies are needed to systematically investigate differences between different types of DWI acquisition schemes compared to the ZOOMit^{PRO} technique.

The last component in our workflow is the use of AI-based lesion detection and classification. Schelb et al. [15] used the input from T2w sequences and DWI to train a deep learning algorithm (Unet) on the histopathological outcome, serving as ground truth. They were able to show that this algorithm achieved a similar performance to human readers using the PI-RADS assessment score. Cao et al. [16] used the input of mpMRI images to build a convolutional neural network trained on histopathological data and used this algorithm to detect suspicious lesions and to predict the Gleason score. The results were promising, with a high sensitivity for lesion detection – comparable to expert human readers – and a high classification performance with regards to clinically significant cancer. However, the usefulness of these algorithms needs to be proven in larger multi-reader, multi-case (MRMC) studies, systematically examining their influence on interpretation performance and speed, with and without those solutions.

We have identified a need to re-structure existing prostate MRI workflows, as patient or – in case of screening approaches – participant throughput is expected to increase. In our vision, current workflows need more reliable, reproducible and fast data acquisition steps. Furthermore, recent research has shown that deep learning algorithms can compete with human intelligence in prostate MRI reporting. We outlined a possible end-to-end solution and demonstrated its feasibility with two case examples. Future research will investigate what impact the individual components or the combination of those components will have on the future of prostate MRI.

References

1 Ahmed HU, El-Shater Bosaily A, Brown LC, et al. Diagnostic accuracy of multi-parametric MRI and TRUS biopsy in prostate cancer (PROMIS): a paired validating confirmatory study. Lancet. 2017;389:815–822. https://doi.org/10.1016/S0140-6736(16)32401-1
2 Kasivisvanathan V, Rannikko AS, Borghi M, et al. MRI-Targeted or Standard Biopsy for Prostate-Cancer Diagnosis. N Engl J Med. 2018;378:1767–1777. https://doi.org/10.1056/NEJMoa1801993
3 EAU Guidelines. Presented at the EAU Annual Congress Barcelona 2019. ISBN 978-94-92671-04-2.
4 Kim SJ, Vickers AJ, Hu JC. Challenges in Adopting Level 1 Evidence for Multiparametric Magnetic Resonance Imaging as a Biomarker for Prostate Cancer Screening. JAMA Oncol. 2018;4:1663–1664. https://doi.org/10.1001/jamaoncol.2018.4160
5 Padhani AR, Barentsz J, Villeirs G, et al. PI-RADS Steering Committee: The PI-RADS Multiparametric MRI and MRI-directed Biopsy Pathway. Radiology. 2019;292:464–474. https://doi.org/10.1148/radiol.2019182946
6 Weiss J, Martirosian P, Notohamiprodjo M, et al. Implementation of a 5-Minute Magnetic Resonance Imaging Screening Protocol for Prostate Cancer in Men with Elevated Prostate-Specific Antigen before Biopsy. Invest Radiol. 2018;53:186–190. https://doi.org/10.1097/RLI.0000000000000427
7 Weinreb JC, Barentsz JO, Choyke PL, et al. PI-RADS Prostate Imaging - Reporting and Data System: 2015, Version 2. Eur Urol. 2016;69:16–40. https://doi.org/10.1016/j.eururo.2015.08.052
8 Rosenkrantz AB, Ginocchio LA, Cornfeld D, et al. Interobserver Reproducibility of the PI-RADS Version 2 Lexicon: A Multicenter Study of Six Experienced Prostate Radiologists. Radiology. 2016;280:793–804. https://doi.org/10.1148/radiol.2016152542
9 Maas MC, Fütterer JJ, Scheenen TW. Quantitative evaluation of computed high b value diffusion-weighted magnetic resonance imaging of the prostate. Invest Radiol. 2013;48:779.
10 Rosenkrantz AB, Parikh N, Kierans AS, et al. Prostate Cancer Detection Using Computed Very High b-value Diffusion-weighted Imaging: How High Should We Go? Acad Radiol. 2016;23:704–711. https://doi.org/10.1016/J.ACRA.2016.02.003
11 Yang D, Xu D, Zhou SK, et al. Automatic Liver Segmentation Using an Adversarial Image-to-Image Network. In: Descoteaux M, Maier-Hein L, Franz A, et al (eds) Medical Image Computing and Computer Assisted Intervention – MICCAI 2017. Springer International Publishing, Cham. 2017; pp 507–515.
12 Padhani AR, Turkbey B. Detecting Prostate Cancer with Deep Learning for MRI: A Small Step Forward. Radiology. 2019;192012. https://doi.org/10.1148/radiol.2019192012
13 Kuhl CK, Bruhn R, Krämer N, et al. Abbreviated Biparametric Prostate MR Imaging in Men with Elevated Prostate-specific Antigen. Radiology. 2017;282:493–505. https://doi.org/10.1148/radiol.2017170129
14 Woo S, Suh CH, Kim SY, et al. Head-to-head comparison between biparametric and multiparametric MRI for the diagnosis of prostate cancer: A systematic review and meta-analysis. Am J Roentgenol. 2018;211:W226–W241. https://doi.org/10.2214/AJR.18.19880
15 Schelb P, Kohl S, Radtke JP, et al. Classification of Cancer at Prostate MRI: Deep Learning versus Clinical PI-RADS Assessment. Radiology. 2019;190938. https://doi.org/10.1148/radiol.2019190938
16 Cao R, Bajgiran AM, Mirak SA, et al. Joint Prostate Cancer Detection and Gleason Score Prediction in mp-MRI via FocalNet. IEEE Trans Med Imaging. 2019;38:2496–2506. https://doi.org/10.1109/TMI.2019.2901928

Contact

David J. Winkel, M.D.
Department of Radiology
University Hospital Basel
Spitalstrasse 21
4031 Basel
Switzerland
Tel.: +41 61 328 65 22
davidjean.winkel@usb.ch

Please note that the familiar Dot engines will move under the umbrella of the Siemens Healthineers myExam Companion. This will harmonize tools facilitating easier workflow across different modalities under one common brand name. On the MAGNETOM scanners myExam Companion will feature the "Dot engines" as "myExam Assist" or simply "Assist". The former "Prostate Dot Engine" becomes "myExam Prostate Assist".

Experiences with Robot Assisted MR-guided Inbore Prostate Biopsies

Jeroen Reijnen; Jon Bache Marthinsen

Radiology Department, Sørlandet Hospital Kristiansand, Kristiansand, Norway

Background

Clinical management of prostate cancer is strongly challenged by the triangle of very high prevalence [1], heterogeneous and poorly understood tumor biology, and significant side effects of established treatments [2]. In order to contain the harms of therapy, we have to put great effort into the difficult task of identifying, from a huge pool of indolent prostate cancers, the patients that actually benefit from treatment.

In recent years, multiparametric MR imaging of the prostate (mpMRI) has evolved into a useful tool in the pursuit of better prognostic stratification. On the one hand, quality assured mpMRI has great potential for triage of patients for biopsies [3], i.e. omitting unnecessary biopsies [4]. On the other hand, mpMRI targeted biopsies, instead of or in addition to systematic biopsies, escalate the detection rate of cancer that might need treatment [5] and increase the likelihood and confidence of attaining optimally representative biopsies, i.e. sampling tumor tissue that can be expected to drive prognosis.

Diagnostic pathway

In the assessment for possible prostate cancer at our prostate center, mpMRI is the first test for all patients. For interpretation of the mpMRI we apply PI-RADS v2, but in some cases deviate from the scoring guidelines. Based on recent literature [4] and internal results (Table 1), our group refrains from biopsy in most patients with a negative mpMRI (PI-RADS 1–2). Systematic biopsies despite negative mpMRI are performed in selected patients on the basis of certain clinical alarm signals, since it is clear that prostate cancers can have growth patterns that make them more or less MR-invisible. Patients with a positive mpMRI (PI-RADS 3–5) are scheduled for either MR-guided inbore biopsy or TRUS-biopsy, the preferred method depending on the targets defined on the mpMRI, in the following manner: Lesions considered potentially deterministic for prognosis and treatment choice are defined as biopsy targets, with a maximum of three targets for practical reasons. In case of heterogeneous intratumoral signal characteristics on diffusion-weighted images (DWI) or dynamic contrast-enhanced images (DCE), the area that is suspected to correlate to highest tumor aggressiveness is defined as a separate biopsy target. Only in the case of a high probability of hitting all the defined targets is TRUS-biopsies considered the preferred method. At our institute this currently generates approximately 6 MR-guided biopsies weekly.

	PI-RADS 1+2	PI-RADS 3	PI-RADS 4+5
Group size	**43%**	**8%**	**49%**
% cancer	**1%**	**27%**	**91%**
Gleason score 6	1%	20%	33%
Gleason score 7a	0	7%	30%
Gleason score 7b or higher	0	0	28%

Table 1: Performance of diagnostic mpMRI at our institute. Retrospective data collected for quality assurance purposes (189 patients). Numbers represent highest Gleason score found during completed diagnostic workup or in prostatectomy specimens.

System and workflow

For the MR-guided biopsies we use a MAGNETOM Skyra 3T system and Soteria's Remote Controlled Manipulator (RCM)[1], a pneumatically driven robotic device that allows for precise needle guide steering from the operator room (Fig. 1).

Oral antibiotic prophylaxis and an enema are the only preparations for the biopsy procedure. For the procedure the patient is placed in the prone position on the MR table and a needle guide is inserted in the rectum and subsequently connected to the RCM (Fig. 2). Image guidance is done with TrueFISP, alternatively short T2w TSE, sequences and when deemed beneficial, diffusion-weighted imaging (Case 3). Images are send from the MR console to the RCM software, which then allows for quick and easy calibration and thereafter manipulation of the needle guide position (Fig. 3). When the images show satisfactory needle guide positioning, a biopsy needle is inserted into the needle guide at appropriate depth and the biopsy taken.

[1] The information shown herein refers to products of 3rd party manufacturers (Soteria) and thus are in their regulatory responsibility. Please contact Soteria for further information.

Figure 1: The RCM-system. **(1A)** MRI-compatible robotic device that holds and manipulates the position of the needle guide. **(1B)** Cart that is positioned outside of the MRI-room and connected to the robotic device by plastic tubing, containing a steering unit, compressor and vacuum pump. The system includes a portable laptop with the control and targeting software.

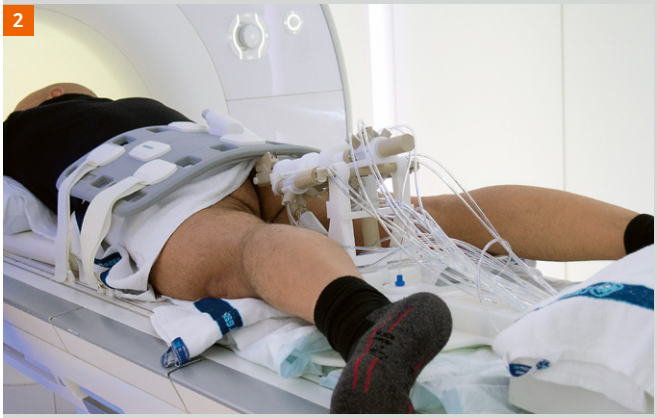

Figure 2: Patient and RCM positioning.

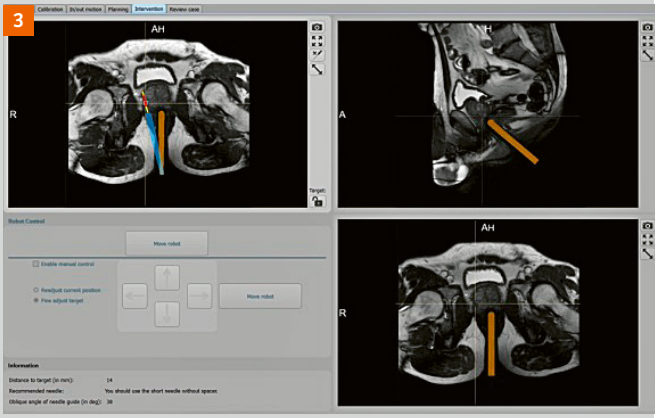

Figure 3: Software interface.

Usage of an MR-compatible biopsy needle permits for image documentation of the needle position. However, in our experience the procedure allows for such accurate needle positioning that this step is superfluous in most cases. By routinely using ordinary biopsy needles we save both time and money.

Procedure time varies with lesion size, location and especially number. In the majority of our cases a door-to-door time of 30 minutes is achieved, but since somewhat longer procedures do occur quite regularly, we currently schedule 40 minutes per patients.

Experiences

Patients generally tolerate the procedure very well. The prone position can become somewhat uncomfortable for the shoulders, but due to predominantly short procedure times this rarely creates significant problems.

Learning to use the RCM system has been quite easy and right from the start we have been able to perform accurate biopsies. Obtaining short procedure times required some experience for both radiologists and technologists, but was achieved rather quickly.

All our targets have been reachable with the system. Biopsy precision is logically dependent on the operator's ability to correctly identify the target and readiness to aim accurately, but the RCM enables the operator to achieve a very high level of precision. In our experience, even the smallest of targets, in all locations in the prostate, are consistently hit (e.g. Case 1).

In approximately 85% of our biopsy cases cancer is found. In the benign cases the mpMRI findings are usually equivocal and the confident needle positioning routinely allows for considering the benign histology to be representative.

In addition to high detection rates, we experience three further important advantages of the high accuracy. First, targeting of more than one lesion and precise targeting of the tumor center or intratumoral areas suspicious of higher-grade cancer regularly generates higher final Gleason scores (Case 2). Second, the technique clarifies mpMRI findings, which increases to total accuracy of the diagnostics. Third, concise learning feedback to the diagnostic imaging is generated, which is highly valuable given the evolving pivotal role of mpMRI in clinical management of probable prostate cancer.

Conclusions

The RCM facilitates targeted MR-guided biopsies of the prostate with very high precision and confidence in a time-efficient manner. Providing high-quality diagnostic mpMRI,

Case 1

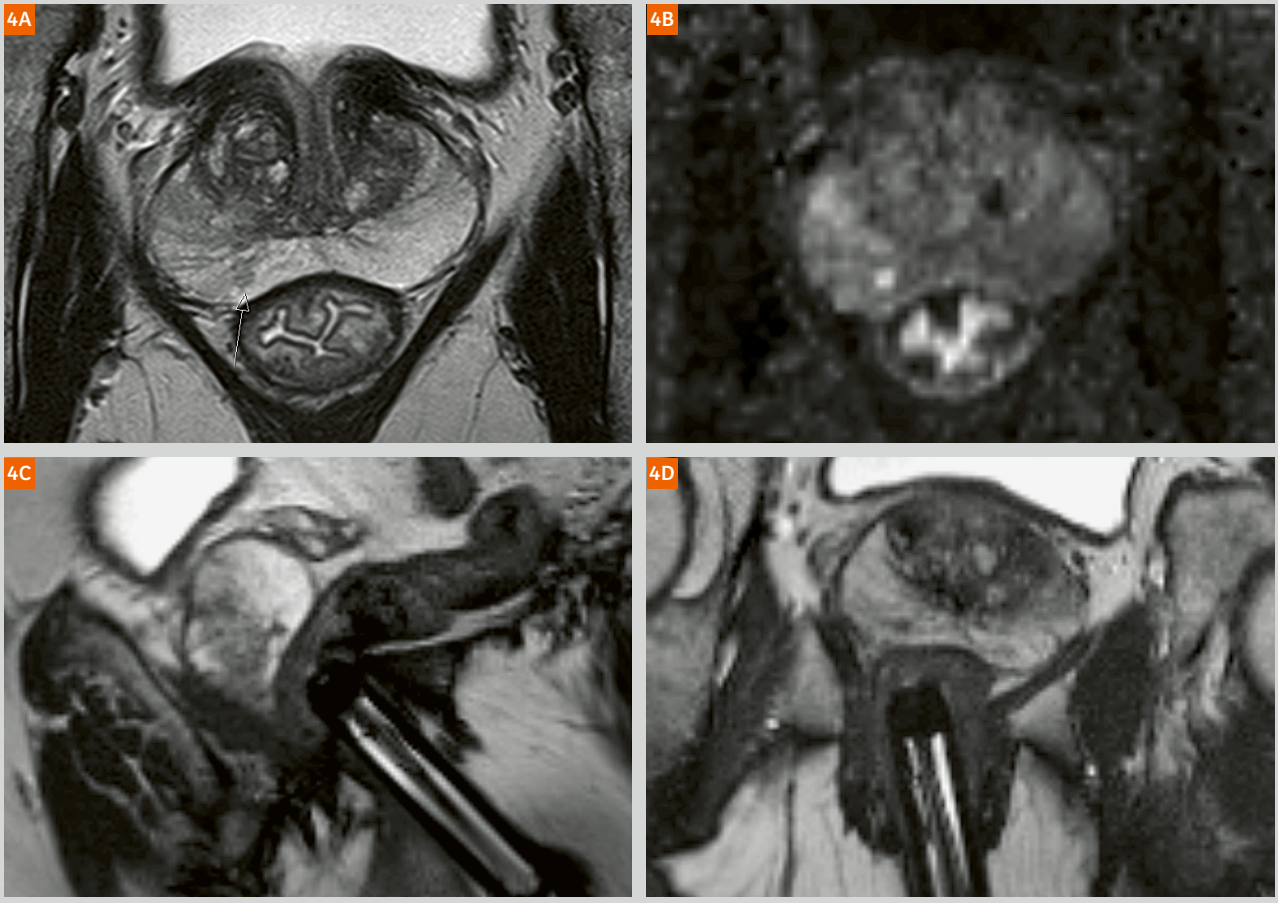

Figure 4: 65-year-old patient with PSA level 4.4.

Diagnostic mpMRI showed a 3 mm highly tumor suspicious lesion in the peripheral zone of the right midgland and additionally typical prostatitis changes anterolaterally mainly on the right side.

MR-guided biopsies revealed prostate cancer Gleason grade 4+3.

4A) Diagnostic mpMRI, transversal TSE T2w.
4B) Diagnostic mpMRI, transversal calculated b1500 images (RESOLVE diffusion).
4C) TrueFISP sagitally along the axis of the biopsy needle guide pointing at the target.
4D) TrueFISP transversally along the axis of the biopsy needle guide pointing at the target.

this allows for routine application of a one-stop, definitive biopsy strategy that aims at accurately mapping prostate cancer. Our center performs RCM-biopsies whenever they are expected to outperform TRUS-biopsies in the challenging task of detecting and delineating the clinical significance of prostate cancer, i.e. in the majority of our patients. With this, the system has revolutionized our practice and empowered us to improve and further develop stratification of our patients. A hope for the future is that improvements in histological grading and molecular testing of tumor tissue [6, 7], combined with optimized biopsies, will lead to further improvements in prognostication.

References

1 Bell, Katy J. L., Del Mar, Chris, Wright, Gordon, Dickinson, James & Glasziou, Paul. 2015. Prevalence of incidental prostate cancer: A systematic review of autopsy studies. International Journal of Cancer. Journal International du Cancer 137: 1749-1757.
2 Resnick, Matthew J., Koyama, Tatsuki, Fan, Kang-Hsien, Albertsen, Peter C., Goodman, Michael, Hamilton, Ann S., Hoffman, Richard M.,

Case 2

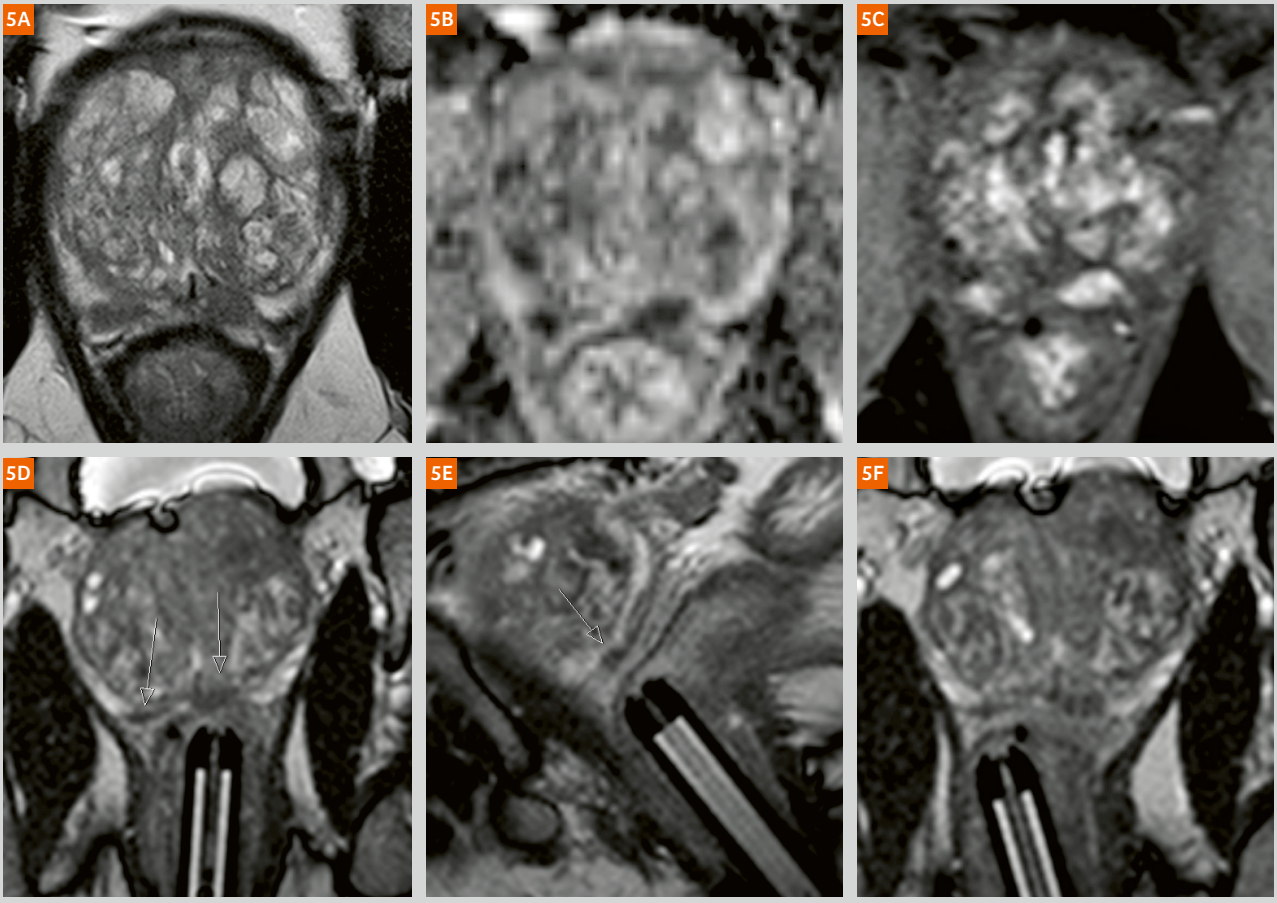

Figure 5: 63-year-old patient with PSA level 6.0, referred to our center for MR-guided biopsies after negative MR-US Fusion-guided biopsies at an external institute.

Diagnostic mpMRI showed a large prostate (estimated volume 128 ml) and apically bilateral relatively small, but highly tumor suspicious lesions.

Both lesions were targeted with MR-guided biopsies. Histology revealed prostate cancer Gleason grade 4+3 on the left side and Gleason grade 4+5 on the right side.

5A) Diagnostic mpMRI, transversal TSE T2w.
5B) Diagnostic mpMRI, transversal ADC map (RESOLVE diffusion).
5C) Diagnostic mpMRI, initial contrast uptake phase of transversal DCE (Twist VIBE).
5D) TrueFISP transversally along the axis of biopsy needle guide pointing at the target on the left side.
5E) TrueFISP sagittaly along the axis of the biopsy needle guide pointing at the target on the right side.
5F) TrueFISP transversally along the axis of the biopsy needle guide pointing at the target on the right side.

Potosky, Arnold L., Stanford, Janet L., Stroup, Antoinette M., Van Horn, R. Lawrence & Penson, David F.. 2013. Long-Term Functional Outcomes after Treatment for Localized Prostate Cancer. The New England journal of medicine 368: 436-445.

3 de Rooij, M., Hamoen, E. H., Futterer, J. J., Barentsz, J. O. & Rovers, M. M.. 2014. Accuracy of multiparametric MRI for prostate cancer detection: a meta-analysis. AJR Am J Roentgenol 202: 343-51.

4 Ahmed HU. The PROMIS study: a paired-cohort, blinded confirmatory study evaluating the accuracy of multi-parametric MRI and TRUS biopsy in men with an elevated PSA. J Clin Oncol 2016; 34: (suppl; abstr 5000).

5 Pokorny, M. R., de Rooij, M., Duncan, E., Schroder, F. H., Parkinson, R., Barentsz, J. O. & Thompson, L. C.. 2014. Prospective study of diagnostic accuracy comparing prostate cancer detection by transrectal ultrasound-guided biopsy versus magnetic resonance (MR) imaging with subsequent MR-guided biopsy in men without previous prostate biopsies. Eur Urol 66: 22-29.

6 McKenney, Jesse K., Wei, Wei, Hawley, Sarah, Auman, Heidi, Newcomb, Lisa F., Boyer, Hilary D., Fazli, Ladan, Simko, Jeff MD, Hurtado-Coll, Antonio, Troyer, Dean A., Tretiakova, Maria S., Vakar-Lopez, Funda, Carroll, Peter R., Cooperberg, Matthew R., Gleave, Martin E., Lance, Raymond S., Lin, Dan W., Nelson, Peter S.,

Case 3

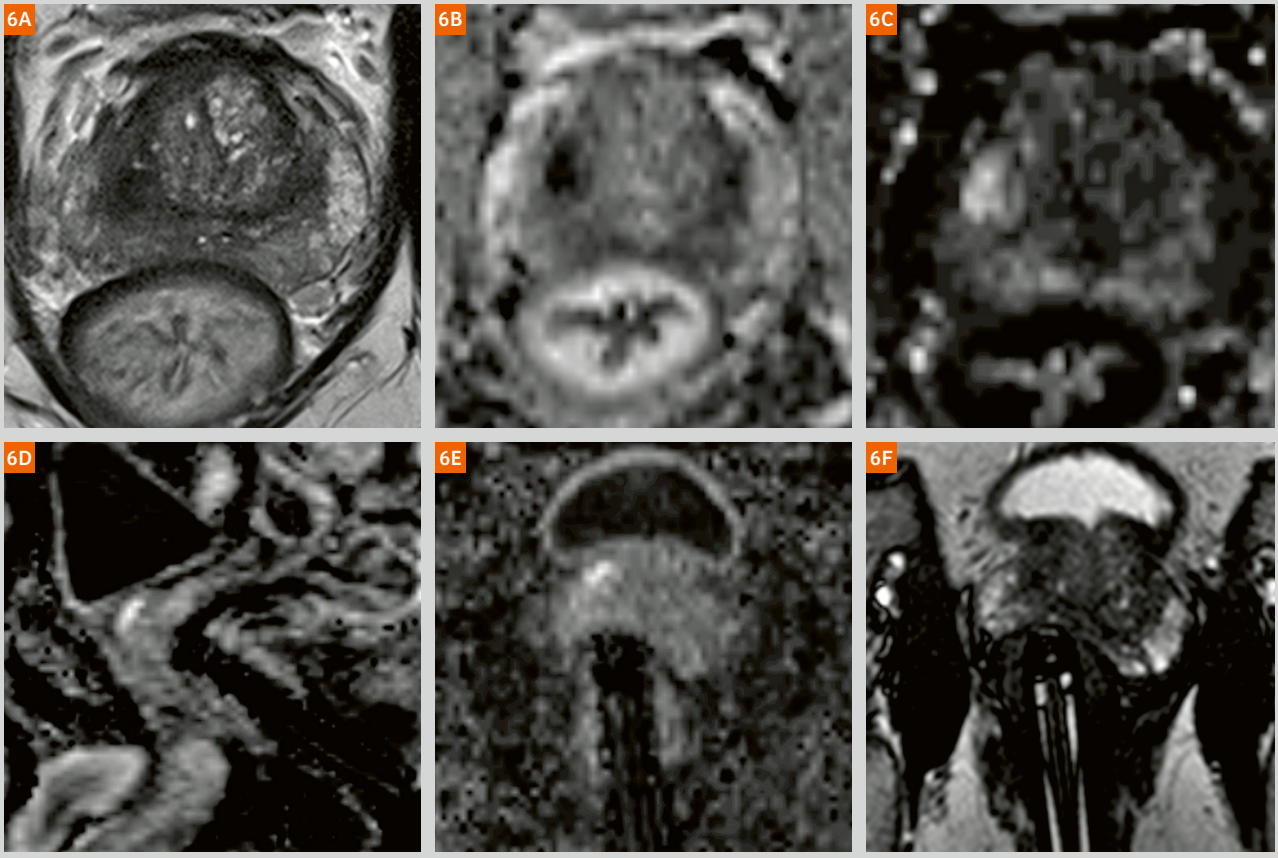

Figure 6: 63-year-old patient with PSA level 5.3.

Diagnostic mpMRI showed an 8 mm tumor suspicious lesion in the transitional zone of the right basal gland.

During the MR-guided biopsy procedure the lesion was hard to localize on TrueFISP and TSE T2 images, but possible to target confidently with the use of diffusion-weighted images.

Histology revealed prostate cancer Gleason grade 3+4.

6A) Diagnostic mpMRI, transversal TSE T2w.
6B) Diagnostic mpMRI, transversal ADC map (RESOLVE diffusion).
6C) Diagnostic mpMRI, transversal calculated b3000 images (RESOLVE diffusion).
6D) Calculated b1500 images (RESOLVE diffusion) sagittaly along the axis of the biopsy needle guide pointing at the target.
6E) Calculated b1500 images (RESOLVE diffusion) transversally along the axis of the biopsy needle guide pointing at the target.
6F) TrueFISP transversally along the axis of the biopsy needle guide pointing at the target.

Thompson, Ian M., True, Lawrence D., Feng, Ziding, Brooks, James D. 2016. Histologic Grading of Prostatic Adenocarcinoma Can Be Further Optimized: Analysis of the Relative Prognostic Strength of Individual Architectural Patterns in 1275 Patients From the Canary Retrospective Cohort. Am J Surg Pathol 2016 Nov;40(11):1439-1456.

7 Hoogland, A. Marije, Kweldam, Charlotte F. and Van Leenders, Geert J. L. H.. Prognostic Histopathological and Molecular Markers on Prostate Cancer Needle-Biopsies: A Review. BioMed Research International, vol. 2014, Article ID 341324.

Contact

Jeroen Reijnen
Radiology Department
Sørlandet Hospital Kristiansand

Egsveien 1000
Postboks 416
4604 Kristiansand
Norway
Phone: +47 97799733
Jeroen.Sebastiaan.Reijnen@sshf.no

Jon Bache Marthinsen, Jeroen Reijnen, Frank Gonzalez

PI-RADS 2.1 Standardized Prostate MRI Reporting

David Jean Winkel, M.D. and Hanns-Christian Breit, M.D.

University Hospital Basel, Switzerland

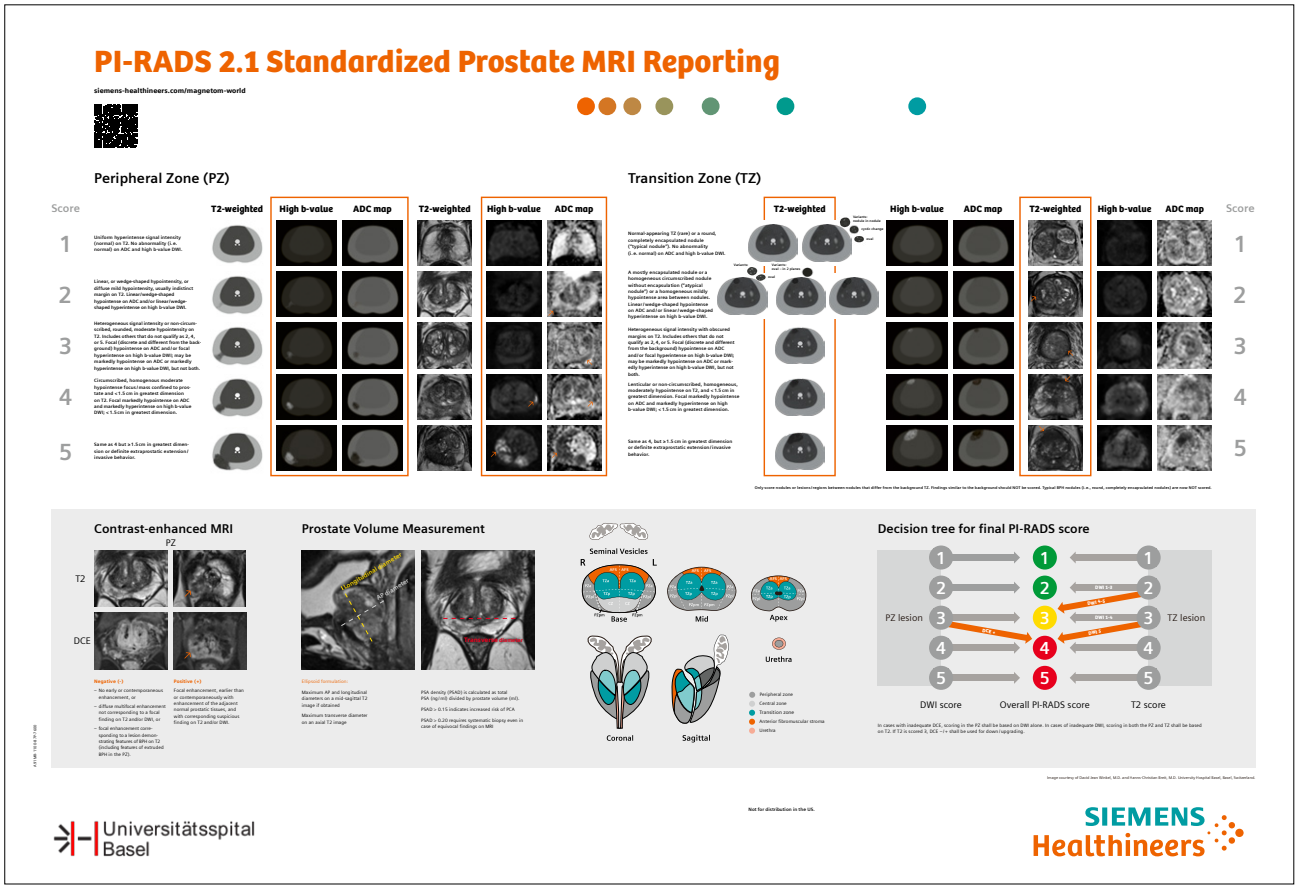

Get your free copy of the PI-RADS poster at

www.magnetomworld.siemens-healthineers.com/publications/subscriptions/mri-poster

MR-based Synthetic CT. An AI-based Algorithm for Continuous Hounsfield Units in the Pelvis and Brain – with *syngo*.via RT Image Suite

Michaela Hoesl, Ph.D.; Nuria Escobar Corral, Ph.D.; Nilesh Mistry, Ph.D.

Siemens Healthineers

Why MRI in radiotherapy?

Radiotherapy treatment simulation and planning are conventionally performed on computed tomography (CT) images because of the intrinsic relationship between Hounsfield units (HU) and electron density information, needed to model radiation attenuation in the treatment planning system [1]. Compared with CT images, MRI shows superior soft-tissue contrast (Fig. 1) and is becoming the modality of choice for delineation of target organs and organs at risk (OAR) [2]. Moreover, MRI gives access to multiparametric data, such as T1w, T2w, dynamic contrast-enhanced MRI (DCE-MRI), and diffusion-weighted imaging (DWI) [3–7], which play an increasingly important role in the whole workflow from diagnosis, structure delineation, treatment planning, and response assessment.

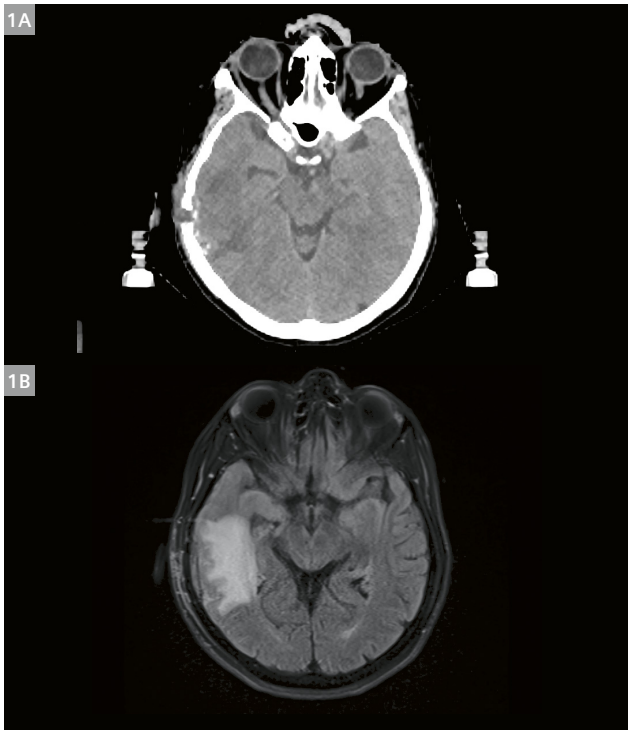

1 **(1A)** CT, **(1B)** MRI (T2 FLAIR)
Courtesy of Universitätsklinikum Erlangen, Germany.

Dose calculation

Dose calculation requires a 3D electron or mass density map and unfortunately the necessary correlation between the nuclear magnetic properties and electron density is missing. Therefore, MR images cannot directly be used for dose calculation. When MR images are used for contouring, a CT image is required for dose calculation, resulting in a combined MRI-CT workflow.

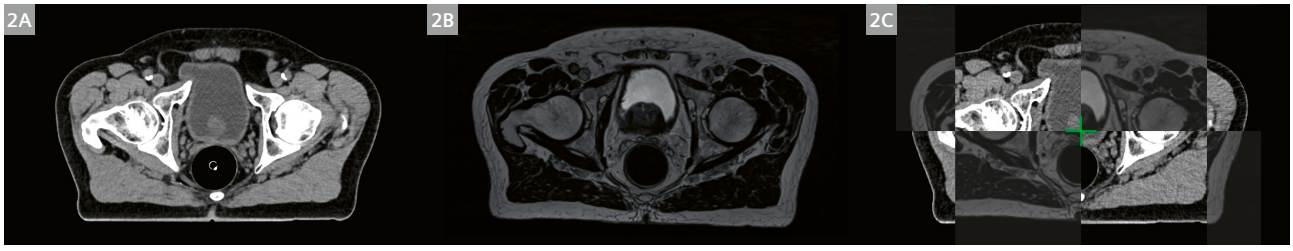

2 **(2A)** Planning CT, **(2B)** T2w MRI, **(2C)** registration visualized with the checkerboard tool[1]. Registration errors may persist and registration can be cumbersome. *Courtesy of Universitätsklinikum Erlangen, Germany.*

[1]*Since syngo.via RTiS VB60.*

Main challenge of a combined MRI-CT workflow

In multimodality workflows, rigid and sometimes deformable image registration (DIR) are employed. When anatomies deviate significantly (bladder filling or rectal filling, Fig. 2) fusing of CT and MRI modalities becomes difficult and adds to uncertainties in the planning process [8, 9].

MR-only workflow for the pelvis and brain

The MAGNETOM Sola (1.5T) and MAGNETOM Vida (3T)[2] are our MRI systems supporting MR-only workflows. Both MAGNETOM RT Pro edition systems are dedicated to RT with continuous development and updates with the latest features for RT simulation:

- Reproducible patient positioning with MR-compatible, certified, and indexed flat tabletop overlays, immobilization devices, and an external laser bridge
- Flexible coils with multiple channels
- RT Dot Engine with dedicated RT protocols including workflow guidance
- Automatic, optimal (2D/3D) distortion correction for spatial integrity for robustness and reproducibility
- QA solutions including an in-depth guide: QA cookbook [10]
- MR-based Synthetic CT with continuous HU

An example of an MR-only workflow protocol for pelvis is shown in Figure 3. The key sequence for MR-based Synthetic CT reconstruction, the T1 VIBE-Dixon sequence, follows the optional T1w and T2w clinical sequences for morphological information precontrast and postcontrast. Additional sequences, such as, for example diffusion-weighted images (DWI), can be acquired to obtain further insights and support target definition [18].

Advanced sequences like DWI can potentially be used for treatment response evaluation [11].

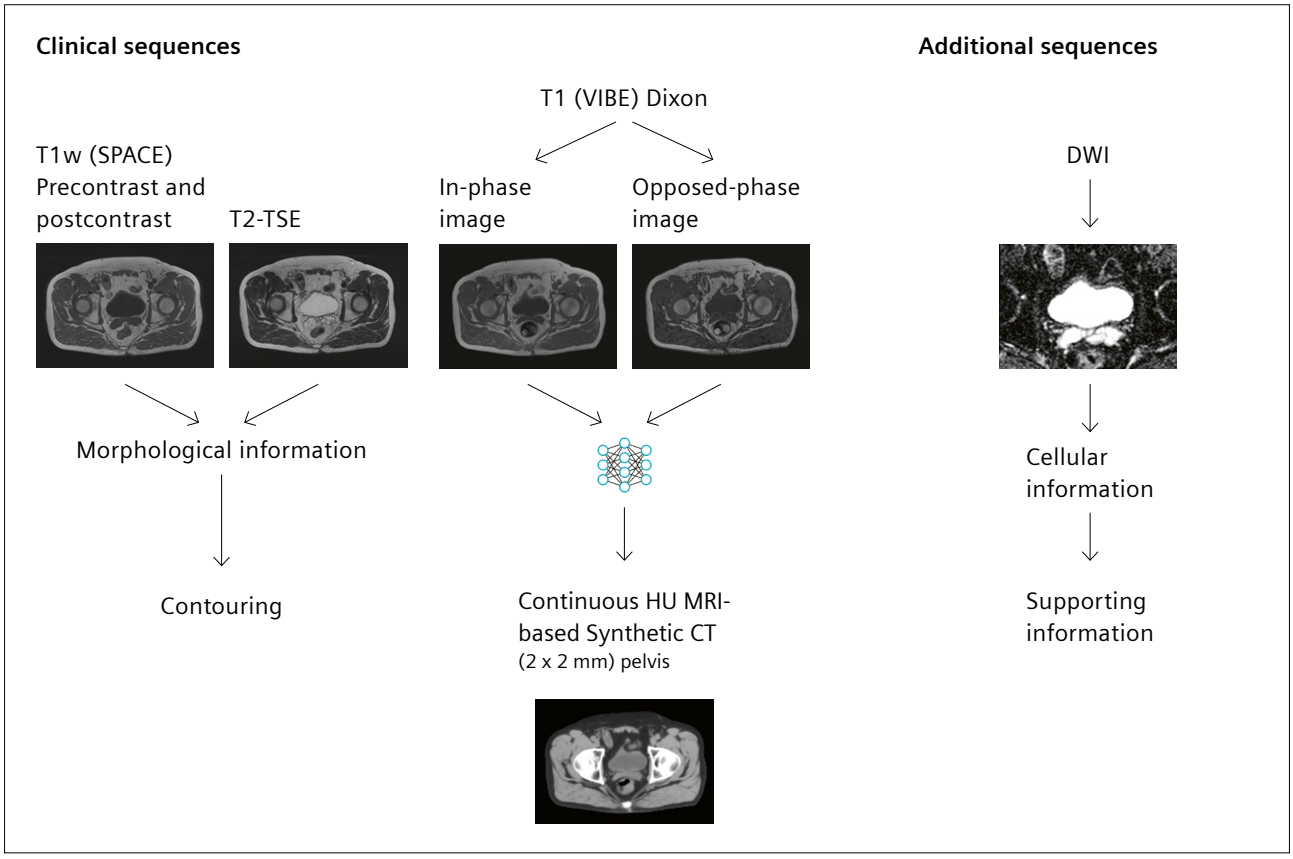

3 Example of a scanning protocol for a prostate MR-only workflow. *Courtesy of Universitätsklinikum Erlangen, Germany.*

[2]*The data acquisition protocols for Synthetic CT are available with syngo MR XA11A and later software versions with MAGNETOM RT Pro edition for MAGNETOM Vida and MAGNETOM Sola, with syngo XA30 and later software Versions for MAGNETOM Aera and MAGNETOM Skyra.*

MR-based Synthetic CT generation algorithm – How does it work?

In recent years, the field of MR-based Synthetic CT imaging has gained substantial interest [12–17]. Different methods have been proposed to create electron density information from MRI artificially [15, 18]. Our latest algorithm for MR-based Synthetic CT is an AI-based algorithm. The model was trained by leveraging deep learning (DL) neural network technology. The DL algorithm uses a combination of multilayer neural networks to learn Synthetic CT reconstruction. Training was accomplished using a large number of datasets for training with 6486 CT and MRI image pairs for brain and 9059 for pelvis (validation sets were 553 for brain and 695 for pelvis). For the training image pairs, CT images were registered to MRI using rigid and deformable registration. The input for the trained deep learning algorithm are only the VIBE-Dixon in-phase and opposed-phase images for Synthetic CT reconstruction. The AI-based Synthetic CT product comes fully trained to the user and does not continue training at the user's site.

The network architecture (Fig. 4) consists of two parts:
Network 1: convolutional neural network (densely connected UNet) for segmentation in three classes: background, bone, and soft tissue from a two-channel input using the MR images.

Network 2: generator and discriminator (conditional GAN) for Synthetic CT reconstruction with continuous HU (one output channel). During training, the input and condition are the MR images concatenated with the segmentation results of the first network (five input channels) to guide the training of the conditional GAN.

- Generator (densely connected UNet): receives a five-channel input (in-phase, opposed-phase Dixon MRI and the segmentation output in three tissue classes) for Synthetic CT reconstruction.
- Discriminator: tries to discriminate the prediction of the generator (Synthetic CT) from the ground truth (real CT image). During training, the information is fed back iteratively to yield a machine-generated Synthetic CT, which is indistinguishable from a real CT image.

VIBE Dixon acquisition for MR-based Synthetic CT reconstruction

MR scanning parameters for the VIBE-Dixon sequence as input for Synthetic CT reconstruction are automatically handled in the RT Dot Engine.
In the RT Dot Engine, axial orientation reformatting and distortion correction are automatically preselected. The neural network imposes certain requirements on the input data. The network expects MR volume pairs in axial orien-

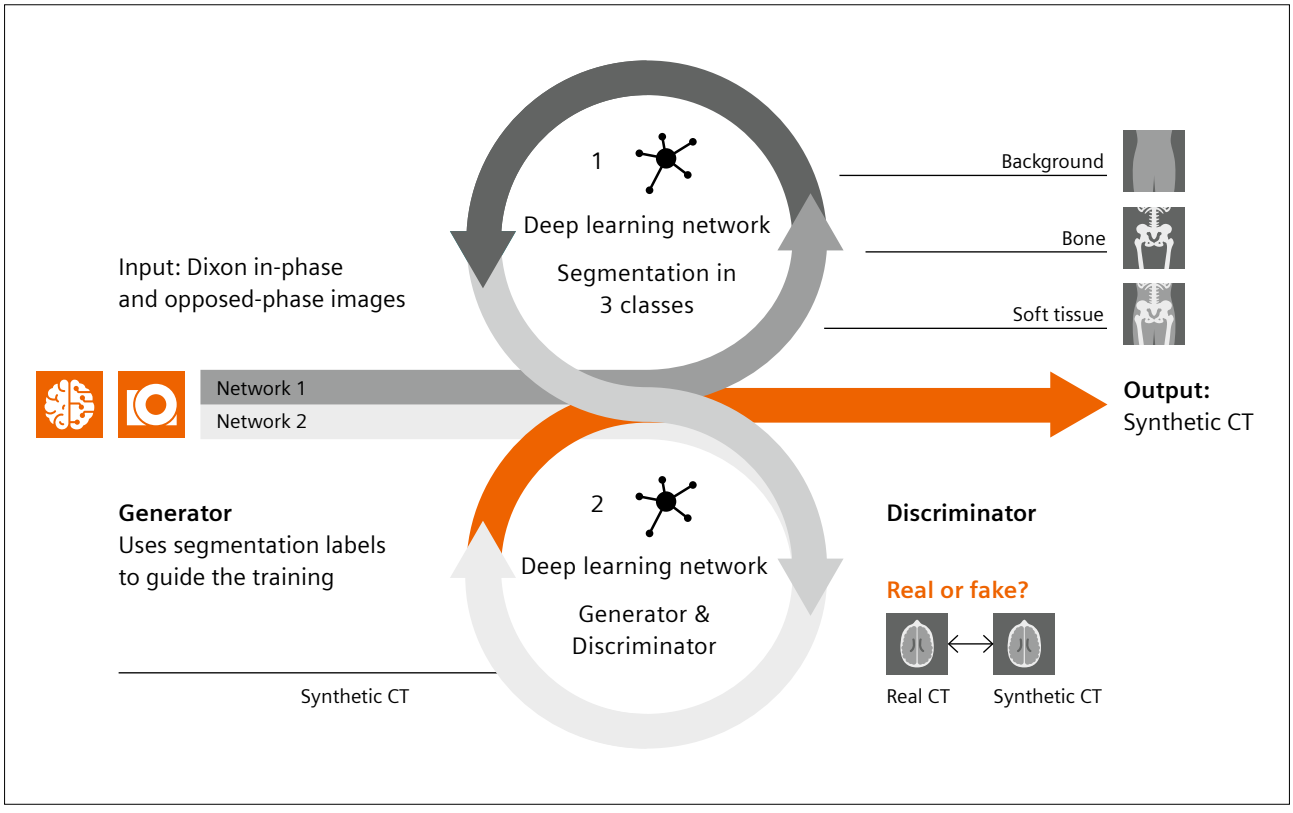

4 The cGAN (conditional generative adversarial network) training scheme.

tation. Therefore, volumes are always reformatted to axial orientation. The fully trained network requires input images with dimensions (in x-axis and y-axis) in multiples of 16, which is also pre-selected in the RT Dot Engine. Otherwise, zero padding is performed before the synthesis. Additionally, input images need 98th percentile normalizations, which is done automatically in the postprocessing pipeline.

The resulting Synthetic CT has an in-plane resolution of 1 × 1 mm (brain) and 2 × 2 mm (pelvis). The slice thickness is determined by the acquired input data.

Synthetic CT import in the treatment planning system

The generated MR-based Synthetic CT image can be exported in HU, relative electron density (RED), and relative mass density (RMD). When exported as HU, for dose calculation the HU values of the synthetic CT have to be converted to RED or RMD in the TPS. For this purpose, the following table can be used. If RED and RMD are chosen as output, the calibration table is automatically applied by the software. The MR-based Synthetic CT image is labeled in DICOM as "CT" and is therefore recognized by the TPS and LINAC as a CT image.

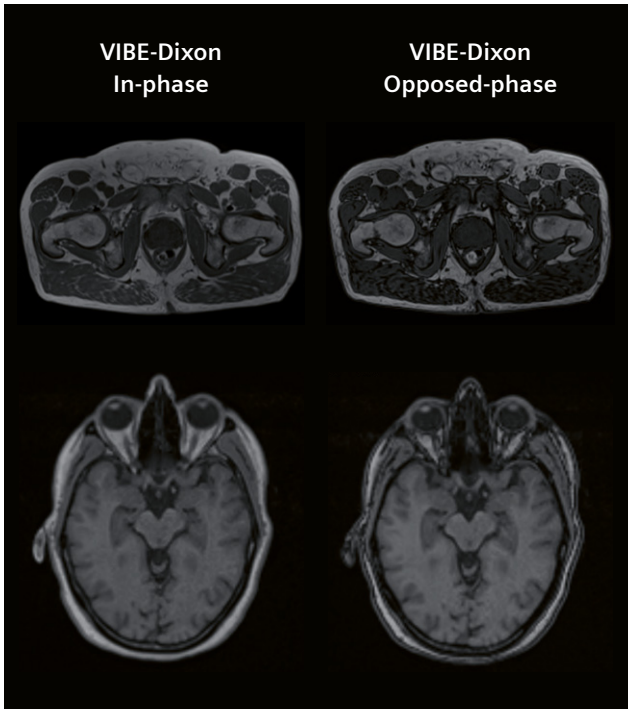

5 VIBE-Dixon in-phase and opposed-phase images of a male pelvis and brain.

T1 VIBE Dixon	1.5T acquisition time	Resolution	3T acquisition time	Resolution
Head	3 min 25 s	1.5 × 1.5 × 1.5 mm³	2 min 22 s	1.3 × 1.3 × 1.0 mm³
Pelvis	2 min 21 s	2.0 × 2.0 × 2.0 mm³	1 min 33 s	2.0 × 2.0 × 2.0 mm³
	4 min 12 s	1.6 × 1.6 × 2.0 mm³	2 min 48 s	1.6 × 1.6 × 2.0 mm³

Table 1: T1 VIBE-Dixon sequence with example acquisition time and image resolution at 1.5T and 3T for brain and pelvis: For pelvis, the acceleration mode CAIPIRINHA [18] was selected with a total acceleration factor of 4–5. For the brain at 1.5T, no acceleration mode was used. At 3T, GRAPPA [19] with a total acceleration factor of 2 was selected.

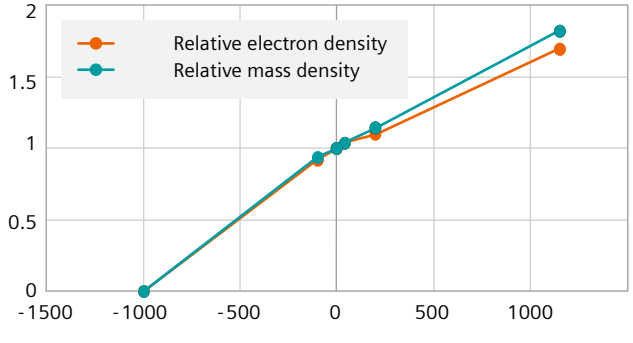

Tissue class	HU value	Relative electron density	Relative mass density
Air	-1000	0	0
Fat	-100	0.924	0.941
Liquid	0	1	1
Brain/muscle	40	1.04	1.04
Spongeous bone	200	1.096	1.143
Cortical bone	1150	1.695	1.823

6 Synthetic CT calibration curve.

MR-based Synthetic CT results for pelvis and brain

In Figure 7, an example of the results obtained for pelvis and brain are shown. Both the soft-tissue window level and bone window level are presented. Besides dose planning, Synthetic CT can be used to verify the patient's position on the LINAC by matching the Synthetic CT with the cone-beam CT or the 2D synthetic DRR (derived from the Synthetic CT) with the flat-panel radiograph (Fig. 8).

Evaluation of geometric fidelity and CT number accuracy

We performed an internal validation of geometric fidelity and HU accuracy. The geometric fidelity test was passed for both brain and pelvis with an average symmetric surface distance (ASSD) of less than 1 mm (0.9 ± 0.1 mm pelvis, 0.8 ± 0.1 mm brain), which is below the in-plane pixel resolution of 1 mm (2 mm) for the brain (pelvis) and therefore negligible. For HU accuracy, line profiles from CT and MR-based Synthetic CT from the same patient were compared. An example of this comparison is shown in Figure 9. In addition to that, the HU values of the MR-based Synthetic CT were evaluated in multiple 2D regions of interest (ROI) of the tissue types: fat, liquid, soft tissue, and bone and were each compared with the expected literature values. All values, including deviations, fell within the expected range and tolerance (Table 2).

For visual inspection of geometric accuracy, *syngo*.via RTiS VB 60 provides a checkerboard tool (Fig. 11A). The HU can be verified in regions of interest using the ROI tool, see Figure 11B.

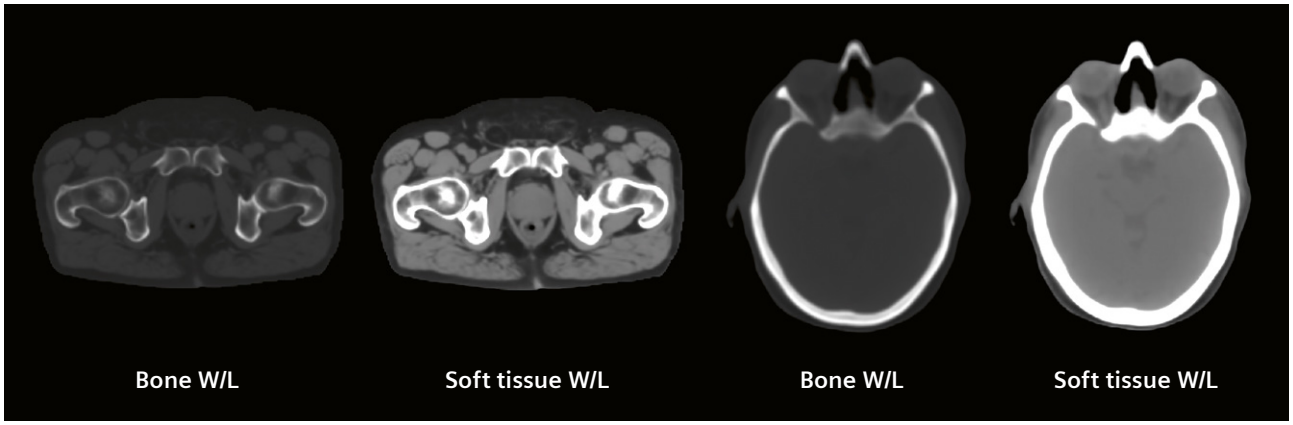

7 Synthetic CT for the pelvis and brain in two different window levels (W/L): bone and soft tissue.

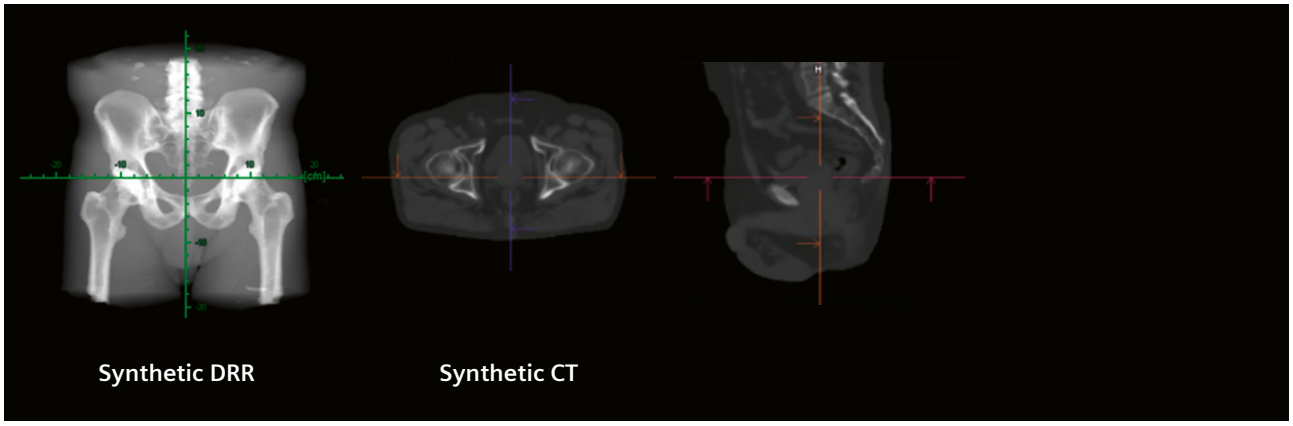

8 Synthetic DRR for matching with DRR and Synthetic CT for matching with cone-beam CT images for patient positioning.

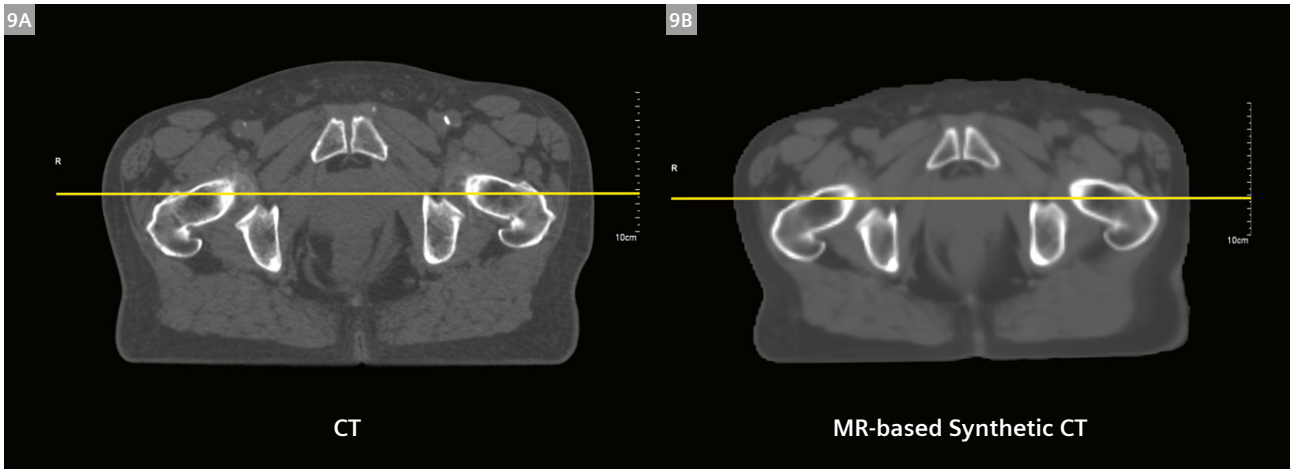

9 **(9A)** Planning CT, **(9B)** MR-based Synthetic CT and graph comparing HU along the line profile (yellow lines).
Courtesy of Centre Hospitalier de l'Université de Montréal – CHUM, Montreal, Canada.

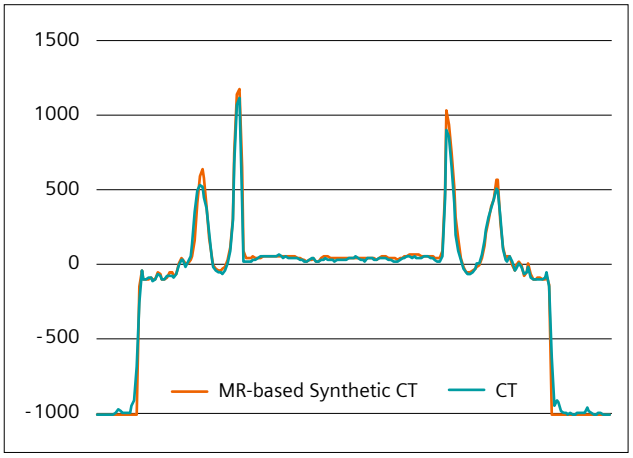

10 Line profile comparison.

ROI	Reference values[3]	Measured in brain	Measured in pelvis
Fat	-100 ± 50	-59 ± 4	-97 ± 1
Liquid (ventricles, bladder)	0 ± 50	7 ± 1	8 ± 2
Soft tissue (brain, muscle)	40 ± 50	27 ± 1	44 ± 2
Cortical bone (skull, femoral head)	1150 ± 200	1103 ± 59	1236 ± 17
Spongeous bone (femoral shaft)	200 ± 200	–	277 ± 9

Table 2: Hounsfield unit (HU) comparison of the MR-based Synthetic CT in multiple regions of interest (ROI) of different tissue types with expected literature values.

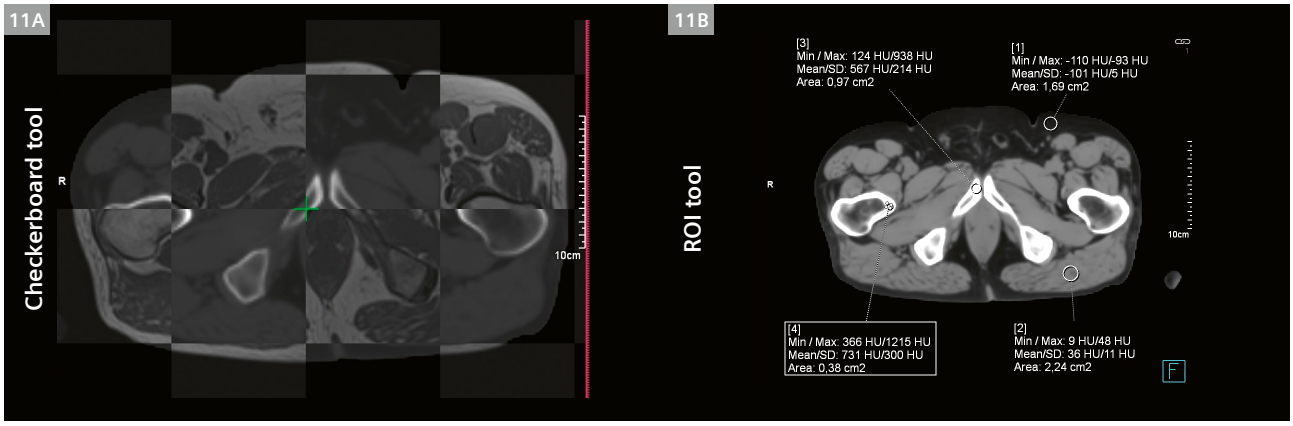

11 Geometric accuracy and HU value verification with checkerboard inspection and ROI tool in a pelvic case.

[3]*Reference values match the CT lookup table (Table 1).*

Clinical evaluation

Dose difference evaluation between the CT and Synthetic CT is the crucial metric for radiation therapy. The dosimetric and spatial positioning evaluation of the new algorithm relative to standard CT-based planning was performed by two independent clinical partners.

Summary

1. Evaluation of the pelvic MR-based Synthetic CT from Brigham & Women's Hospital, Dana-Farber Cancer Institute, Harvard Medical School, Boston, MA, USA[4]
Overall, differences between the original dose distribution and the dose recalculated on the Synthetic CT were: < 1% dose difference in the CTV and evaluated OAR for the seven prostate patients examined. The mean dose difference (ΔDose = Dose (planning CT) – Dose (registered Synthetic CT)) from the CTV was -0.21% relative to total dose.

- 1%/2 mm gamma analysis showed mean agreement of 98.9 ± 0.3% (range 98.4–99.3%).

Regarding spatial positioning evaluation, 0.12 mm/ -0.72 mm/-0.56 mm differences in x-, y-, and z-direction (range: -1.8–1.4 mm) between registered Synthetic CT to CBCT registration and planning CT-CBCT registration.

2. Evaluation of the brain MR-based Synthetic CT from Universitätsklinikum Erlangen, Germany
The mean dose difference was computed and analyzed for all patients for the target volumes (PTV, GTV) and the evaluated organs at risk (brainstem, chiasma, optical nerves).

- < 1% mean dose difference (normalized to the total planned dose) in all the regions of interest
- < 1% (median 0.06%) mean dose differences of PTV and GTV
- < 0.5% and 1.4% mean dose difference for the brainstem and chiasma respectively

[4] *The clinical evaluation was performed on a prototype; its algorithm does not deviate from the released product.*

Full evaluation

1. Evaluation of the pelvic MR-based Synthetic CT from Brigham & Women's Hospital, Dana-Farber Cancer Institute, Harvard Medical School, Boston, MA, USA
A total of seven prostate cancer patients scheduled for subsequent EBRT underwent same-day MRI (MAGNETOM Vida 3T) and CT (SOMATOM Confidence) simulation. All patients were clinically planned and treated using their planning CT scanner. Parameters were as follows:

- CT: 0.976 × 0.976 mm voxel size, 3 mm slice thickness
- MRI: 336 × 448 mm field of view, 2 × 2 mm voxel size, 2 mm slice thickness. T1 VIBE-Dixon Synthetic CT protocol sequence
- TPS: Eclipse 15.6
- Treatment technique: 6 MV X-rays using a VMAT (RapidArc)
- Dose prescription: 180 cGy/fr for 44 fractions. Some patients received simultaneous integrated boosts and altered fractionations.

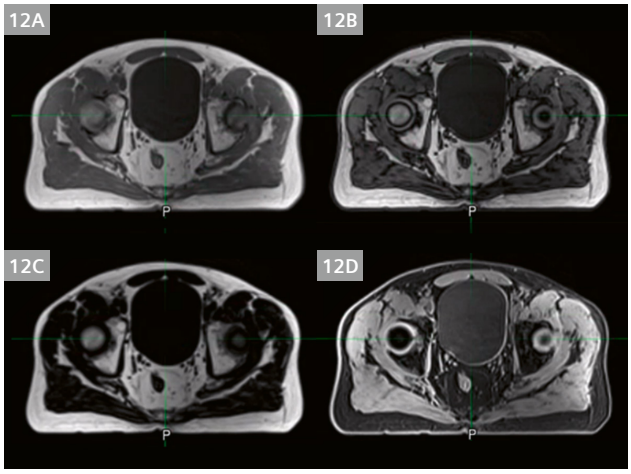

12 Four MR contrasts generated by the T1 VIBE-Dixon scan protocol **(12A)** in-phase (IP), **(12B)** opposed-phase (OP), **(12C)** fat, **(12D)** water. Only 12A and 12B are needed for Synthetic CT postprocessing.

Dosimetric accuracy evaluation of the AI-Synthetic CT
MR-based Synthetic CT images were registered to the planning CT (pCT), resampled and then saved into the frame of reference of the pCT. These registered MR-based Synthetic CTs (called "rsCT" in the following) were then imported into the Eclipse treatment planning system. The clinical treatment plans (based on pCT) were copied and recomputed onto the corresponding rsCT using the same plan parameters. Dose differences were computed in OARs (bladder, rectum, and left and right femoral heads) and the CTV prostate target structure. The original contours (from the pCT scans) were used for all subsequent analyses. Dose distributions obtained using the pCT and the rsCT were compared using a 1%/2 mm gamma criteria [19].

Assessment of spatial localization accuracy (cone-beam CT (CBCT) registration)
Spatial (on treatment) localization accuracy of the Synthetic CT was evaluated by comparing Synthetic CT to CBCT registration results with pCT-CBCT registration in Eclipse/Aria using the Image Registration tool. The first five CBCT scans of each patient were used for this study. Two types of translation-only registrations were performed:

- CBCT scans were registered to the space of the pCT.
- CBCT scans were registered to the space of the rsCT (Synthetic CT registered to the planning CT).

Differences in the translation vectors of the pCT-CBCT registration and rsCT-CBCT registration (e.g., Δx = translation_x(pCT)−translation_x (rsCT)) were calculated and averaged among the five CBCT cases.

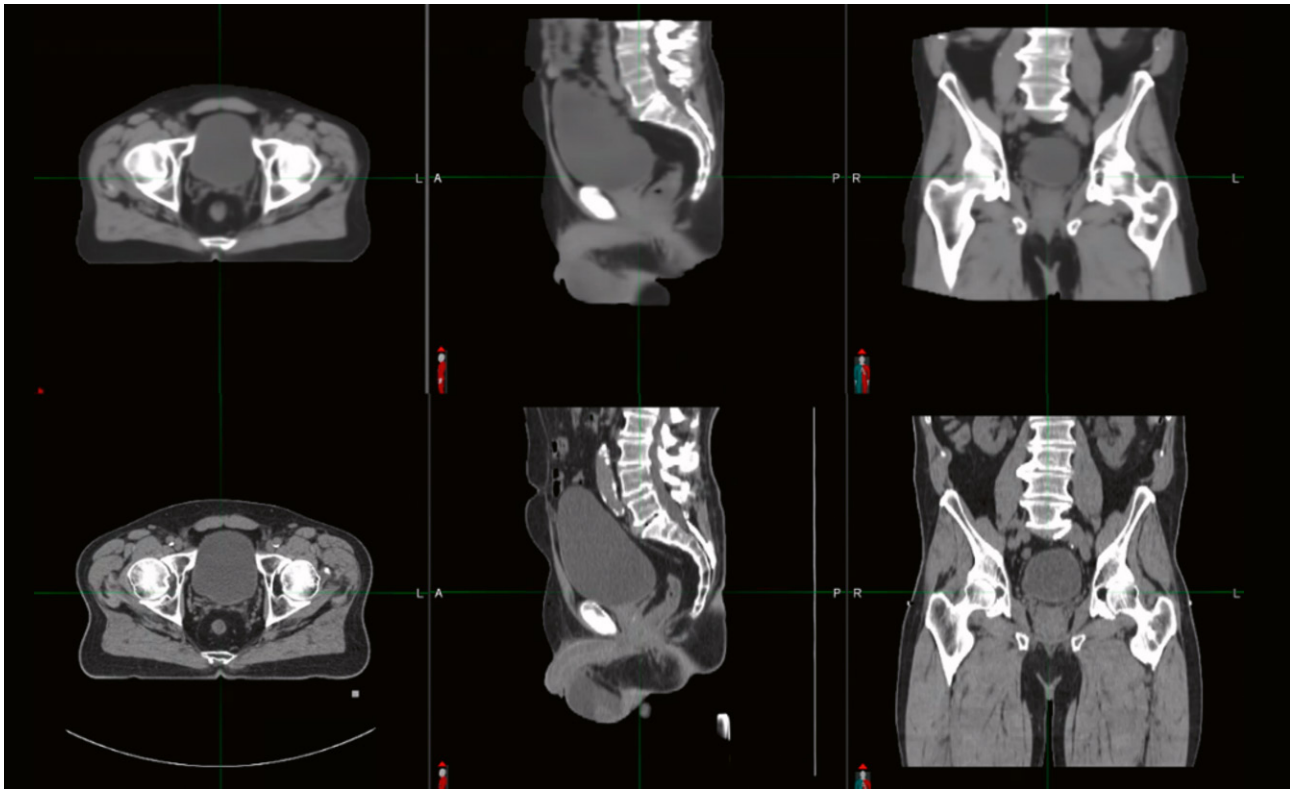

13 MR-based Synthetic CT (top) compared with conventional planning CT (bottom) of the same patient.

Dosimetric results in the pelvis

Differences between the original dose distribution on the pCT and the recalculated dose distribution on the Synthetic CT were globally < 1% for the seven patients examined. The difference in the dose calculated for the prostate (CTV), penile bulb (when contoured), bladder, rectum, and both femoral heads are tabulated in Table 3. The mean dose difference (ΔDose = Dose (pCT)–Dose (rsCT)) to the CTV was -0.21% relative to the total dose. Results of gamma analysis at 1%/2 mm showed a mean agreement of 98.9 ± 0.3% (range 98.4–99.3%).

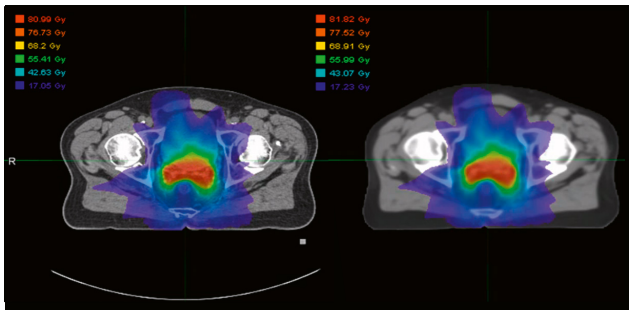

14 Exemplary dose distributions of a treatment plan calculated on the planning CT (left) and the MR-based Synthetic CT (right).

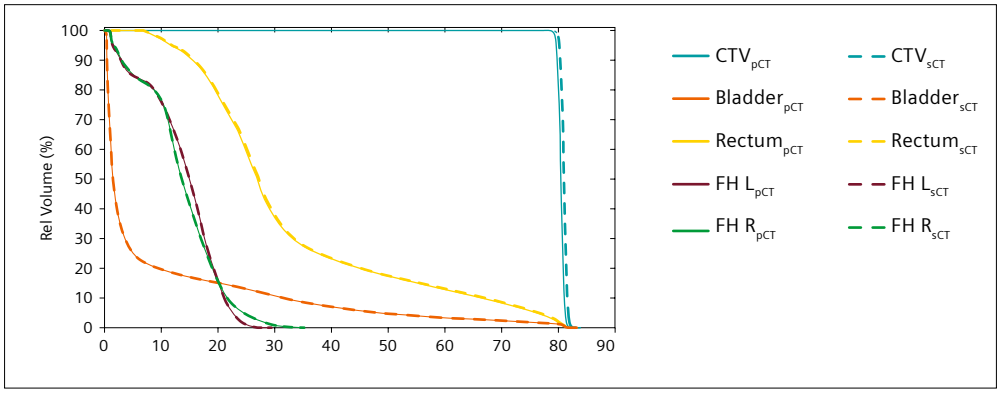

15 Dose volume histograms were compared in CTV and OARs (bladder, rectum, and femoral heads).

Patient	CTV (% difference)	Bladder (Gy)	Rectum (Gy)	Femoral head left (Gy)	Femoral head right (Gy)	Gamma 1%/2mm
1	-0.62%	-0.05	-0.15	-0.04	-0.08	99.1%
2	0.28%	0.02	-0.05	0.19	0.07	98.4%
3	-0.49%	-0.08	-0.31	0.01	-0.05	98.4%
4	-0.74%	-0.43	-0.62	0.06	0.12	99.2%
5	-0.08%	0.03	-0.33	0.07	0.09	99.3%
6	0.58%	-0.03	-0.13	-0.03	-0.03	99.3%
7	-0.30%	-0.01	-0.05	-0.14	-0.05	98.9%
Mean	-0.21%	-0.078	-0.23	0.017	0.01	98.9%
STD	0.44%	0.16	0.20	0.10	0.08	0.3%

Table 3: Differences in dose distributions of pCT- and Synthetic CT-based dose plans. Dose differences in CTV, PTV, and OAR were calculated as ΔDose = Dose(pCT) - Dose(rsCT).

Spatial localization accuracy results (CBCT registration)

Differences between rsCT-CBCT registration results and pCT-CBCT registration were assessed (Table 4). On average, 0.12 mm/-0.72 mm/-0.56 mm in x-, y-, and z-direction respectively (range: -1.8–1.4 mm) were observed.

Patient	1	2	3	4	5	6	7	Mean	STD
X (mm)	1.4	0.46	0.1	-1.3	0.08	-0.36	0.5	0.12	0.83
Y (mm)	-1.1	-1.06	-0.26	-1.22	-0.14	-1.44	0.2	-0.72	0.63
Z (mm)	-1.02	-1.2	-0.56	1.14	-0.48	0	-1.8	-0.56	0.94

Table 4: Difference in the translation vector (mm) between rsCT-CBCT registration and pCT-CBCT registration. Difference was calculated as translation (pCT)–translation (rsCT) in X, Y, Z axes.

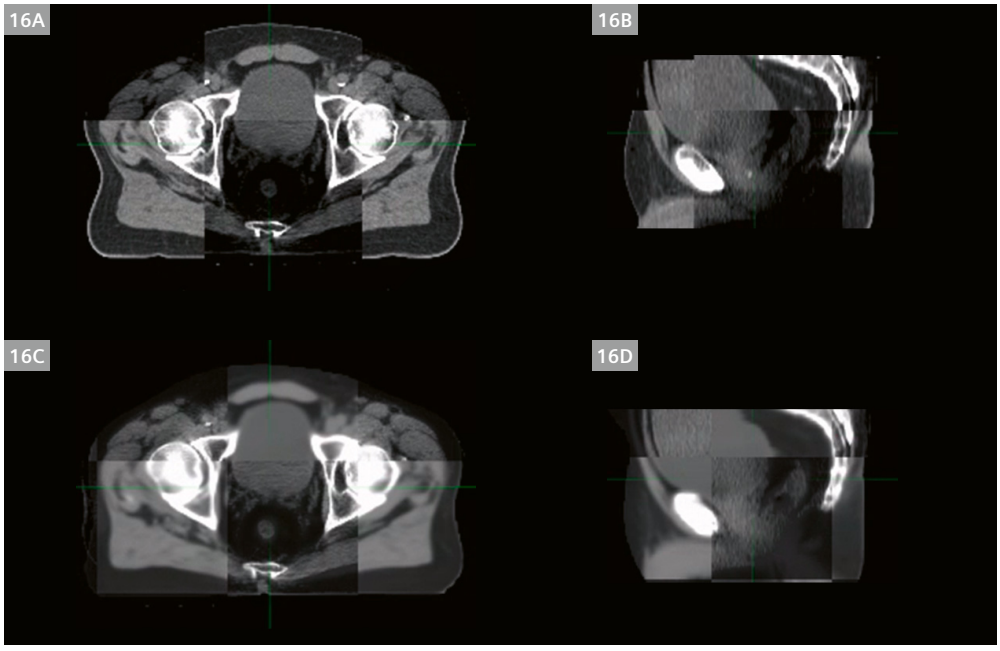

16 Localization accuracy comparison using the original planning CT data to CBCT registration as the reference **(16A, 16B)**, versus CBCT registration to the MR-based Synthetic CT **(16C, 16D)**.

2. Evaluation of the brain MR-based Synthetic CT from Universitätsklinikum Erlangen, Germany

A total of five brain cancer patients underwent MRI (MAGNETOM Sola 1.5T) and CT (SOMATOM go.Open Pro) simulation with a maximal time delay of five days. Both simulation images were acquired in a dedicated RT setup to minimize differences in the head position between MRI, CT, and RT treatment.

The five patients were scheduled for subsequent EBRT. All patients were treated with 6 MV X-rays using a VMAT (RapidArc) treatment technique with different dose prescriptions. A clinical treatment plan according to institutional clinical guidelines was optimized on the planning CT. The thermoplastic mask structure was removed on the planning CT image to obtain the same body contour as in Synthetic CT. The same plan was recalculated on the Synthetic CT. The mean doses of the target volumes (PTV, GTV) and OARS (brainstem, chiasma, optical nerves) were compared. In all the regions of interest, the mean dose differences were below 1% (normalized to the total planned dose).

The mean dose difference for PTV and GTV were overall below 1%, with a median of 0.06%. For the brainstem and chiasma, the mean dose difference was overall below 0.52% and 1.37% respectively.

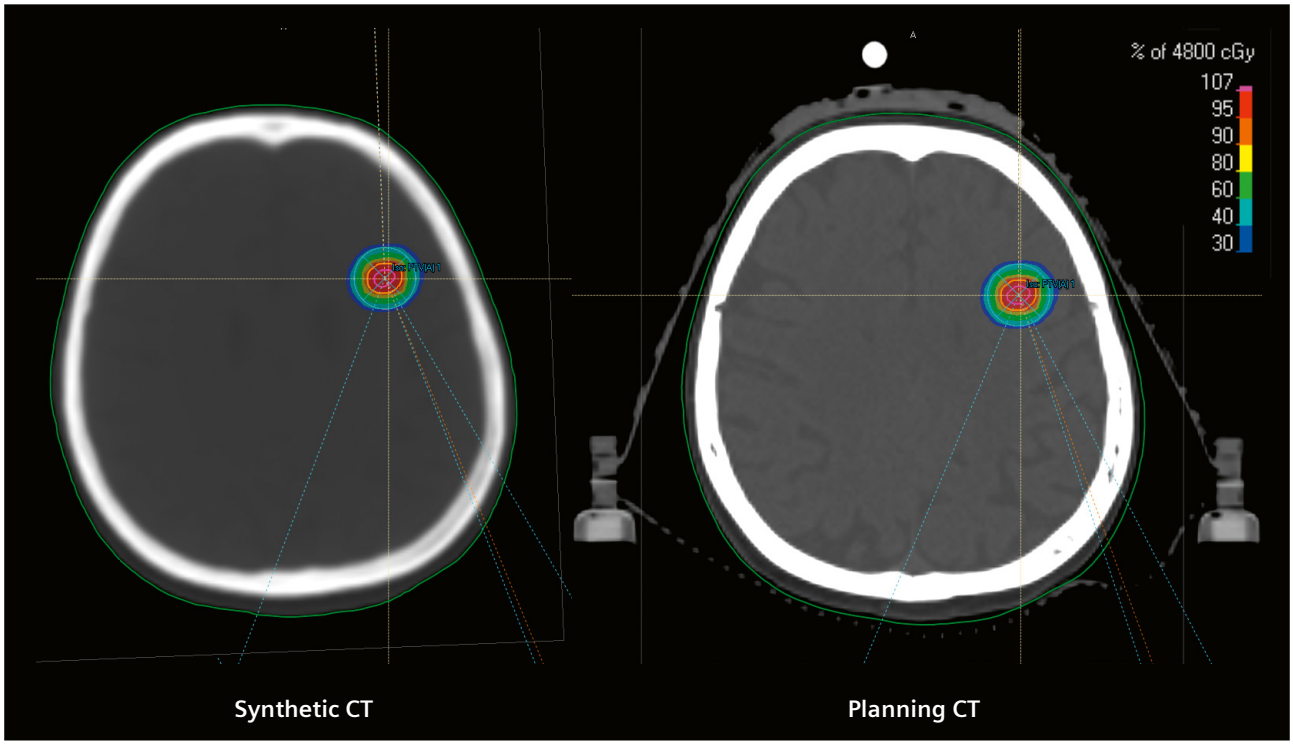

17 Dose distribution on Synthetic CT and CT with corresponding DVHs.

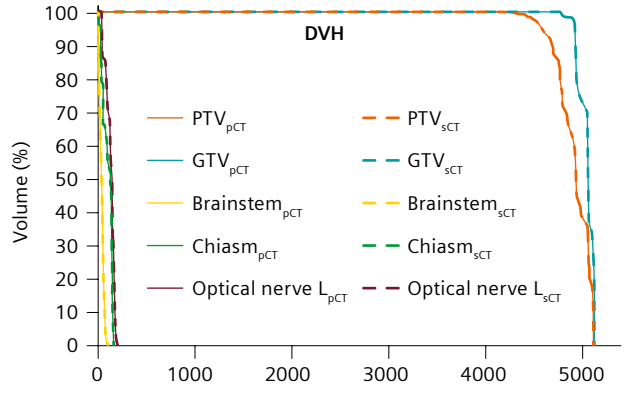

Mean dose [cGy] in ROI	on CT	on sCT
PTV	4919	4914
GTV	5045	5038
Brainstem	34	34
Chiasma	100	100
OPT_NRV_L	125	124
OPT_NRV_R	19	19

18 Mean dose on the planning CT and Synthetic CT (sCT) in six regions of interest for one patient.

Patient	Prescription dose	PTV	GTV	Brainstem	Chiasma
P1	12fx × 4 Gy	- 0.10	-0.14	0	0
P2	25fx × 2 Gy	0.08	0.08	0.17	0.42
P3	28fx × 1.8 Gy	0.83	0.85	0	1.37
P4	12fx × 4 Gy	- 0.04	-0.04	0.52	0.46
P5 (Plan 1)	1fx × 18 Gy	0.04	0.04	0	0
P5 (Plan 2)	1fx × 20 Gy	0.55	0.49	0	0
Median		0.06	0.06	0	0.21
95th percent		0.75	0.74	0.41	1.10
Max.		0.83	0.85	0.52	1.37

Table 5: Differences in dose distributions of planning CT and Synthetic CT in the PTV, GTV, and two organs at risk structures, the brainstem and chiasma, for the different patients. P5 has received two plans for two different target volumes.

Conclusion of clinical Synthetic CT evaluation

In pelvis and brain, dosimetric errors were small and on average < 1% for target structures. Automated matching localization errors for pelvis were small and, on average, ~ 1 mm along each axis. For brain, they were not evaluated.

A potential limitation is that fiducials (and some calcifications) are generally converted to soft tissue, which precludes the ability to localize by fiducial when preferred or necessary. In the special case of prostate SBRT, for example, it would be desirable to have a fiducial-based localization methodology implemented.

However, a method to contour the fiducials and override the HUs in the Synthetic CT is available in the *syngo*.via RT Image Suite. This method was not evaluated in this clinical study.

In conclusion, the MR-based Synthetic CT solution provided a clinically appropriate level of dosimetric and spatial accuracy for standard fractionation cases. Overall, the Synthetic CT created by *syngo*.via RT Image Suite VB601 provides a clinically reasonable alternative to a CT simulation exam and may be used clinically in the treatment planning and treatment of prostate pelvic standard fractionation radiation therapy as well as for brain treatment planning.

Clinical partners

Prof. Atchar Sudhyadhom, Ph.D. (Brigham and Women's Hospital, Boston, MA, USA); Siti Masitho, Ph.D. (Universitätsklinikum Erlangen, Germany); Prof. Christoph Bert, Ph.D. (Universitätsklinikum Erlangen, Germany); Florian Putz, Ph.D. (Universitätsklinikum Erlangen, Germany)

Software requirement	*syngo*.via RT Image Suite VB60; Deep learning-based Synthetic CT algorithm license
MRI scanner requirement and field strength	Training and testing were performed on a wide range of Siemens Healthineers 1.5T and 3T MAGNETOM MRI scanners: MAGNETOM Aera, MAGNETOM Skyra, MAGNETOM Sola, MAGNETOM Vida, MAGNETOM Sola Fit. The data acquisition protocols for Synthetic CT are available with *syngo* MR XA11A and later software versions for MAGNETOM RT Pro edition for MAGNETOM Vida and MAGNETOM Sola, with *syngo* XA30 and later software versions for MAGNETOM Aera and MAGNETOM Skyra.
In-plane resolution	1 × 1 mm brain; 2 × 2 mm pelvis
Slice thickness	Slice thickness is controlled by the input slice thickness, determined by the acquired input T1 VIBE-Dixon sequence.
Geometric distortion	The 3D distortion is automatically selected for the sequences in the RT Dot Engine.
Algorithm training	• Trained with a fixed number of datasets during product development and locked at the time of release. The algorithm does not learn continuously in the field. • Updates do not take place automatically. • Training and validation images were randomly assigned from the data pool. • Brain: 6486 training image sets (CT + MR) and 553 validation sets • Pelvis: 9059 training image sets and 695 validation sets • Data augmentation of the original data has been performed.
MR-based Synthetic CT generation	The acquisition time at the scanner is limited to only one sequence: T1 VIBE Dixon. Acquisition times may vary between 1 min 33 s and 4 min 12 s depending on field strength, clinical site, and acceleration modes.

Table 6: Practical information

References

1 R. W. Brown, Y.-C. N. Cheng, E. M. Haacke, M. R. Thompson, and R. Venkatesan, "Magnetic resonance imaging: physical principles and sequence design", John Wiley & Sons, 2014.
2 R. Speight et al., "IPEM Topical Report: An international IPEM survey of MRI use for external beam radiotherapy treatment planning", Phys. Med. Biol., vol. 66, no. 7, 2021.
3 G. P. Liney et al., "Quantitative evaluation of diffusion-weighted imaging techniques for the purposes of radiotherapy planning in the prostate", Br. J. Radiol., vol. 88, no. 1049, pp. 1–6, 2015.
4 W. D. Foltz et al., "Readout-segmented echo-planar diffusion-weighted imaging improves geometric performance for image-guided radiation therapy of pelvic tumors", Radiother. Oncol., vol. 117, no. 3, pp. 525–531, 2015.
5 D. Thorwarth, M. Notohamiprodjo, D. Zips, and A.-C. Müller, "Personalized precision radiotherapy by integration of multi-parametric functional and biological imaging in prostate cancer: a feasibility study", Z. Med. Phys., vol. 27, no. 1, pp. 21–30, 2017.
6 C. Dinis Fernandes et al., "Quantitative 3T multiparametric MRI of benign and malignant prostatic tissue in patients with and without local recurrent prostate cancer after external-beam radiation therapy", J. Magn. Reson. Imaging, vol. 50, no. 1, pp. 269–278, 2019.
7 M. A. Speight, Richard Dubec, Michael Eccles, Cynthia L George, Ben Henry, Ann Herbert, Trina Johnstone, Robert I Liney, Gary P McCallum, Hazel Schmidt, IPEM topical report: guidance on the use of MRI for external beam radiotherapy treatment planning. Physics in Medicine and Biology, 2021.
8 K. K. Brock, "Adaptive Radiotherapy: Moving Into the Future", Semin. Radiat. Oncol., vol. 29, no. 3, pp. 181–184, 2019.
9 K. Latifi, J. Caudell, G. Zhang, D. Hunt, E. G. Moros, and V. Feygelman, "Practical quantification of image registration accuracy following the AAPM TG-132 report framework", J. Appl. Clin. Med. Phys., vol. 19, no. 4, pp. 125–133, 2018.
10 QA cookbook: Commissioning and Quality Assurance (QA) for MAGNETOM systems in radiation therapy, siemens-healthineers.com/magnetom-world-rt 2021 HOOD05162003187576
11 C. Tsien, Y. Cao, and T. Chenevert, "Clinical Applications for Diffusion Magnetic Resonance Imaging in Radiotherapy", Seminars in Radiation Oncology, 24(3), 218–226, 2014.
12 M. A. Schmidt and G. S. Payne, "Europe PMC Funders Group Radiotherapy Planning using MRI", Phys. Med. Biol., vol. 60, no. 22, pp. R323–R361, 2015.
13 E. Paradis, C. Yue, T. S. Lawrence, C. Tsien, K. Vineberg, and J. M. Balter, "Assessing the dosimetric accuracy of MR-generated synthetic CT images for focal brain VMAT radiotherapy Eric", Int J Radiat Oncol Biol Phys, vol. 93, no. 5, pp. 1154–1161, 2015.
14 E. S. Paulson et al., "Consensus opinion on MRI simulation for external beam radiation treatment planning", Radiother. Oncol., vol. 121, no. 2, pp. 187–192, 2016.
15 E. Johnstone et al., "Systematic Review of Synthetic Computed Tomography Generation Methodologies for Use in Magnetic Resonance Imaging–Only Radiation Therapy", Int. J. Radiat. Oncol. Biol. Phys., vol. 100, no. 1, pp. 199–217, 2018.
16 L. Vandewinckele et al., "Overview of artificial intelligence-based applications in radiotherapy: Recommendations for implementation and quality assurance", Radiother. Oncol., 2020.
17 C. K. Glide Hurst et al., "Task Group 284 Report: Magnetic Resonance Imaging Simulation in Radiotherapy: Considerations for Clinical Implementation, Optimization, and Quality Assurance", Med. Phys., 2021.
18 J. M. Edmund and T. Nyholm, "A review of substitute CT generation for MRI-only radiation therapy", Radiat. Oncol., vol. 12, no. 1, pp. 1–15, 2017.
19 D. A. Low et al., "A technique for the quantitative evaluation of dose distributions", Med Phys May; 25(5): 565-61, 1998.

Contact

Michaela Hösl, Ph.D.
Global Product Marketing Manager
Cancer Therapy
Siemens Healthineers VAR CTH M&S PMK
91294 Forchheim, Germany
michaela.hoesl@siemens-healthineers.com

Learn more about Men's Health and Screening

Lectures and presentations given at the MAGNETOM World Summit are available on demand

Selecting the Right Patients in the Age of MRI Prostate Cancer Screening
Masoom Haider (Toronto General Hospital, Toronto, Canada)

Productivity and Short Examination Protocols with GO Prostate and the Prostate Dot Engine
Mukesh G. Harisinghani (Massachusetts General Hospital, Boston, MA, USA)

Prostate AI – Performance in Clinical Practice
Moon-Hyung Choi (Eunpyeong St. Mary's Hospital, Seoul, South Korea)

Active Surveilance with MRI
Kartik Jhaveri (University Health Network, Toronto, Canada)

Efficient, Fast and Precise MR-guided Biopsies with the Soteria RMC
Anshuman Panda (Mayo Clinic, Phoenix, AZ, USA)

New Minimal-invasive, Image-guided Treatment Options for Low-grade Prostate Cancer
Jurgen Fütterer (Radboud UMC, Nijmegen, The Netherlands)

Managment of Advanced Disease
Chen Min (Beijing Hospital, The National Center of Gerontology, China)

Unmet Needs in Prostate MRI. Where is the Field Heading to?
Anwar R. Padhani (Mount Vernon Cancer Centre, London, UK)

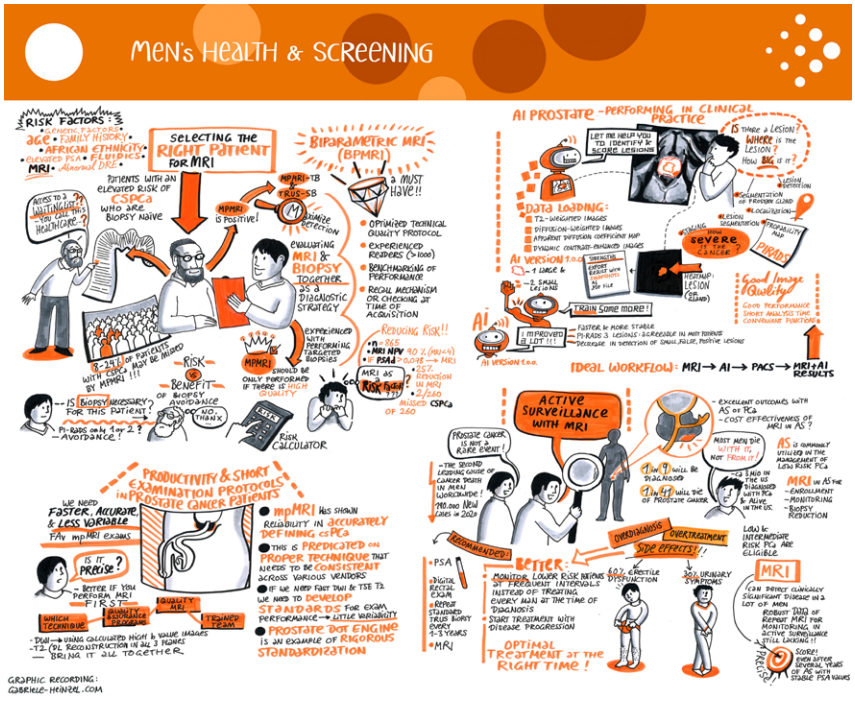

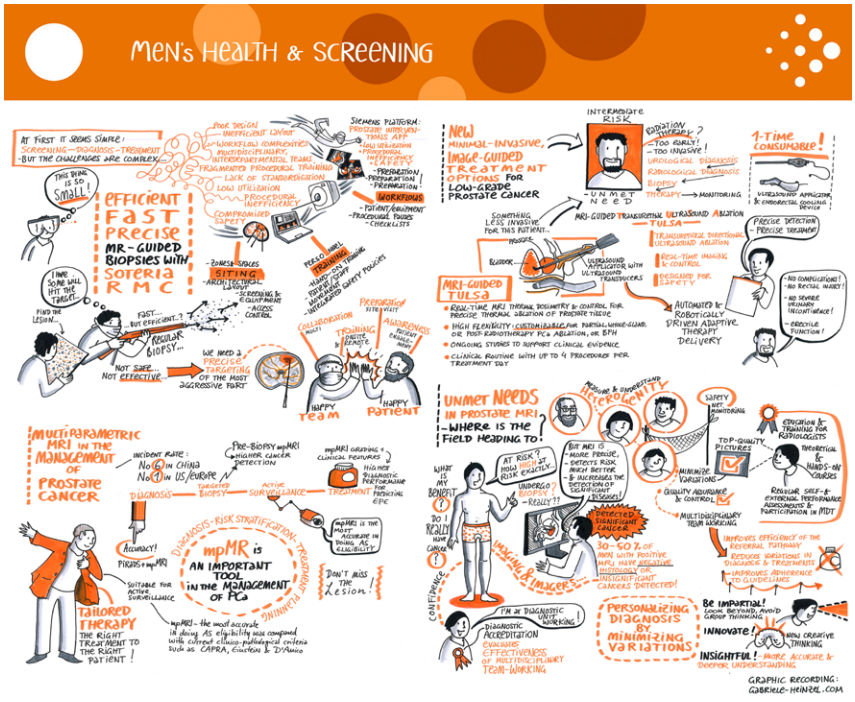

Graphic recording:
www.gabriele-heinzel.com

Don't miss this valuable source of information

https://www.magnetomworld.siemens-healthineers.com/magnetom-world-summit/recordings/mens-health

Clinical Implementation of MR-guided Radiotherapy for Prostate Cancer in Halcyon-System

Zimmermann M.[1]; Lange A.[2]; Sabatino M.[1]; Giro C.[1]; Lorenzen J.[3]; Struck J.[3]; Dahle J.[1]; Würschmidt F.[1]; Kretschmer M.[1]

[1]Radiologische Allianz, Strahlentherapie, Hamburg, Germany
[2]Beuth Hochschule für Technik, Berlin, Germany
[3]Radiologische Allianz, Diagnostische Radiologie, Hamburg, Germany

Introduction

In Germany, prostate cancer is the most common cancer among men. Approximately 58,000 men are diagnosed with prostate cancer each year, and more than 14,000 men die from it [1]. Almost half of all patients receive external beam radiotherapy (EBRT). Before treatment, a three-dimensional radiation therapy plan is created. Many clinics use thin-slice CT images to define the clinical target volume (CTV). Because of the limited soft tissue contrast of CT images, and the uncertainties in the treatment planning process, a large margin is needed to create the planning target volume (PTV). Early studies have shown that co-registered CT/MRI images improve target volume definition for radiotherapy planning of prostate cancer [2]. However, the image registration introduces an additional error in delineating targets and organs at risk (OARs) due to the modified geometry by two different examinations at two different time points.

A workflow based only on MR images (MR-only workflow)[1] offers considerably improved soft tissue contrast for CTV definition and improved OAR delineation without

Case	Age [years]	Weight [kg]	Gleason score	iPSA [ng/ml]	TNM
1	76	92	3 + 3 = 6	10.25	cT2a cN0 M0
2	78	85	5 + 4 = 9	6.50	cT2a cN0 cM0
3	78	84	3 + 3 = 6	32.80	pT3b pN0 (0/18) R1 Pn1 cM0
4	82	95	4 + 5 = 9	88.61	cT2b-c cN0 cM0
5	58	–	4 + 4 = 8	5.70	cT2c cN0 cM0
6	79	82	4 + 5 = 9	12.70	cT2c cN0 cM0
7	75	87	4 + 3 = 7	9.53	cT2c cN0 cM0
8	77	86	3 + 3 = 6	7.80	cT2b cN0 cM0
9	80	72	4 + 3 = 7	42.00	cT2c cN0 M1
10	68	83	3 + 4 = 7	9.45	pT1b pN0 cM0
11	72	84	5 + 4 = 9	11.00	cT2c cN0 cM0 Pn1
12	67	80	3 + 4 = 7	–	cT1c
13	71	72	3 + 4 = 7	101.00	pT3a pN0 (0/6) cM0 L0 V0 pM1 R1
14	74	85	4 + 5 = 9	6.58	cT2 cN0 cM0 pn1, G3
15	67	115	4 + 3 = 7	8.00	pT3b pN0 (0/5) L0 V0 Pn1 R1

Table 1: Clinical profile and tumor stages of the patients included in the implementation phase. Patients 6, 11, and 14 received radiation therapy to their lymph nodes.

registration errors. The acquisition and maintenance price is higher than that of CT imaging, but it can be considerably reduced by shared-use models including diagnostic radiology departments, so diagnostic images and MR-only sequences can be acquired in one session.

Optimizing the dose distribution requires electron density (or mass density), which is not provided by MR images. Moreover, modern image-guided radiotherapy (IGRT) linear accelerators need CT images as a reference to compare cone beam CT (CBCT) images with planning CT images for patient position correction before each treatment session. For these reasons synthetic CTs (sCT) have been introduced into clinical routine. Tissue classification methods as well as atlas-based and machine learning algorithms are used to generate sCT datasets from MR sequences. These algorithms have moved in recent years from research to the clinical world (so far for brain and pelvis cases). Commercially available solutions use somewhat different methods to generate the sCT images, and come with different business models. Spectronic offers a cloud-based pay-per-use approach, whereas Siemens Healthineers offers a classic software license model.

The main objective of our analysis was clinical implementation of the MR-only workflow in a novel ring-gantry linear accelerator system (Halcyon; Varian, Palo Alto, CA, USA) with daily CBCT based IGRT. We discuss in particular how daily CBCT guided IGRT based on sCT images compares with the traditional approach using a planning CT (pCT) image as reference. Detailed dose calculations are part of the comparison and complete the discussion.

Materials and methods

The implementation phase of MR-only radiotherapy took place from May to August 2019. It included all prostate patients without contraindications (such as pacemakers, extensive endoprosthesis, claustrophobia). During the consent discussion, patients were required to follow an empty rectum protocol before each imaging and treatment session. For radiotherapy planning, patients received first a planning CT scan with virtual simulation, and immediately afterwards (within a maximum of 30 minutes) an MRI scan in identical position.

1. Patient collective

In total 15 patients with different tumor stages were included in this study: 11 patients with localized tumors (T1–2, N0, M0), three patients with locally advanced tumors (T3a–T3b, N0, M0) and one patient with metastasis to the sacrum. Twelve of the patients included in this study received radiotherapy as primary therapy, and the other three received postoperative radiotherapy. Because of their PSA values and Gleason scores, three of the patients also had radiation therapy to their lymph nodes (Table 1).

2. CT/MRT virtual simulation

For pCT imaging, the SOMATOM Definition AS (Siemens Healthcare, Forchheim, Germany) with a slice thickness of 2 mm, 120 kV and iterative image reconstruction was used.

As MRI simulator, the 1.5T MAGNETOM Aera (Siemens Healthcare, Erlangen, Germany) installed in our clinic. Images are reconstructed with 2.5 mm slice thickness was used. Table 2 shows the acquired sequences.

For simulation purposes, patients must be scanned in the same position as on the treatment couch of the linear accelerator. So in the MRI scanner patients were positioned on a flat tabletop overlay using a knee immobilization device, reproducing the positioning setup during pCT imaging and during the treatment with the Halcyon system.

Figure 1 shows the body coil (Body 18 long MR coil 1.5T) fixed in place with a coil positioning aid (INSIGHT Body Coil Holder; Qfix, Avondale, PA, USA).

In addition to the diagnostic images (sequences listed in Table 2), the T1- and T2-sequences, together with the generated sCT are imported into the oncology information system (OIS) ARIA (Varian, Palo Alto, CA, USA). Contouring of the target volumes is performed on the images obtained from these sequences, using the diagnostic findings recorded in ARIA as support. The workflow is integrated into the ARIA CarePath.

Step	Sequence	Time in min
Orientation	localizer bh	00:17
	localizer @center	00:17
Overview	t2 tse sag 3.5 mm	04:30
	t2 haste cor mbh	00:49
Diffusion	ep2d diff b50 800 1400 tra 3 mm	04:36
sCT Spectronic	t2 tse tra p2 2.5 mm	13:35
sCT Siemens	t1 sCTp1-Dixon	02:32
Perfusion with KM	t1 vibe tra dyn 4 mm	02:05
	t1 fl2d fs tra mbh	01:20
Total		**30:17**

Table 2: Description of sequences used.

[1]*MR protocols for Synthetic CT generation are works in progress for MAGNETOM Aera, they are currently under development and not for sale in the U.S. and in other countries. Their future availability cannot be ensured. MR protocols for Synthetic CT generation for 1.5T MAGNETOM Sola and 3T MAGNETOM Vida are clinically released.*

3. Generation of sCT

3.1 Pay-per-use model (Spectronic)

Spectronic (Helsingborg, Sweden) uses an atlas-based algorithm for sCT image generation, offered as a cloud-based service[2]. Anonymized MRI datasets are transferred from PACS or directly from the MRI scanner to the cloud using a DICOM-receiver installed at the clinic network. After being de-anonymized in the DICOM-receiver the generated sCTs are transferred to PACS. Customers are informed by E-mail that new data are available. The sCT images are generated using a statistical decomposition algorithm (SDA) [3]. The atlas-based method is combined with machine learning. The algorithm calculates the most probable CT representation for an MRI image set, according to previously acquired datasets. So it is important always to follow the same protocol and use the same scan parameters when scanning patients, to obtain the same contrast as in the training datasets.

3.2 License-based model (Siemens Healthineers)

Siemens Healthineers combines a tissue classification and an atlas-based method to generate the sCT image. From the required T1 VIBE Dixon sequence, four MR datasets with different weighting in water, fat, in-phase and opposed-phase were obtained. The four sets or image sets are used by the *syngo*.via RT Image Suite to generate an sCT dataset in a few minutes (Fig. 2). Bones are rendered in the sCT image set using a multi atlas-based algorithm, so the three lowest lumbar vertebrae must be scanned during the sequence acquisition.

4. Treatment planning

A VMAT treatment plan was optimized using a Halcyon system (V2.0) with 6 MV flattening filter-free beam and Eclipse V15.6. Later, the sCT image and pCT image are registered rigidly and the structures and beam configurations are transferred to the sCT image. On the sCT image, the treatment plan is re-calculated, without new optimization.

5. Treatment and image guided radiotherapy

5.1 Halcyon with iCBCT (online matching)

For IGRT, the Halcyon linear accelerator uses daily CBCT with iterative image reconstruction (iCBCT) and slice thickness of 2 mm. A treatment session without imaging before dose application is not possible with this system.

1 Patient positioning in an MRI device using MRI compatible positioning aids: flat table top with knee immobilization device to reproduce the patient positioning from the simulation to the treatment, in this case using the Halcyon.

[2]The information shown herein refers to products of a 3rd party, which are their regulatory responsibility. Please contact the 3rd party for further information.

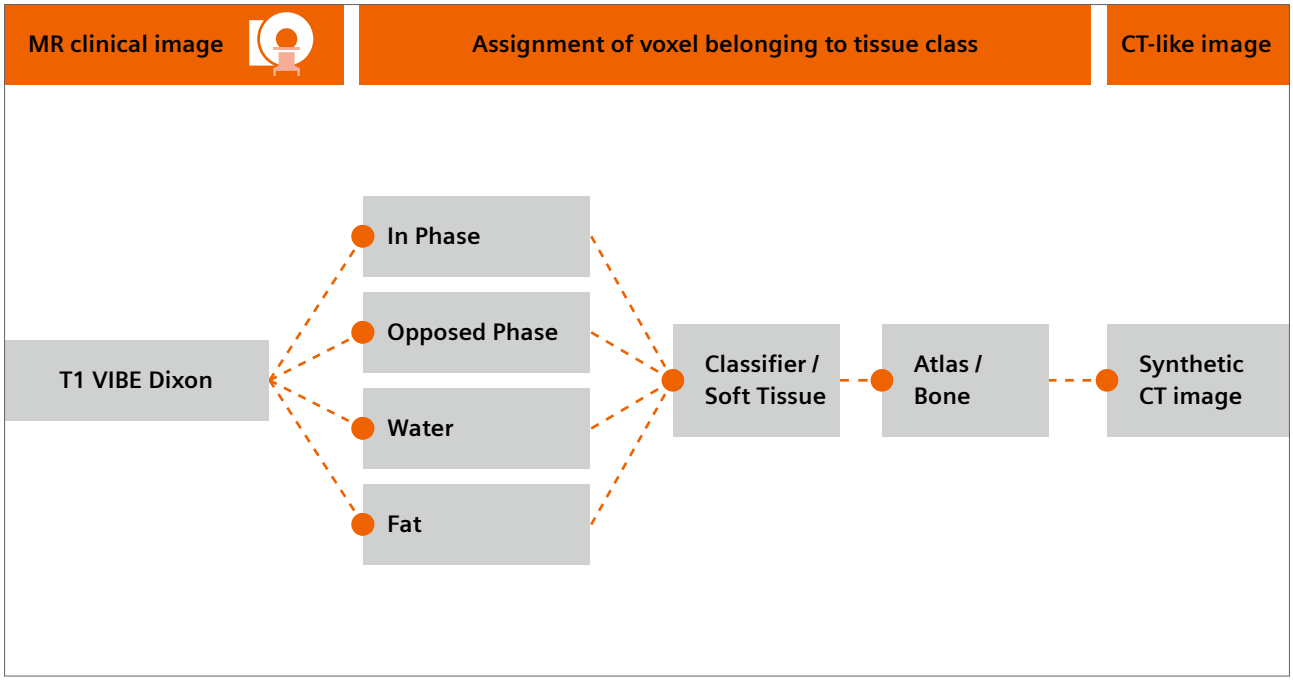

2 The synthetic CT algorithm for the pelvis, from image acquisition to synthetic CT image generation.

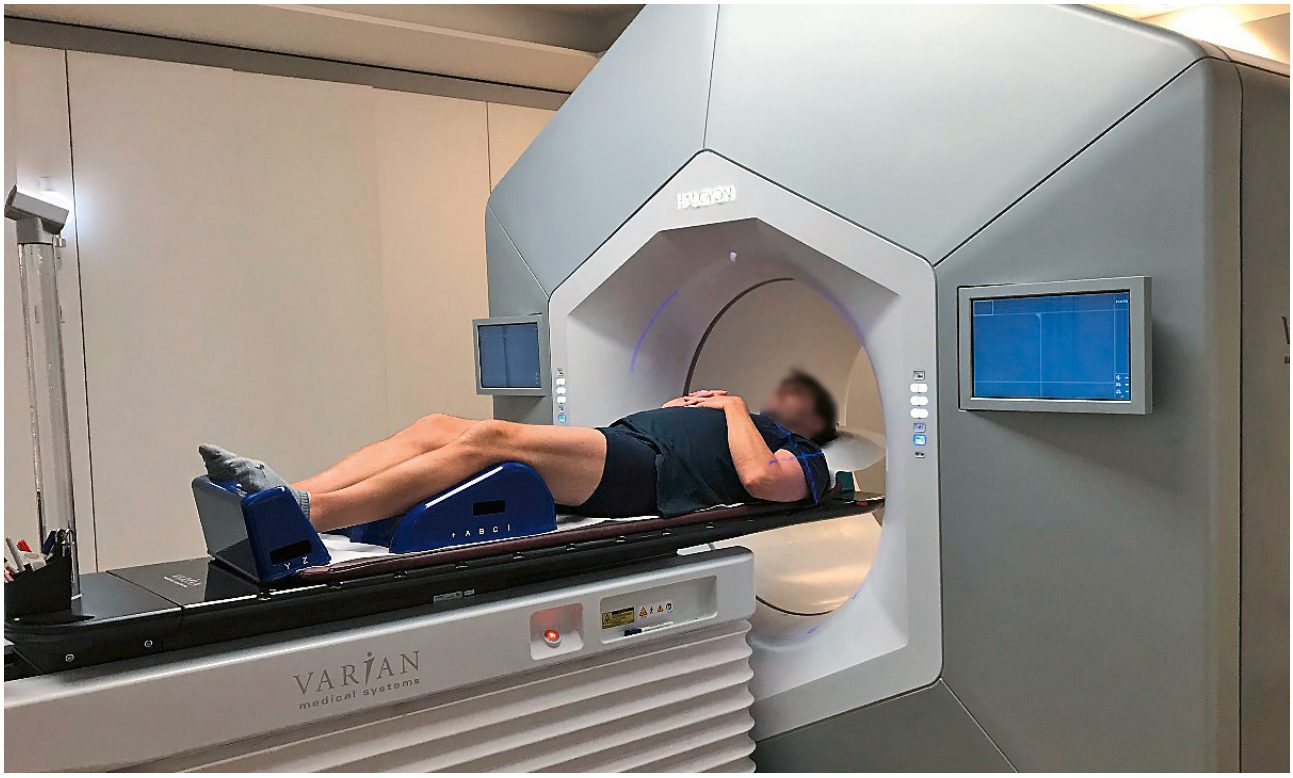

3 Patient positioning on the Halcyon.

5.2 Offline matching

In the implementation phase, each CBCT image is registered offline with the pCT and sCT images (Siemens and Spectronic). Registration is based on intensity differences and a pixel-based similarity optimization. For this auto-registration, a region including the PTV and a margin of 2 cm was selected (Fig. 4). To calculate translations in x-, y- and z-directions, the following equation was used:

$$\Delta\vec{V} = \Delta\vec{V}_{CBCT/pCT} - (\Delta\vec{V}_{CBCT/sCT} + \Delta\vec{V}_{pCT/sCT})$$

where the term $\Delta\vec{V}_{pCT/sCT}$ expresses the intrinsic offset between pCT and sCT images.

In order to perform this analysis analog to the clinical work, image registration was limited to translations, so rotation, pitch, and roll were not considered.

6. Quality assurance

Currently there is no official guideline for quality assurance (QA) for MRI systems used for radiotherapy planning.
To measure geometric distortions in MRI, the GRADE Phantom (Spectronic) was used. As result of the analysis, a PDF is generated with a 3D overview of the distortion in a clinically relevant scan volume (Fig. 5).

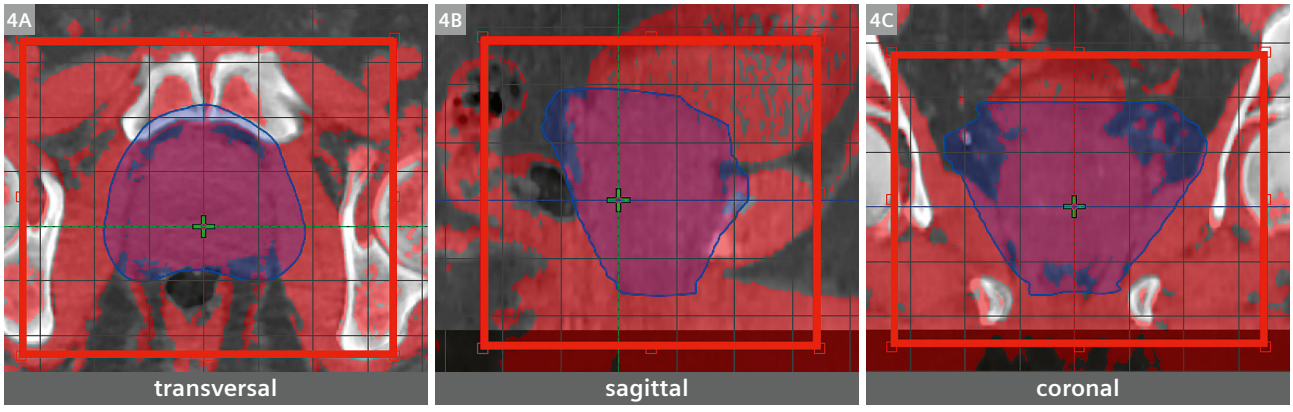

4 Example of image registration between CBCT images and CT images using soft tissue. The contoured PTV is in blue and the soft tissue used for the auto-registration algorithm is in red. The red line defines the volume of interest (VOI) used for the registration.

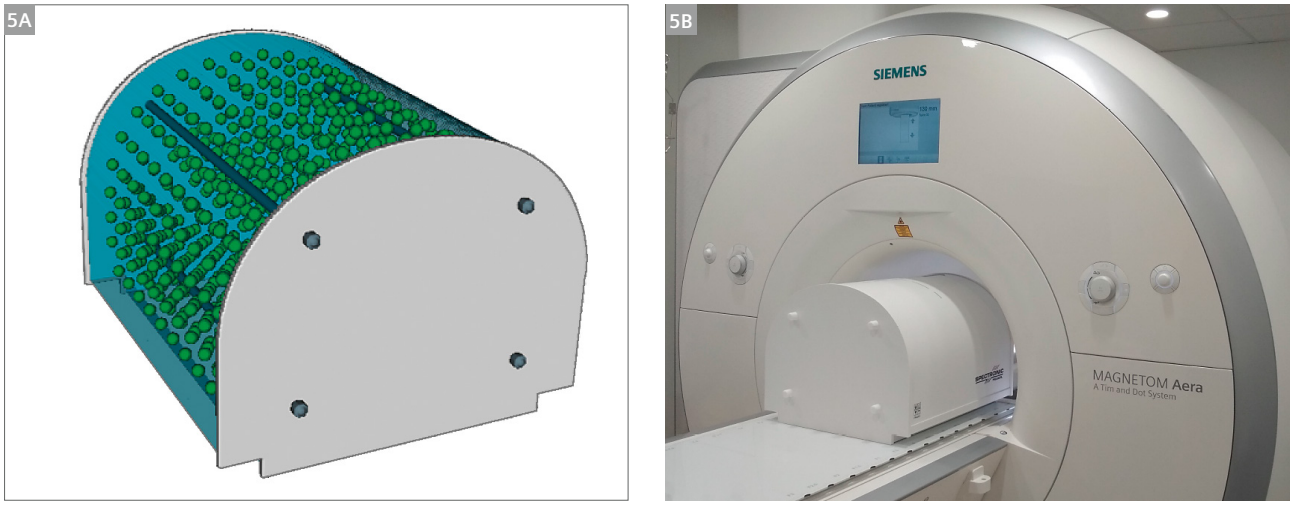

5 GRADE phantom from Spectronic, used to measure geometrical distortion. **(5A)** Image of the phantom. **(5B)** Phantom on the scanner allowing the measurement of geometric distortion in the entire scan field.

Results

Figure 6 shows an example of the results from the different sCT generation methods. The solution from Spectronic with its continuous Hounsfield units (HU) distribution is similar to a planning CT image whereas the Siemens solution uses a discrete HU distribution: Air (-1000 HU), fat (-75 HU), water (0 HU), spongy bone (204 HU) and cortical bone (1170 HU) (Fig. 6). The soft tissue of bladder, rectum and prostate is assigned 0 HU, like water. The sCT images from Spectronic use different HU values for different soft tissues, in analogy to pCT images.

Dose distributions

Different therapy concepts regarding the total dose were used during this study. For comparison reasons, the calculated plans were all normalized to the mean PTV dose and only relative dose deviations were considered.

In Figure 7, mean dose differences of the 15 patients are represented using a boxplot diagram, showing the results for the following OARs: rectum, bladder, and right- and left femoral head. The plot gives the difference between the calculated dose based on the sCT (Spectronic) and pCT (left box); and between the calculated dose based on the sCT (Siemens) and pCT (right box). The total mean difference is below 2%.

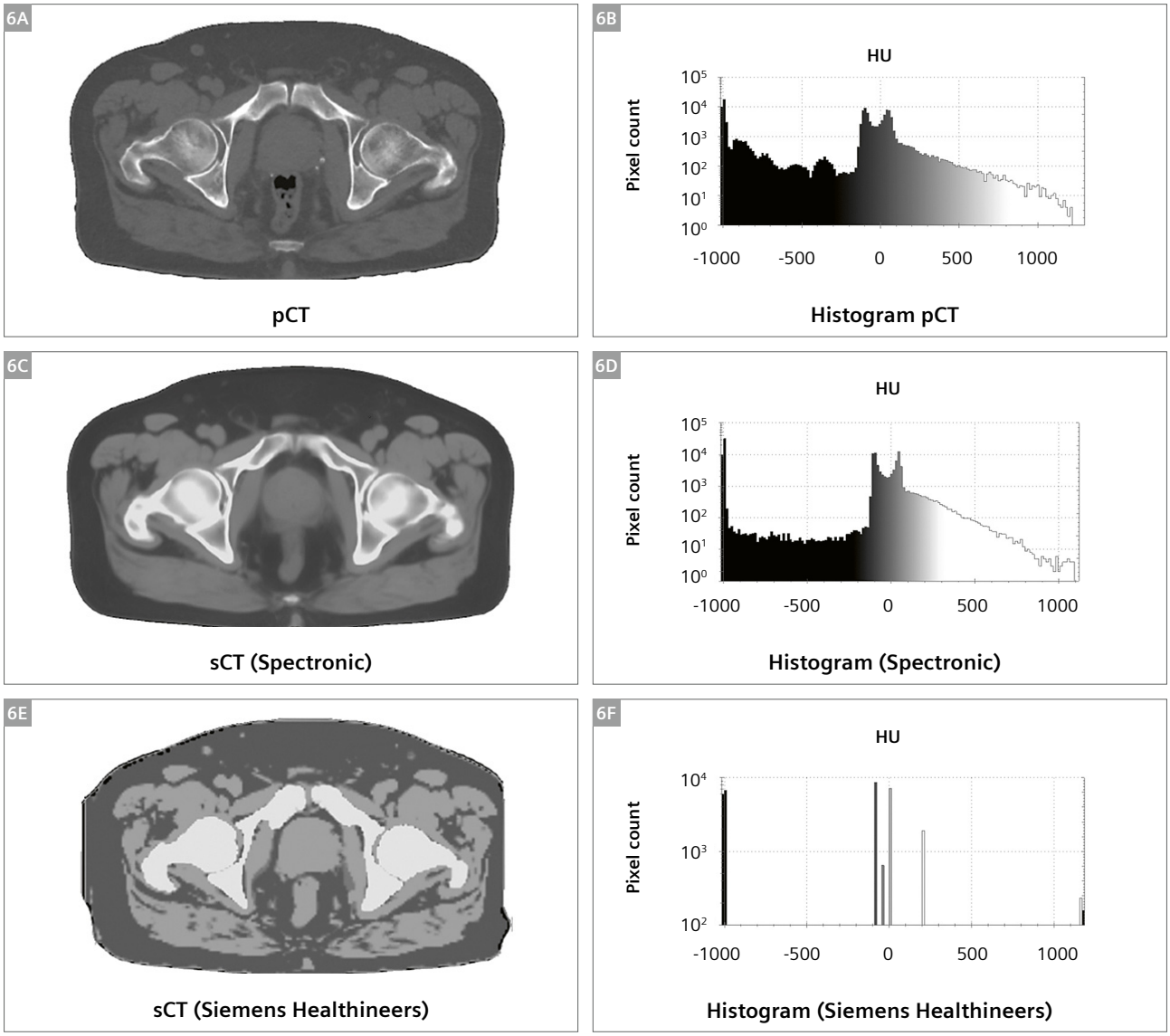

6 Examples of pCT (6A), sCT (Spectronic: 6C) and sCT (Siemens: 6E) representation including HU surface histogram (pCT: 6B; Spectronic: 6D; Siemens: 6F) of the shown cross-sectional images. The HU histograms of the pCT and the sCT (Spectronic) have a continuous spectrum from -1000 to 1210 HU and -1000 to 1071 HU, respectively. The HU histogram of the sCT (Siemens) has discrete values.

Offline matching

For both manufacturers, we evaluated translations after offline IGRT between CBCT/pCT and CBCT/sCT of 15 patients with a total of 513 CBCTs. In Figure 8, each point represents the deviation in one-dimensional direction from the registration (PTV + 2 cm, see Figure 4) between the CBCT and the respective pCT (vertical axis) and between CBCT and the respective sCT (horizontal axis). Considering all one-dimensional directions as independent parameters the correlation between sCT (Spectronic) and pCT images has a coefficient of determination of $R^2 = 0.895$. The correlation between sCT (Siemens) and pCT has a coefficient of determination of $R^2 = 0.851$. In the lateral (x) direction both sCT solutions show best correlations to CBCT compared to the CT (considered the gold standard).

For Spectronic, the worst correlation is in the z-direction whereas with the Siemens solution the lowest correlation is in the y-direction. Analyzing the registrations between CBCT and pCT images, 94% of the one-dimensional translations in the three directions are smaller than 10 mm. For registrations between sCT (Spectronic) and sCT (Siemens) respectively with CBCT images, 95% of the translations are smaller than 10 mm. The maximum difference between CBCT and pCT is 1.9 ± 5.2 mm in longitudinal direction (z), between CBCT and sCT (Spectronic) −2.5 ± 5.6 mm in vertical direction (y) and between CBCT and sCT (Siemens) 1.2 ± 5.5 mm in longitudinal direction.

The calculated translations between pCT and sCT differ significantly ($p < 0.001$) in all spatial directions, but they do not exceed 1 mm on average (Figure 9).

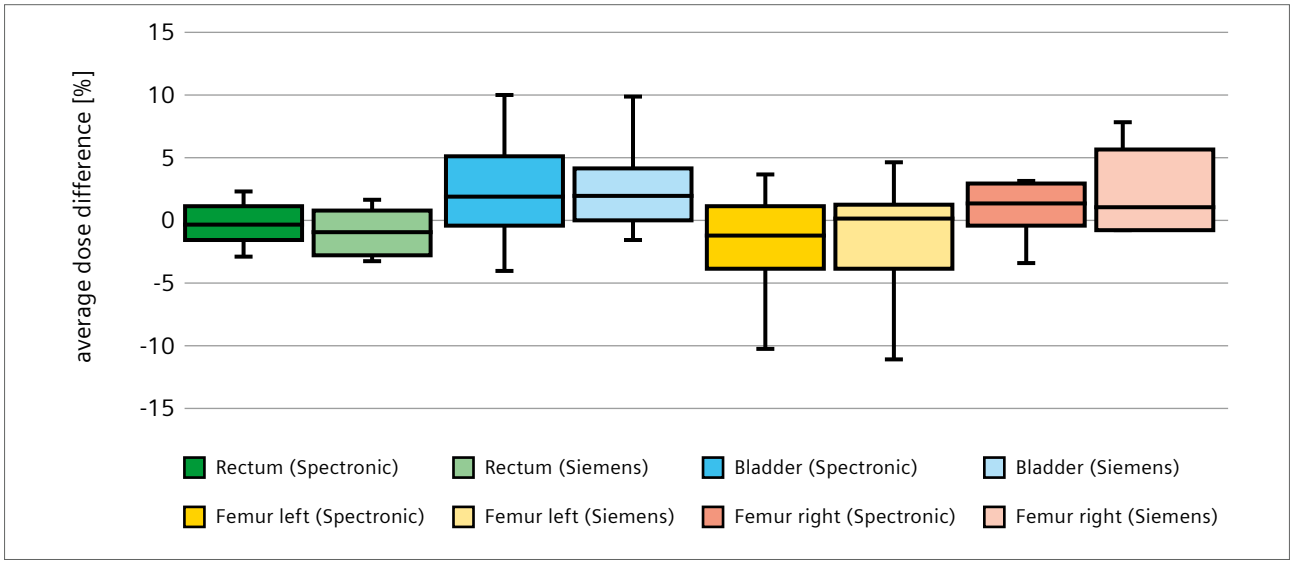

7 Boxplots of the mean dose difference of considered OARs. Representation of the dose differences to pCT, each in comparison to sCT.

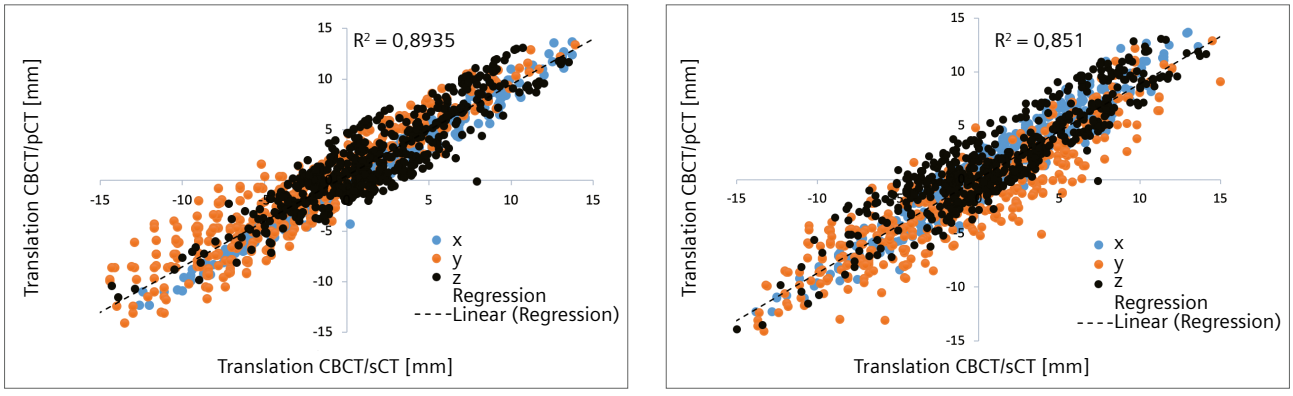

8 Scatterplot showing the translations from CBCT to pCT and from CBCT to sCT, for Spectronic (left) and Siemens (right) (n = 513 CBCTs). Estimations of the coefficient of determination considering all directions as independent values. Each direction is represented by a different color: blue = x, lateral; orange = y, vertical; black = z, longitudinal.

Discussion

In order to integrate the MR-only workflow into our clinical routine we had to develop a new CarePath (ARIA, Varian). For this, the existing workflow has been extended by adding the MRI simulation, including the sCT generation, as new task. This modified workflow comprises the pCT scan acquisition, followed by MRI acquisition when the MRI scanner was available. Afterwards, the standard clinical workflow was carried out. During the validation phase of this study, pCT images were used as basis for contouring, dose calculation, and IGRT. In the analysis, the results from sCT are compared with pCT as a reference.

The MR-only workflow eliminates the error introduced in the standard MR/CT workflow when doing image registration. Patient positioning during CT and MRI acquisition may be different. Moreover, scans are taken at different times, which can produce different internal geometry (for example bladder filling).

The standard simulation timeslot required for MR only is 45 minutes, independent of the chosen solution for sCT generation. The sequences required for sCT generation and

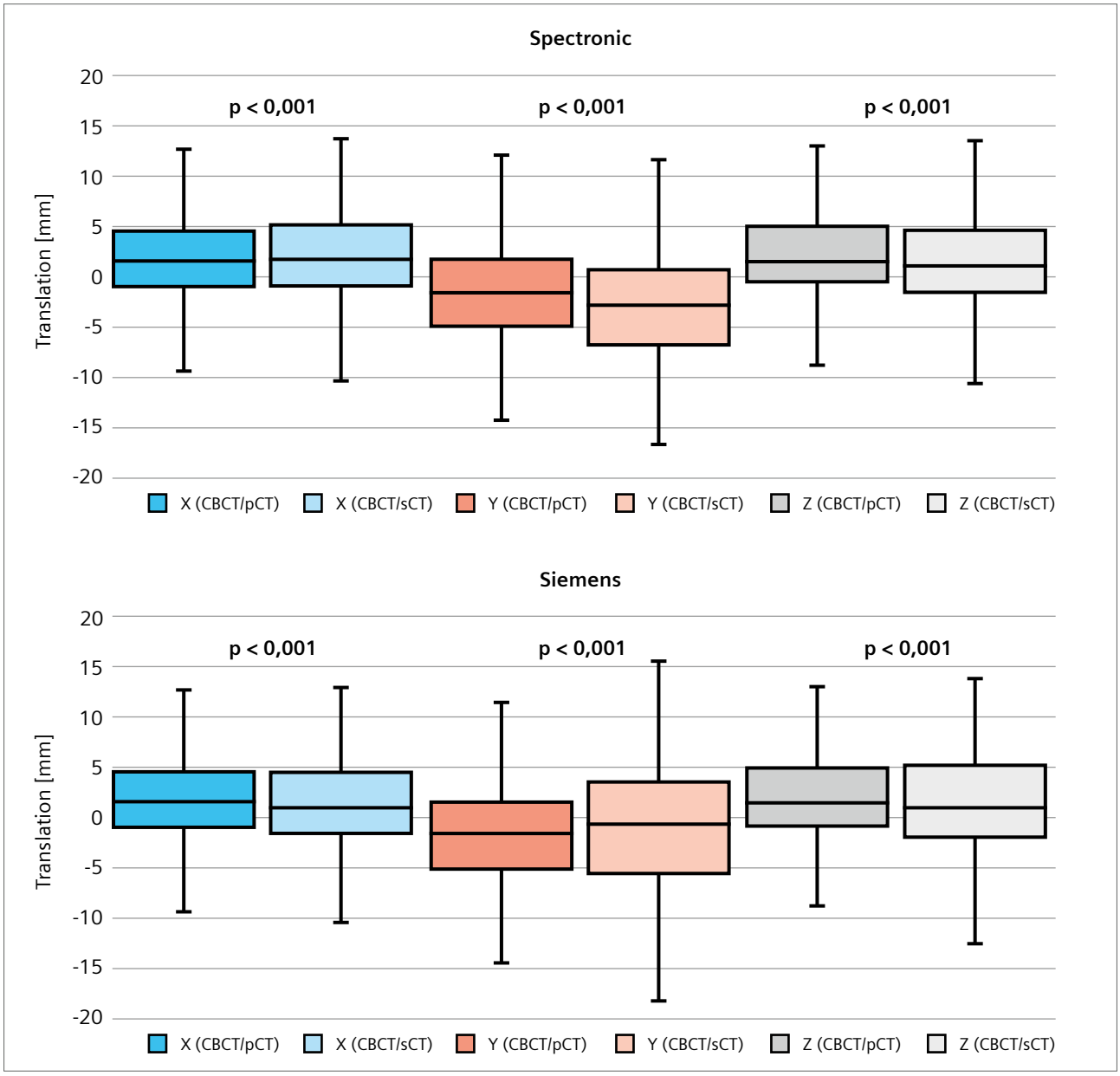

9 Boxplots of the translations of the CBCT registration to pCT, sCT (Spectronic) and sCT (Siemens). blue = x-direction, orange = y-direction, grey = z-direction.

also the diagnostic images for staging are taken at this time. If diagnostic images are already available, the timeslot is shortened to 20 minutes to acquire T2- and T1-Dixon sequences for contouring, and generate sCT images. The advantage of the quick T1-Dixon sequence from the Siemens solution is reduced when considering that a T2 sequence is normally needed for contouring. However, an important advantage of the quick acquisition is that motion artifacts are less prominent compared with those from a long sequence acquisition for sCT generation.

All 15 patients included in the implementation phase received a daily image-guided radiotherapy treatment in the prostate region at the Halcyon linear accelerator. A total of 513 CBCT images were compared with pCT and sCT images to calculate the translation. The values were significantly different when comparing the results from pCT (reference) images to the results from sCT images. The correlations (R^2 = 0.85–0.89) from CBCT/pCT and CBCT/sCT images demonstrate the difficulty when comparing the translation values from pCT and sCT images because of changes in geometry between pCT and MRI (sCT) scans taken at different times. The mean differences are smaller than 1.1 mm, and therefore not clinically relevant for daily IGRT on the Halcyon. They are, moreover, in accordance with already published studies [4].

IGRT based on sCT can therefore be performed on the Halcyon-System and allows the replacement of the conventional workflow using pCT as reference imaging for online matching. For the considered OARs the dose calculations based on sCT image sets from Siemens and

Spectronic show small mean differences and dose distributions.

The GRADE Phantom, adapted to MRI, allows to scan a large field of view, comparable to the field of view used for a pelvis patient. The mean distortion value measured in a clinically relevant field of view (150–200 mm from magnet isocenter) is 0.76 mm.

Conclusion

The MR-only workflow with the 1.5T MAGNETOM Aera has been successfully implemented. High contrast images for prostate contouring, and the immediate availability of the radiological report integrated in the ARIA OIS are helpful features that will lighten the daily workload in a busy clinical environment. The daily IGRT using the sCT image generated with the solution either from Siemens or Spectronic as reference CT can be performed on the Halcyon-system and allows the replacement of the conventional workflow using a pCT. The "pay-per-use"-model offered by Spectronic allows costs to be assigned to patients. The advantage of a license-based model as offered by Siemens is the unlimited and real-time availability of sCT.

References

1 Robert Koch Institute, Society of Epidemiological Cancer Registries in Germany, editors. Cancer in Germany for 2015/2016, 12th edition. Berlin, 2019.
2 Nyholm T, Nyberg M, Karlsson MG, Karlsson M. Systematisation of spatial uncertainties for comparison between a MR and a CT-based radiotherapy workflow for prostate treatments. Radiat Oncol. 2009; 4(1): 54. doi:10.1186/1748-717X-4-54.
3 Siversson C, Nordström F, Nilsson T, Nyholm T, Jonsson J, Gunnlaugsson A, Olsson LE. MRI only prostate radiotherapy planning using the statistical decomposition algorithm. Med. Phys. 2015; 42(10): 6090-6097. doi:10.1118/1.4931417.
4 Chen S, Quan H, Qin A, Yee S, Yan D. MR image-based synthetic CT for IMRT prostate treatment planning and CBCT image-guided localization. J Appl Clin Med Phys. 2016; 17(3): 236–245. doi:10.1120/jacmp. v17i3.6065.

Contact

Mandy Zimmermann M.Sc.
Medical Physics
Radiologische Allianz Hamburg
Mörkenstraße 47
22767 Hamburg
Germany
Tel.: +49 (40) 325552-598
mandy.zimmermann@radiologische-allianz.de

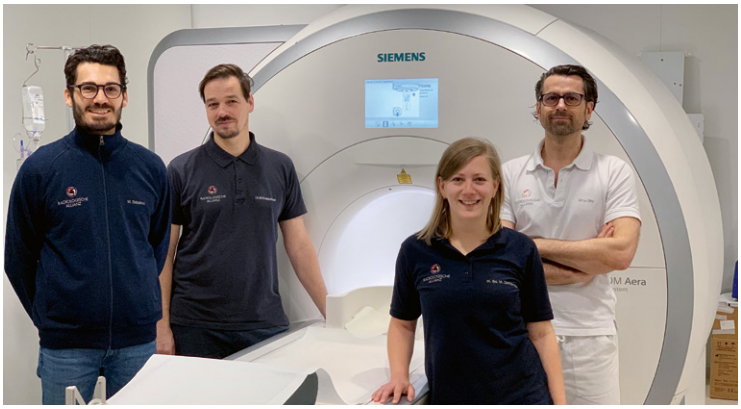

Left to right: M.Sc. Marcello Sabatino, Dr. Matthias Kretschmer, M.Sc. Mandy Zimmermann, Dr. Christian Giro

Personalized Treatment for Patients with Prostate Cancer Using MRI-guided Transurethral Ultrasound Ablation (TULSA)

Joyce Bomers, Ph.D.[1]; Cameron Wright, M.Sc.[2]; Jurgen Fütterer, M.D., Ph.D.[1]

[1]Department of Imaging, Radboud University Nijmegen Medical Centre, Nijmegen, The Netherlands
[2]Profound Medical Inc., Mississauga, Canada

Background

The lifetime risk of being diagnosed with prostate cancer (PCa) is one in six [1]. Although PCa can be lethal, most men who are diagnosed with PCa will not suffer clinically significant consequences from the disease during their lifetime. According to (inter)national guidelines, when a patient has localized PCa treatment the conventional treatment options include radical prostatectomy (RP) and radiation therapy (RT), which treat the whole prostate regardless where the underlying pathology is located. The comorbidity associated with this type of treatment in combination with a relatively high cancer specific survival (92%) has a tremendous impact on quality of life and cost. Approximately 15–20% of the patients who undergo prostatectomy will suffer from treatment-induced urinary dysfunction and 8–36% will have to live with erectile dysfunction [2, 3].

Several new interventions have been developed hoping to offer non-inferior oncological control with an improved safety profile, including minimally invasive modalities such as high-intensity focused ultrasound, cryoablation, and laser ablation [4]. At their inception these technologies performed whole-gland ablation, but as PCa screening and disease localization have improved primarily due to the advent of mpMRI [5], there has been a shift to targeted treatment. Targeted therapy treats the dominant lesion plus an additional thermal safety margin, with the rationale this should offer the best compromise between oncological control and morbidity.

The concept of targeted therapy is still relatively new and therefore controversial, and has stricter inclusion requirements, meaning patients with multi-focal and/or diffuse disease are likely not ideal candidates. This underscores the need for a modality that can delivery safely and effectively both whole-gland and targeted treatment.

MRI-guided transurethral ultrasound ablation (TULSA) has been used as a primary treatment for whole-gland treatment [6, 7] as well as targeted treatment [8, 9] and will be explored in more detail.

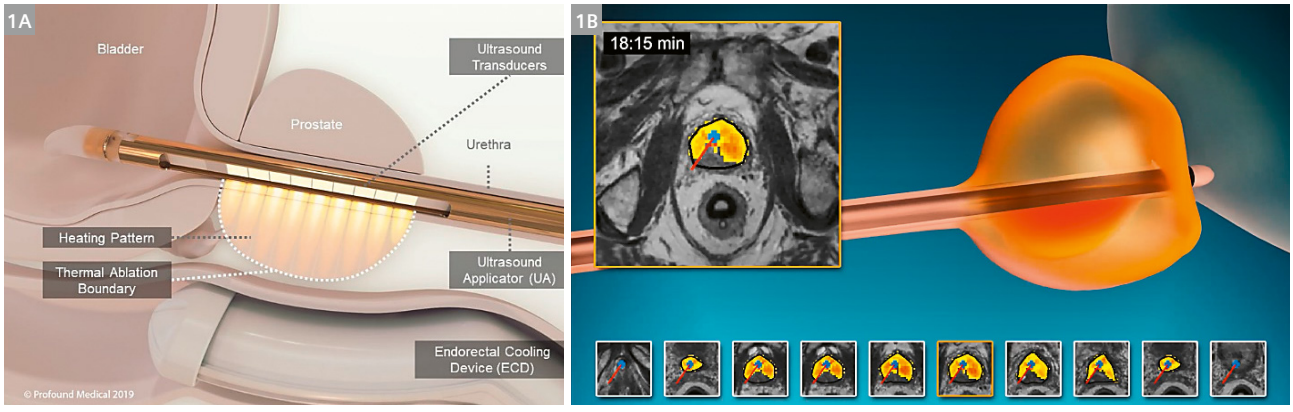

1 MRI-guided transurethral ultrasound (TULSA) procedure. **(1A)** Rendering of ultrasound applicator and endorectal cooling device. **(1B)** Ablation zone is prescribed on intraoperative transverse T2-weighted images from prostate apex to base, and the ablation is observed in real-time with thermometry.

TULSA overview

TULSA is a newer technology which uses high-intensity thermal ultrasound to destroy prostate tissue by treating the prescribed boundary to an ablative temperature of 55 °C. The procedure takes place entirely in the MRI suite with the patient under general anesthesia or regional block. A rigid transurethral ultrasound catheter is guided into the prostate and then secured with an MRI-compatible robot that provides linear and rotational motion of the device within the prostatic urethra during treatment planning and the ablation. The ultrasound catheter has ten separate elements, each which are independently controlled for acoustic power and frequency. A rectal device is inserted which cools the rectum with cold water (Fig. 1A).

Device localization is performed with a high-resolution sagittal 3D T2-weighted SPACE sequence (TR 1700 ms; TE 97 ms; Slice thickness 1 mm; FOV 256 mm; Resolution 1 x 1 x 1 mm). Treatment planning is performed with transverse T2-weighted images (qtse: TR 7500 ms; TE 101 ms; Slice thickness 3 mm; FOV 260 mm; Resolution 1 x 1 x 3 mm) and monitored in real-time with a segmented EPI MRI thermometry sequence (TR 45 ms; TE 8 ms; Slice thickness 4 mm; FOV 256 mm; Resolution 2 x 2 x 4 mm) (Fig. 1B).

One of TULSA's distinguishing features that allows it to ablate large volumes of tissue yet still offer conformal ablation is the automated controller. During the ablation real-time thermometry images acquired by the MRI are sent to the TULSA software every ~6 s. These images are processed immediately upon arrival, and the controller in turn calculates the optimal device rotation rate, acoustic power and acoustic frequency for all active ultrasound elements. This process repeats itself indefinitely until the ablation is completed. The control parameters are adjusted to achieve the fine balance of reaching the 55 °C temperature at the prescribed boundary in the shortest possible treatment time, but not overshooting into surrounding structures. Over time (~50 minutes for a whole-gland ablation) the ultrasound catheter is rotated through the prostate via the robotic arm, delivering a consistent thermal dose to the targeted volume.

Whole-gland TACT trial

The most extensive and up-to-date clinical data regarding TULSA comes from the TACT trial (NCT02766543). This was a multi-center, prospective, single-arm clinical trial where patients with low- to intermediate-risk, biopsy-proven, localized PCa (Table 1) were treated with TULSA as a first-line therapy. From September 2016 until February 2018 115 men were enrolled across 13 different institutions in 5 different countries. The main objectives of the study were safety and early oncological control at one year as determined by PSA, biopsy, and mpMRI. Every patient regardless of their specific disease characteristic received whole-gland ablation but with sparing to the urethra and apical sphincter. Repeat TULSA was not allowed. At the time of writing 2-year follow-up is available for 48 / 115 patients (42%).

Procedural outcomes

The median (IQR) ablation time was 51 minutes (39–66), achieving 98% thermal coverage. The spatial precision of the TULSA ablation was 1.4 mm. Patients were discharged the same day (55%) or admitted overnight (45%), mostly depending on the local hospital protocol.

Safety outcomes

No ≥ Grade 4 adverse events, no intraoperative complications, no rectal injury, and no rectal fistula were observed. A total of 12 Grade 3 (severe) adverse events occurred in 9 (8%) men, including genitourinary infection (4%), urethral stricture (2%), urinary retention (2%), urethral calculus and pain (1%), and urinoma (1%), all resolved by the 12-month visit.

No patient had severe erectile dysfunction. Of the 92 patients at baseline who had erections sufficient for penetration, 75% maintained this at one year, and this increased to 83% in those patients with two-year follow-up, indicating a continued recovery. Moderate urinary incontinence (Grade 2, pads) was reported by 3 patients (2.6%), with no new incontinence at 2 years. The patient-reported IPSS (International Prostate Symptom Score) questionnaire was used to quantify urinary symptoms after the intervention, where a score 1–7 represents mild, 8–19 moderate and 20–35 severe symptoms. The median IPSS was unchanged from 7 at baseline to 6 at one year and 5 at two years after TULSA.

Oncological outcomes

Median (IQR) PSA reduction at one year was 95% (91–98%) with a median nadir of 0.3 ng/ml and was stable at two years. Median decrease in perfused prostate volume changed by 91% at 12 months, decreasing from a median of 37 cc at baseline to 3 cc.

Median age, age	65 (59–69)
PSA, ng/ml	6.3 (4.6–7.9)
Grade Group Distribution, n (%)	72 with GG2 (63%) 43 with GG1 (37%)
Targeted prostate volume, cc	40 (32–50)

Table 1: Patient characteristics at baseline for whole-gland TACT trial.

From biopsy results there was no evidence of cancer in 72 (65%) men and 16 (14%) had low-volume GG1. Among the 68 men with GG ≥ 2 at baseline, 54 (79%) were free of GG ≥ 2 at 12 months. Similarly, 20 of 26 (77%) men with high-volume GG1 at baseline had either no cancer or low-volume GG1 (< 3 cores and < 50% per core) at 12 months. Overall, histological improvement (eradication of GG2, shift from high to low-volume GG1, or eradication of GG1 disease) occurred in 75–80% of men across all risk subgroups.

12-month MRI showed a 96% negative predictive value for absence of GG2 disease on 1-year biopsy.

TULSA case example: whole-gland ablation

A 68-year-old male arrived in our clinic in 2017 with suspicion of localized PCa in the left midgland peripheral zone based on elevated PSA and mpMRI findings (PSA 6.9 ng/ml, PI-RADS 5, prostate volume 52 cc). Baseline mpMRI findings were concordant with the MRI-targeted biopsy, revealing 2 positive cores with a total cancer core length of 12 mm (Grade Group 2).

The patient underwent whole-gland TULSA with urethra and apical sphincter sparing, with the treatment plan show in Figure 2A. The total ablation time lasted 42 minutes, with the patient discharged the following day. The maximum heat deposition at the end of treatment (Fig. 2B) and the corresponding immediate post-ablation contrast scan revealing immediate cell kill can be seen in Figure 2C.

One-year follow-up visit was promising, with the patient experiencing no urinary incontinence, no rectal injuries, and an IPSS improvement from 14 to 8. Oncological control at 12 months was demonstrated by a low and stable PSA of 0.41 ng/ml, negative mpMRI and a negative 12-core biopsy.

TULSA personalized care

As discussed earlier, in the last decade PCa disease localization has greatly improved. This has given treating physicians the option to spare viable prostate tissue and treat only the source of tumor. Opting for targeted therapy is not solely a clinical decision however, as the patient's wishes and underlying health conditions must also be considered, providing a better platform for the patient to control their own care. Possible treatment options with TULSA include whole-gland, whole-gland with nerve sparing, hemi-ablation, or quadrant ablation. Figure 3 illustrates a hypothetical custom treatment plan with TULSA.

If one considers the TACT trial as 'worst-case' for safety and morbidity as the ablation was performed on the whole gland without nerve sparing, it is reasonable to expect a safety improvement moving to partial ablation, although this must be still be confirmed through more extensive clinical trials.

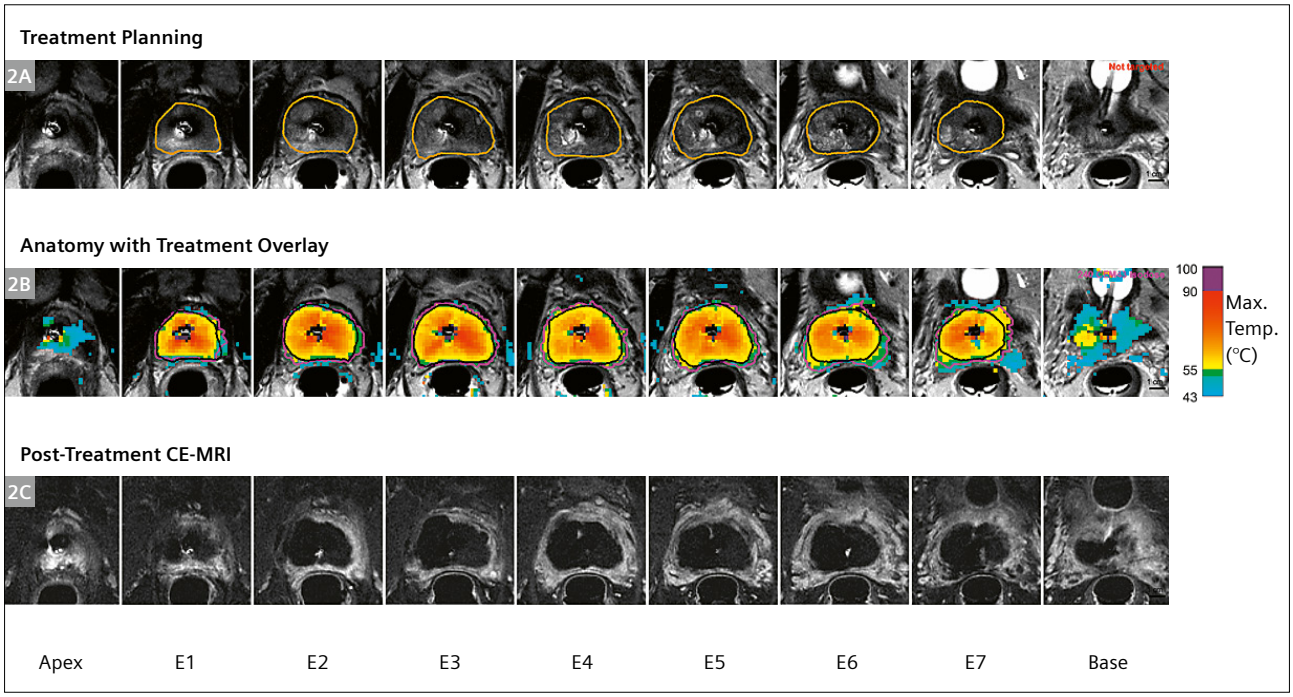

2 **(2A)** Treatment plan outlined on transverse T2w planning sequence. **(2B)** Maximum heat deposition in temperature at the end of treatment. **(2C)** Post-ablation contrast scan showing immediate cell kill based on non-perfused volume.

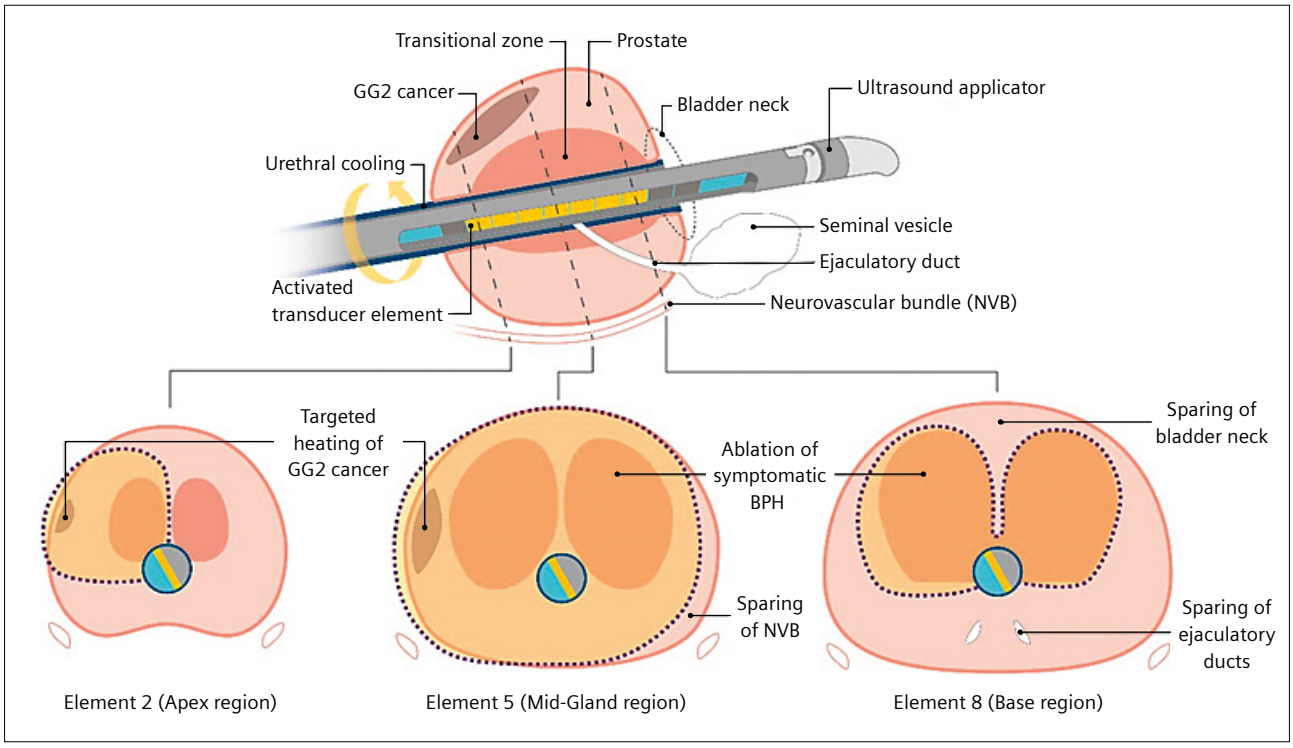

3 Personalized TULSA treatment. A patient presents with both localized intermediate-risk prostate cancer and urinary symptoms prior to treatment. A treatment plan is devised to target only the dominant lesion with a thermal safety margin, as well as the source of adenoma causing urinary obstruction. The apical sphincter, the left side of the neurovascular bundle, the ejaculatory ducts, and the bladder neck are spared from the ablation volume, in order to offer the best compromise between oncological control and function.

TULSA case example: hemi-ablation

A 60-year-old male with intermediate-risk, unilateral, localized PCa (PSA 15 ng/ml, Grade Group 2, PI-RADS 4) arrived at our clinic in 2018. mpMRI findings were concordant with positive biopsy location with the lesion apparent on DWI, outlined in yellow (Fig. 4).

The individualized treatment plan was developed by a multi-disciplinary team including urologists and radiologists, and presented to the patient before the treatment. It was determined the patient would undergo hemi-gland ablation, which would spare one side of the neurovascular bundle, while still targeting the dominant lesion (Fig. 5). The ablation time lasted 35 minutes, with the patient discharged the following day.

At 2 years post-TULSA the patient underwent mpMRI which revealed no suspicions and the PSA was stable at 3.9 ng/ml, a decrease of 74% from baseline which is expected for a focal treatment. No changes to urinary, bowel, or sexual function were noted.

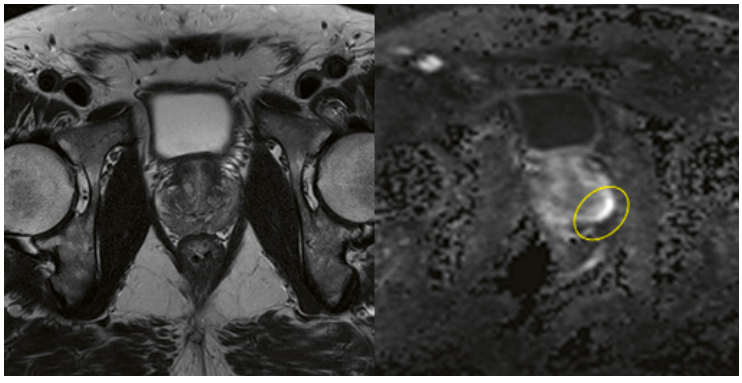

4 Screening image for patient who underwent targeted TULSA treatment. Biopsy showed single lesion Grade Group 2 which was concordant on mpMRI (PI-RADS 4). The lesion is outlined in yellow. Based on the tumor characteristics it was decided the patient would undergo a hemi-ablation on the left side.

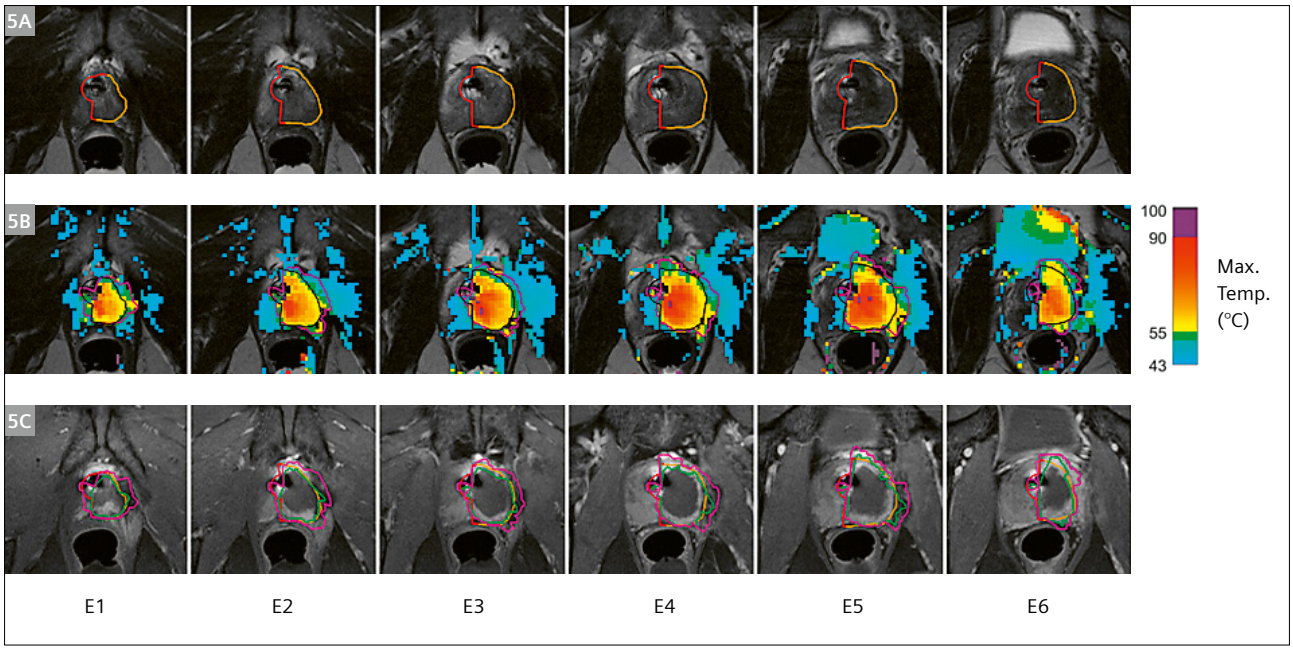

5 Hemi-ablation treatment with TULSA. Elements E1–E6 were enabled on the left lobe to deliver spatially precise ablation in order to reduce toxicity. The treatment plan **(5A)** was determined in advance of the therapy. The ablation lasted only 35 minutes **(5B)** and the immediate treatment effects can be visualized on contrast MRI with the non-perfused volume.

Conclusion

TULSA is a new technology which has demonstrated promising early oncological results with a well-tolerated safety profile. As PCa disease localization continues to improve, it is expected that targeted treatment will become increasingly part of localized PCa management. As MRI is already embedded within TULSA, used both to guide, plan, and monitor treatment, TULSA is well-positioned to address the changing landscape of PCa disease management.

References

1 Siegel RL, et al. Cancer statistics, 2020. A Cancer Journal for Clinicians. 2020;70(1):7-30.
2 Sanda MG, et al. Quality of life and satisfaction with outcome among prostate-cancer survivors. The New England journal of medicine. 2008;358(12):1250-1261.
3 Resnick MJ, et al. Long-term functional outcomes after treatment for localized prostate cancer. The New England journal of medicine. 2013;368(5):436-445.
4 McClure TD, et al. Partial gland ablation in the management of prostate cancer: a review. Current Opinion Urology. 2017;27(2):156-160.
5 Padhani AR, et al. Prostate imaging-reporting and data system steering committee: PI-RADS v2 status update and future directions. European Urology. 2019;75(3):385-396.
6 Chin JL, et al. Magnetic resonance imaging-guided transurethral ultrasound ablation of prostate tissue in patients with localized prostate cancer: a prospective phase 1 clinical trial. European Urology. 2016;70(3):477-455.
7 Eggener S, et al. Pivotal trial of MRI-guided transurethral ultrasound ablation in men with localized prostate cancer: two-year follow-up. The Journal of Urology. 2020;203(4):e369-e369.
8 Ramsay E, et al. Evaluation of focal ablation of magnetic resonance imaging defined prostate cancer using magnetic resonance imaging controlled transurethral ultrasound therapy with prostatectomy as the reference standard. Journal of Urology. 2013;197(1):255-261.
9 Anttinen J, et al. Feasibility of MRI-guided transurethral ultrasound for lesion-targeted ablation of prostate cancer. Scandinavian Journal of Urology. 2019;53(5):295-302.

Joyce Bomers

Jurgen Fütterer

Contact

Professor Jurgen Fütterer, M.D., Ph.D.
Department of Imaging
Radboud University Nijmegen Medical Centre
Geert Grooteplein Zuid 10
6525 GA Nijmegen
The Netherlands
Tel. +31 (0)24 361 40 11
jurgen.futterer@radboudumc.nl

Post Treatment MR of Prostate Cancer

Christopher R. Lunt, MB ChB, FRCR; David J. Ferguson, MB BCh BAO FFR (RCSI), FRCPC; Silvia D. Chang, MD, FRCPC, FSAR

Vancouver General Hospital and BC Cancer, Vancouver, BC, Canada

Multiparametric MRI has in recent years become the imaging method of choice in the investigation of prostate cancer, for detection, decision making regarding targeted biopsy, and to provide information for local staging. MR is also used in the follow up of patients on active surveillance and in those who have undergone treatment of their cancer in the setting of suspected recurrence.

Recurrence of prostate cancer following treatment is most often detected following a rise in serum prostate specific antigen (PSA) levels. How this biochemical recurrence (BR) is defined depends on the modality of treatment; with two consecutive serum PSA concentrations of > 0.2 ng/mL considered to represent BR in patients who have undergone radical prostatectomy (RP), and PSA > 2 ng/mL above the initial nadir value in patients treated with radiotherapy considered to represent recurrence [1].

No consensus values have been established for the newer focal therapies such as cryotherapy or high intensity focused ultrasound (HIFU).

Biochemical recurrence is reported to occur in 27–53% of men treated with curative intent. Between 16–35% of treated men will be given second line therapy, however the interval between initial BR and the need to begin treatment can often be measured in years [2].

Nonetheless local recurrence is associated with an increased risk of metastatic disease, and in patients with local recurrence who are not treated the mean time to detection of distant metastases is 3 years.

Absolute reliance on PSA in the monitoring of treated patients can be unreliable as very poorly differentiated tumors may not produce PSA and this lack of PSA production may be present in the tumor at the time of diagnosis or may occur due to novel mutation in metastatic tumor clone cells later during the period of surveillance. Therefore patients presenting with symptoms attributable to recurrence such as bone pain or symptoms of a pelvic mass or retroperitoneal nodal enlargement should be investigated even in the absence of a serum PSA rise [3].

Initial investigation of men with biochemical recurrence should attempt to establish if the tumor is localized to the residual prostate gland or within the surgical bed in which case radical salvage therapy could be considered, or if distant metastases are present in which case salvage therapy, with its significant associated comorbidity should be avoided in favor of systemic treatment, the timing and method being guided by the location and extent of disease.

Standard assessment for distant metastases in cases of biochemical recurrence in our institutions currently comprises of CT abdomen to assess for lymph node recurrence and MDP bone scan. In cases where the location of

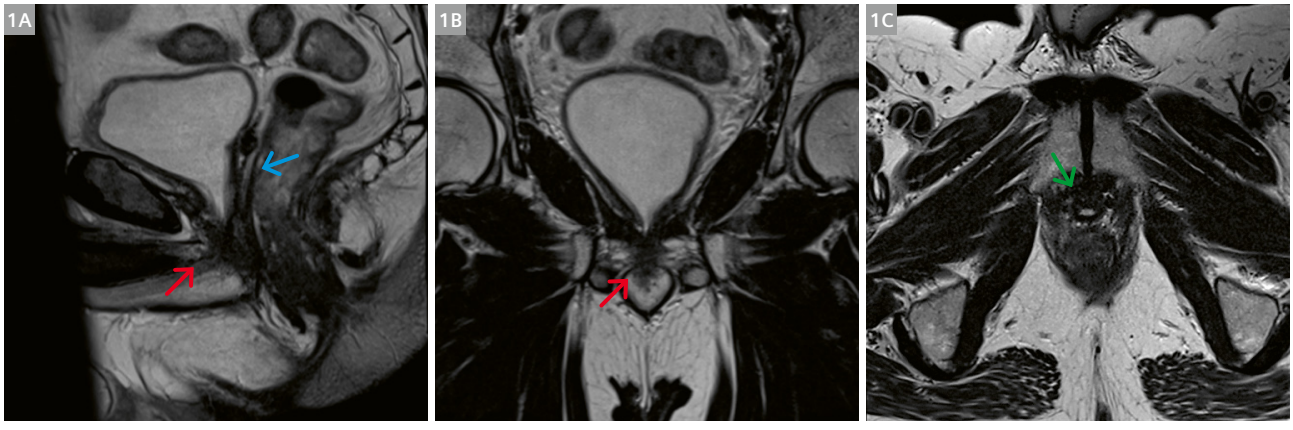

1 Orthogonal T2 sagittal **(1A)**, coronal **(1B)**, and axial **(1C)** small FOV images demonstrating normal MR appearances following radical prostatectomy. The prostate and seminal vesicles are absent and the bladder neck is pulled down to the proximal urethra (red arrows). Uniform low signal scarring is seen at the site of the seminal vesicles (blue arrow). Uniform low signal is seen at the anastomosis, similar to the bladder wall (green arrow).

recurrence is not characterized, a prostate specific membrane antigen (PSMA) PET-CT is currently being trialed.

MR of the prostate or prostate bed in post treatment patients is performed using a standard MR prostate protocol utilizing orthogonal small field of view (FOV) T2, axial diffusion-weighted imaging (DWI), axial wide FOV T1, and dynamic gadolinium enhanced sequences. The latter being crucial to accurate detection in some patients.

Assessment following radical prostatectomy

Surgical removal of the entire prostate gland necessitates the formation of a urethrovesical anastomosis and usually includes removal of the seminal vesicles [4]. Pelvic lymphadenectomy may also be performed at the surgeon's discretion depending on the stage and grade of the tumor as assessed by digital rectal examination, imaging and biopsy histology. Patients with high or intermediate risk disease will usually undergo lymph node dissection, however in low risk disease the need for lymphadenectomy is controversial.

Minimally invasive prostatectomy is now the most commonly employed surgical technique with or without robotic assistance [5]. This may include nerve sparing in suitable patients in an attempt to preserve sexual function.

Following prostatectomy the serum PSA level is expected to fall to < 0.2 ng/mL, in the event this does not occur, residual local disease or occult distant metastases should be suspected.

Normal MR appearances following RP show the bladder neck pulled down to form an inverted conical shape and the vesico-urethral anastomosis which should appear uniformly low signal on the T2 sequences due to the presence of fibrotic tissue. There should be no or minimal evidence of diffusion restriction around the anastomosis, and no early contrast enhancement, however delayed uniform enhancement of the fibrotic tissue is normal (Fig. 1).

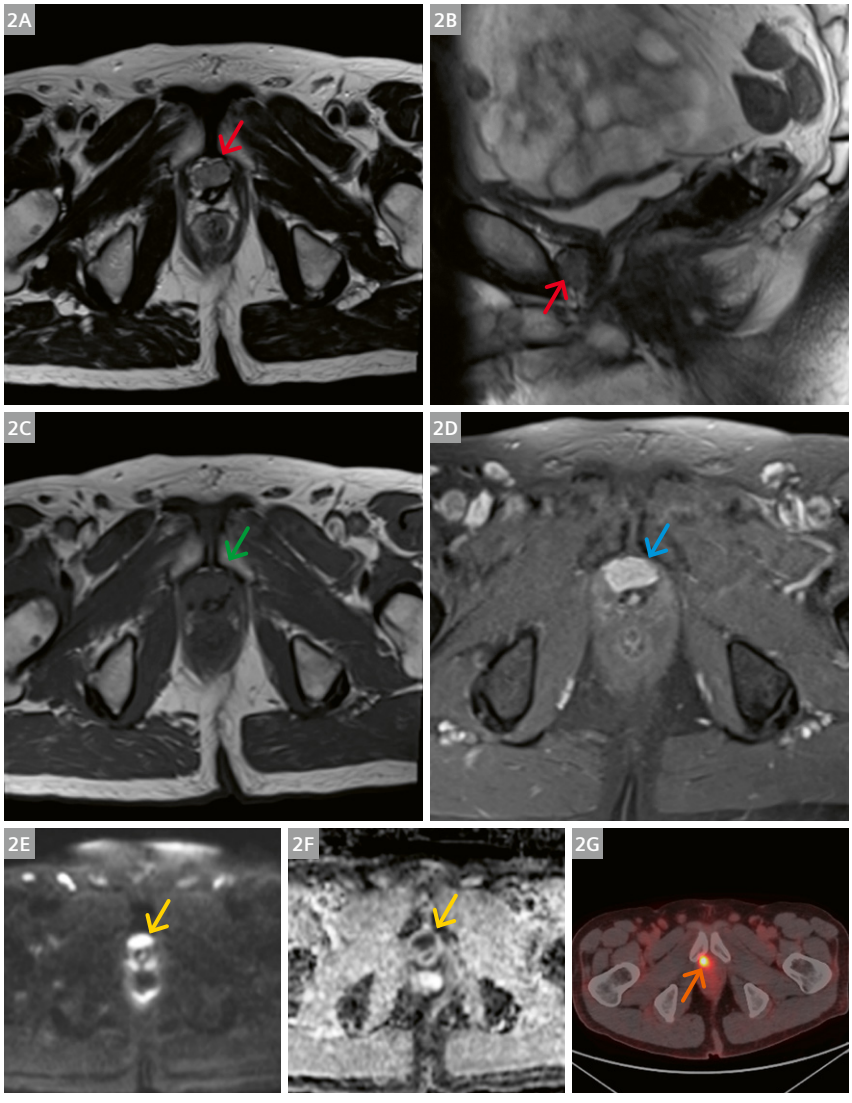

2 **(2A, B)** T2 axial and sagittal images demonstrating recurrence anterior to the anastomosis following radical prostatectomy seen as intermediate signal tumor (red arrows). **(2C)** T1 sequence, tumor is isointense to skeletal muscle (green arrow). **(2D)** Tumor shows avid enhancement following gadolinium contrast administration (blue arrow). **(2E, F)** Tumor shows restricted diffusion with low signal on ADC sequence (yellow arrows). **(2G)** PSMA PET-CT shows isotope uptake within the area of tumor seen on MR (orange arrow).

Local recurrence occurs in 23–43% of patients, most commonly at the anastomosis (75%), or in a retained portion of a seminal vesicle or vas deferens (20%). Soft tissue in the prostatectomy bed away from the anastomosis and nodal or visible skeletal metastases should also be carefully excluded in the setting of rising PSA. The typical appearance of recurrent local disease is soft tissue which is isointense to skeletal muscle on T1 sequences, slightly hyper-intense to muscle on T2 and demonstrates diffusion restriction and rapid contrast enhancement and washout (Fig. 2).

Prostate MR following external beam radiotherapy

The use of external beam radiotherapy (EBRT) for treatment of prostate cancer is primarily associated with lower risk tumors, although with the addition of androgen deprivation therapy (ADT) higher risk tumors can also be treated, often in the setting of patients with significant comorbidity precluding surgery or in patients who have declined invasive treatment [2].

Biochemical recurrence following RT is defined as a PSA rise of > 2 ng/mL above the initial PSA nadir. In this setting localization of the site of recurrence is crucial as salvage surgery carries significant morbidity and should be reserved for those patients who might still be cured. Therefore confirmation through biopsy is mandatory.

Following EBRT the prostate gland shows diffuse atrophy with reduced signal on T2 sequences which can mask areas of recurrent tumor. Normal differentiation between the peripheral and transition zones becomes indistinct and post EBRT changes in the adjacent muscle and bone marrow may be seen. Atrophy of the seminal vesicles is commonly seen [6] (Fig. 3).

Recurrence most often occurs at the site of initial tumor and may still appear lower in T2 signal than the surrounding prostate tissue. Multiparametric (mp) MRI has been shown to be superior to anatomical imaging, and diffusion restriction or tissue demonstrating early enhancement with washout should be considered suspicious. Gradual enhancement without washout is typically seen in patients treated with RT [7] (Fig. 4).

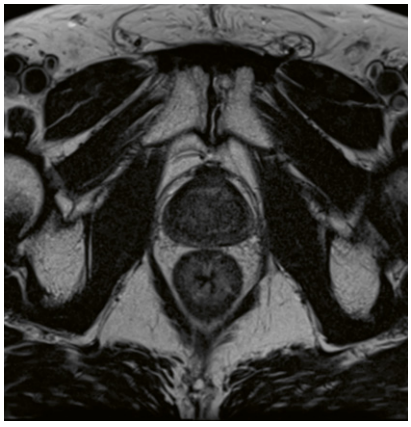

3 Expected findings following external beam radiotherapy (EBRT): Diffuse atrophy of prostate with decreased signal on T2 sequences, loss of normal distinction between peripheral and transition zones, increase T2 signal in muscle and bone marrow. Diffuse low signal thickening of bladder and rectal walls may also be seen.

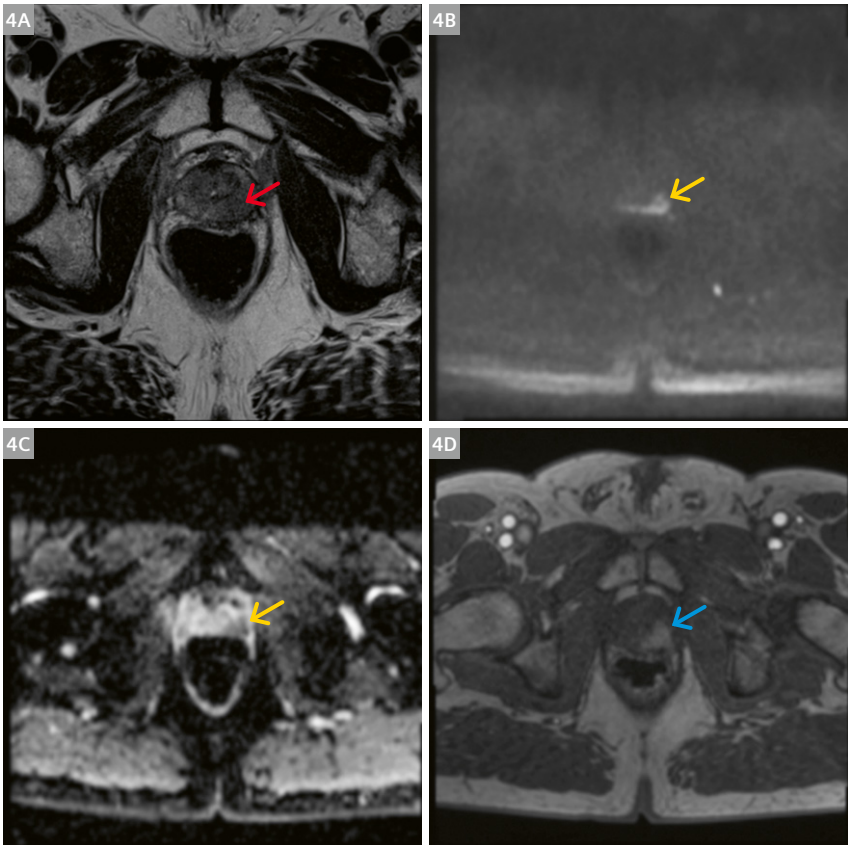

4 Recurrence of prostate cancer following EBRT. **(4A)** T2 axial image showing subtle low signal in the left midgland (red arrow), **(4B)** corresponding high signal on DWI (yellow arrow) and **(4C)** low ADC values (yellow arrow) with **(4D)** avid contrast enhancement on DCE sequence (blue arrow) in keeping with tumor.

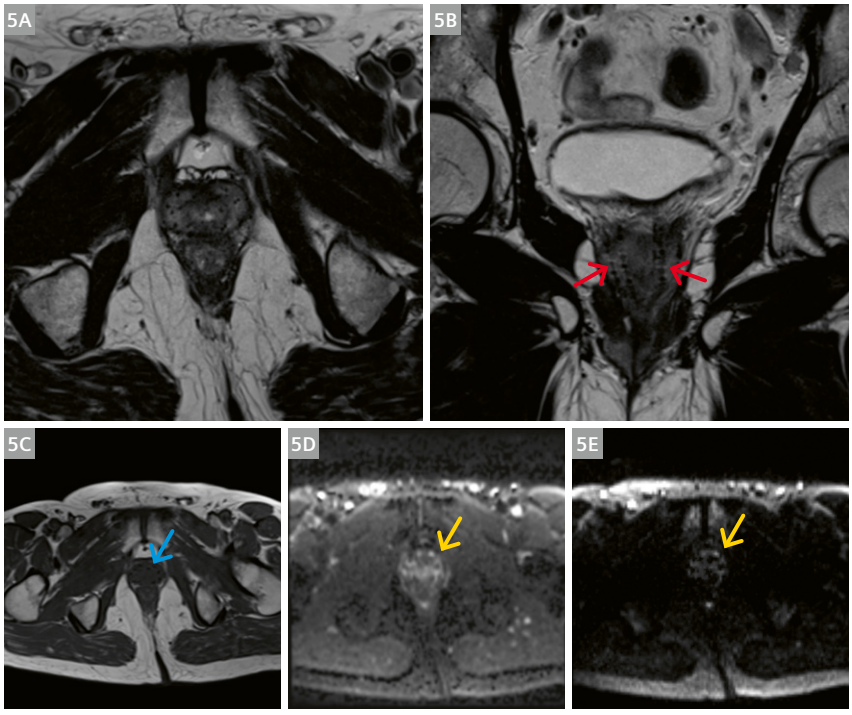

5 Normal appearances following brachytherapy: **(5A, B)** Homogeneous low T2 signal throughout the gland with reduced differentiation between peripheral and transitional zones. **(5B)** On the coronal image, seeds are seen to run in parallel (red arrows). **(5C)** T1 images show seeds with susceptibility artifact (blue arrow). **(5D, E)** DWI and ADC sequences show marked susceptibility artifact limiting use (yellow arrows).

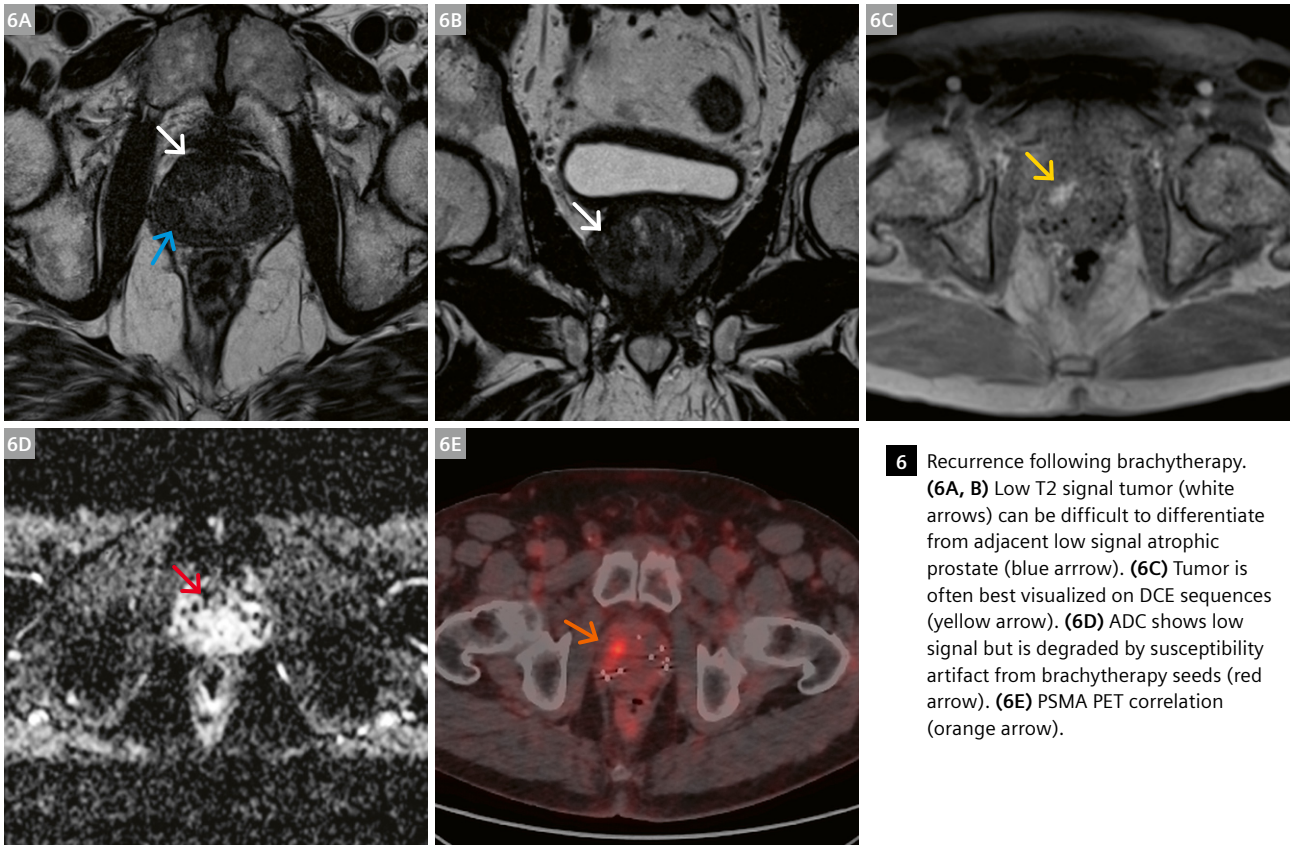

6 Recurrence following brachytherapy. **(6A, B)** Low T2 signal tumor (white arrows) can be difficult to differentiate from adjacent low signal atrophic prostate (blue arrrow). **(6C)** Tumor is often best visualized on DCE sequences (yellow arrow). **(6D)** ADC shows low signal but is degraded by susceptibility artifact from brachytherapy seeds (red arrow). **(6E)** PSMA PET correlation (orange arrow).

Trans-perineal brachytherapy

The insertion of metal seeds into the prostate to deliver highly localized doses of ionizing radiation is performed using a transrectal ultrasound probe and a template grid for guidance. Typically patients with low grade, low volume cancer are offered brachytherapy if there has been no previous prostatic surgery (TURP), the prostate volume is below 50 mL and the International Prostate Symptom Score is ≤ 12 [2].

No consensus exists regarding the definition of biochemical recurrence in patients treated with brachytherapy [1, 8]. 30–60% of patients experience a rise in PSA around one year following the insertion of the seeds which can last for around 12 months. After this period a persistently rising PSA should be viewed with suspicion.

Brachytherapy causes a similar appearance in the prostatic parenchyma to EBRT with homogeneous low T2 signal and loss of normal zonal anatomy. The low signal associated with treatment can mask low signal recurrence. In addition, multiple seeds can be visualized running in parallel on coronal images and may also be seen outside of the gland in the periprostatic fat, the bladder wall and in the base of the penis/perineum (Fig. 5). Areas of susceptibility artifact due to seeds severely limit the interpretation of DWI sequences and recurrences are often best visualized using DCE [6] (Fig. 6).

Androgen deprivation therapy (ADT)

Androgen deprivation therapy can be used in the setting of incurable disease or as an adjunct to radiotherapy. Initial treatment can often result in a significant reduction in tumor volume. Diverse morphologic and signal changes are possible following the initiation of ADT with diffuse atrophy of the gland due to apoptosis of prostate cells the most commonly seen appearance. Loss of the normal zonal definition due to decreased peripheral zone signal is often seen, and the seminal vesicles usually atrophy. Residual tumor can be identified by areas of diffusion restriction and rapid enhancement with washout [9, 10] (Figs. 7, 8).

Focal therapies

Various modalities for the focal treatments of prostate cancer have been proposed and implemented in recent years, most relying on targeted destruction of localized areas of the prostate gland where tumor is located.

Cryotherapy involves ablation tissue by extremely cold temperatures using probes inserted transperineally

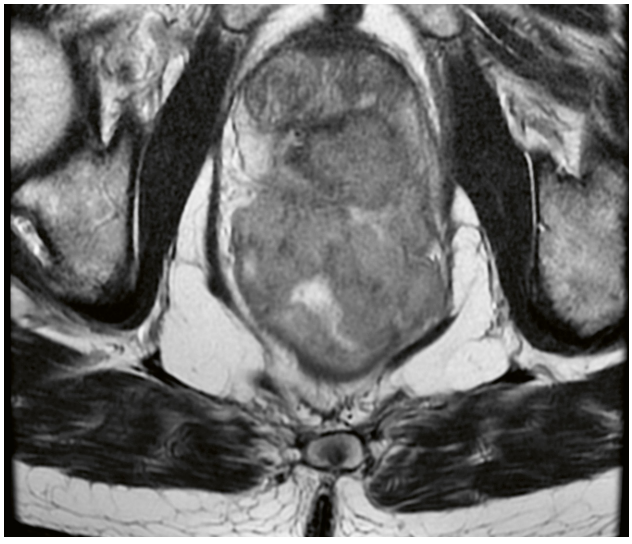

7 Pre ADT axial T2 image with extensive tumor invading the rectum and pelvic sidewall.

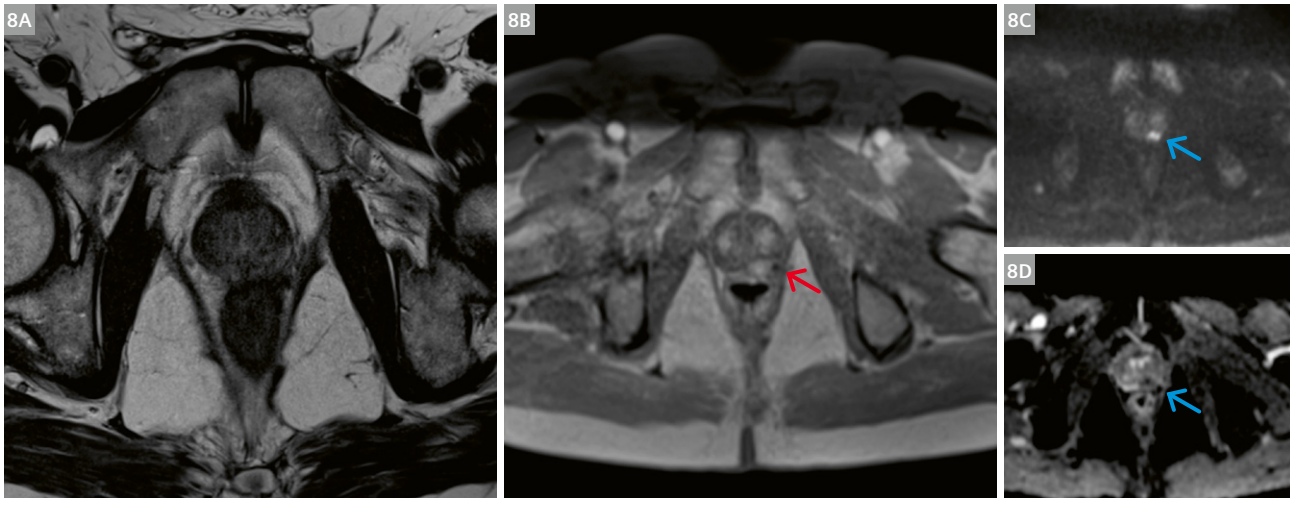

8 Same patient following 8 months of ADT treatment. **(8A)** T2 image showing marked reduction in tumor volume without clearly identifiable residual disease. **(8B)** Left mid gland peripheral zone tumor is seen on DCE (red arrow) and **(8C)** DWI, and **(8D)** ADC sequences (blue arrows).

using a template grid. Ice ball formation leads to lysis of cells within the treatment zone.

High intensity focused ultrasound causes coagulation necrosis by converting mechanical energy into heat and generating a cavitation affect.

Photodynamic therapy involves pre-treatment of the patient with a photosensitizer molecule which absorbs light of a specific frequency and transfers energy to adjacent oxygen molecules creating reactive oxygen species that trigger cell destruction.

Focal laser ablation involves thermal destruction of tissue via a fiberoptic cable placed within the tumor and is performed with MR guidance.

Irreversible electroporation uses two electrodes to increase the permeability of cell membranes leading to apoptosis and necrosis.

Post treatment appearances following focal therapy are variable; often a central zone of necrosis is demonstrated with absence of enhancement, surrounded by an enhancing rim of granulation tissue. The T2 sequences often demonstrate heterogeneous or hypointense signal in the area of treatment. High signal on T1 sequences can be seen due to hemorrhage and blood products, and therefore subtraction sequences are important to differentiate this from enhancement (Fig. 9).

Recurrence following focal therapy can appear as low signal which blends in with the adjacent low T2 signal fibrotic tissue. Low ADC values are suspicious only if combined with high signal on the DWI sequence in order to accurately distinguish recurrent tumor from areas of fibrotic tissue.

Focal enhancement with washout is also suspicious for residual viable tumor however areas of nodular enhancement at the borders of treated lesions secondary to reactive normal prostate tissue can mimic recurrence [11].

Mimics of recurrence

Retained seminal vesicle: Often first identified on CT, the seminal vesicle is retained in 20% of radical prostatectomies [12], commonly related to difficulties in surgical technique or intentionally to reduce the risk of neurovascular bundle injury. MR typically demonstrates a typical convoluted appearance with no evidence of diffusion restriction or abnormal enhancement (Fig. 11).

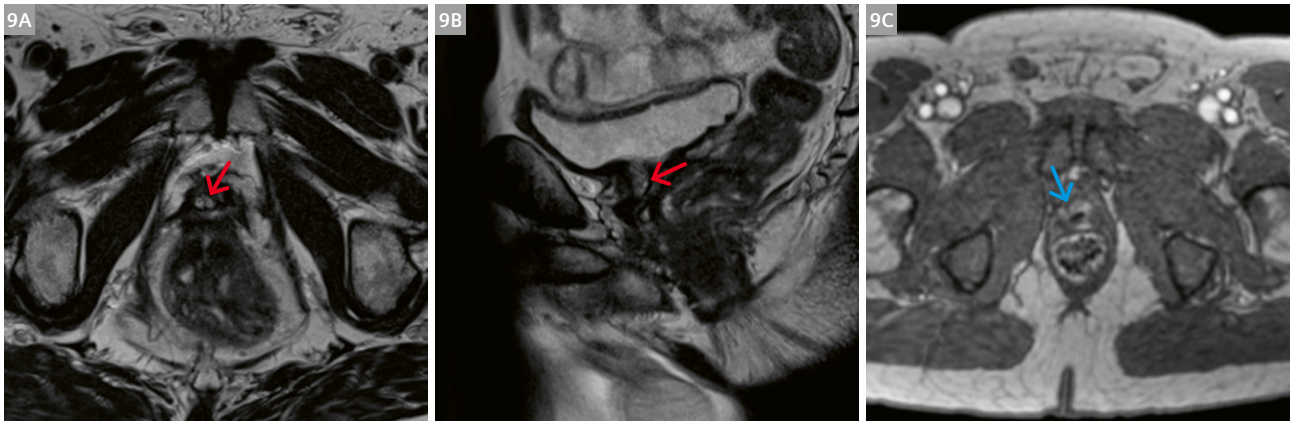

9 **(9A, B)** Axial and sagittal images showing post HIFU ablation zone with central areal of high signal necrosis (red arrows). **(9C)** Axial DCE image showing peripheral rim enhancement around the site of ablation in a different patient (blue arrow).

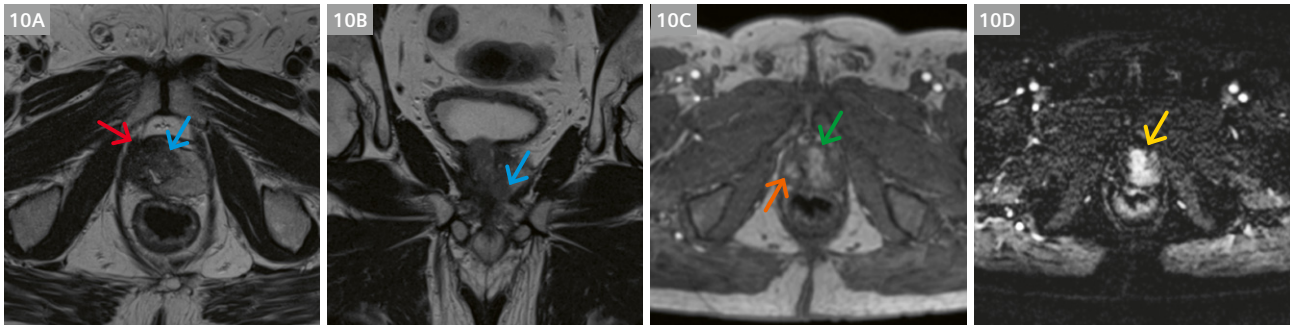

10 Recurrence following phototherapy. **(10A, B)** T2 sequence showing low signal fibrosis at treatment site (red arrow) with adjacent intermediate signal recurrence (blue arrows). **(10C, D)** DCE images show enhancement corresponding to the area of abnormality (green arrow). Subtraction images are mandatory to distinguish blood product within the treatment zone (orange arrow) from enhancing tumor (yellow arrow).

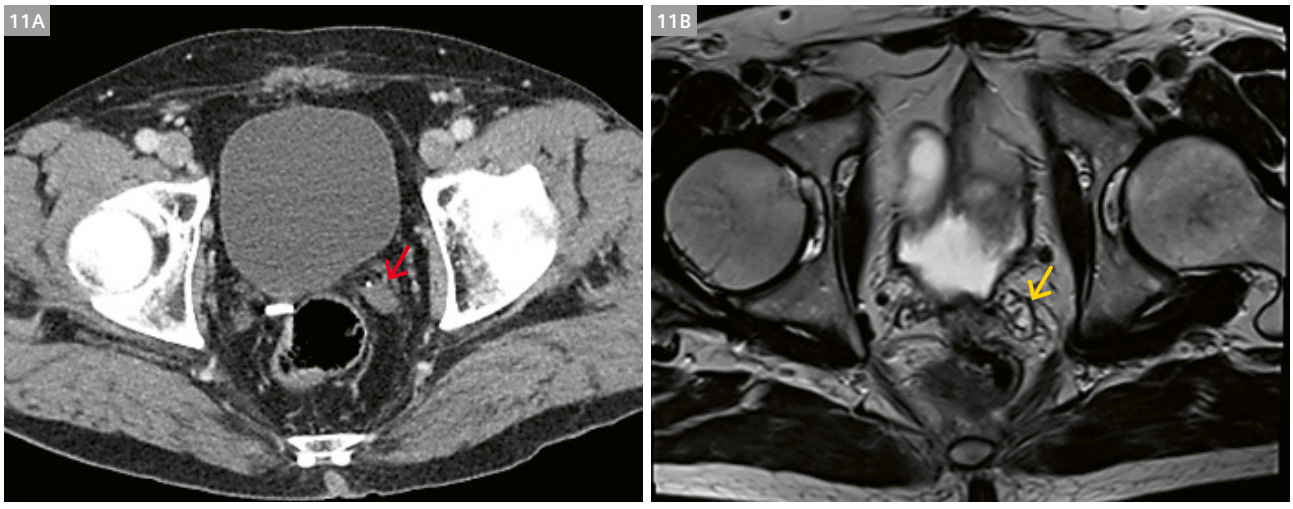

11 **(11A)** Retained seminal vesicle can be mistaken for recurrence especially on CT (red arrow). **(11B)** Characteristic convoluted appearance on T2-weighted MR confirms diagnosis (yellow arrow).

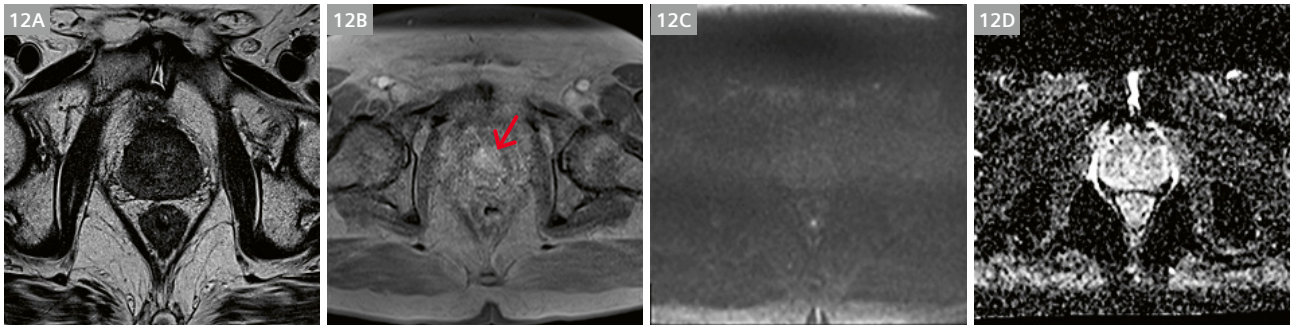

12 Fibrosis or scar tissue following radiotherapy can be difficult to distinguish from tumor. **(12A)** Scar is diffusely low signal on T2, **(12B)** 3 minute delayed post gadolinium sequence demonstrates late enhancement (red arrow). **(12C, D)** Absence of diffusion restriction.

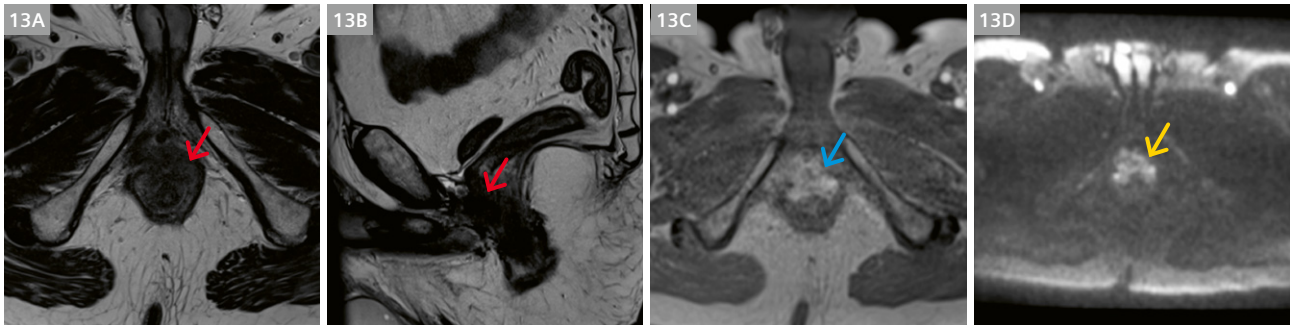

13 Low signal tumor involving prostate resection bed in a patient treated with radiotherapy and salvage cystoprostatectomy following recurrence, biopsy showed invasive rectal adenocarcinoma. **(13A, B)** Low signal in resection bed involving rectum (red arrows). **(13C)** Enhancing tumor (blue arrow), **(13D)** diffusion restriction (yellow arrow).

Focal fibrosis or scarring is commonly seen following EBRT and tissue appears low signal on T2 with no diffusion restriction and diffuse high values on the ADC map. Enhancement should be absent or show delayed gradual uptake without rapid washout (Fig. 12).

Granulation tissue tends to show high signal on T2 sequences with no evidence of diffusion restriction or early enhancement.

The occurrence of secondary cancers due to prior pelvic radiotherapy is somewhat controversial however abnormal findings within the prostatic bed following radiotherapy or prostatectomy can also be related to tumors arising in adjacent structures and careful examination of the other pelvic organs is mandatory. Unusual tumor behaviour such as failure to respond to ADT in a blockade naïve patient should prompt consideration of biopsy (Fig. 13).

Conclusion

Early detection and localization of recurrent prostate cancer is important for treatment planning and prognosis. Detection in post treatment cases can be challenging however advances in mp-MRI help to differentiate recurrence from mimics with DCE sequences being key in post treatment cases. Radiologist familiarity with imaging appearances of recurrence and mimics helps to make a correct and timely diagnosis.

Contact

Associate Professor Silvia Chang, M.D., FRCPC
Department of Radiology
Vancouver General Hospital
899 West 12th Avenue
Vancouver, BC V5Z 1M9
Canada
Tel.: +1 (604) 875-4340
Silvia.Chang@vch.ca

References

1 Cookson MS, Aus G, Burnett AL, et al. Variation in the definition of biochemical recurrence in patients treated for localized prostate cancer: the American Urological Association Prostate Guidelines for Localized Prostate Cancer Update Panel report and recommendations for a standard in the reporting of surgical outcomes. J Urol. 2007;177(2):540-545.
2 Mottet N, Bellmunt J, Bolla M, et al. EAU-ESTRO-SIOG Guidelines on Prostate Cancer. Part 1: Screening, Diagnosis, and Local Treatment with Curative Intent. Eur Urol. 2017;71(4):618-629.
3 Cornford P, Bellmunt J, Bolla M, et al. EAU-ESTRO-SIOG Guidelines on Prostate Cancer. Part II: Treatment of Relapsing, Metastatic, and Castration-Resistant Prostate Cancer. Eur Urol. 2017;71(4):630-642.
4 Allen SD, Thompson A, Sohaib SA. The normal post-surgical anatomy of the male pelvis following radical prostatectomy as assessed by magnetic resonance imaging. Eur Radiol. 2008;18(6):1281-1291.
5 Tyson MD, II, Andrews PE, Ferrigni RF, Humphreys MR, Parker AS, Castle EP. Radical Prostatectomy Trends in the United States: 1998 to 2011. Mayo Clinic Proceedings. 2016;91(1):10–16.
6 Rouvière O, Vitry T, Lyonnet D. Imaging of prostate cancer local recurrences: why and how? Eur Radiol. 2010;20(5):1254-1266.
7 Roy C, Foudi F, Charton J, et al. Comparative sensitivities of functional MRI sequences in detection of local recurrence of prostate carcinoma after radical prostatectomy or external-beam radiotherapy. AJR Am J Roentgenol. 2013;200(4):W361-368.
8 Roach M, Hanks G, Thames H, et al. Defining biochemical failure following radiotherapy with or without hormonal therapy in men with clinically localized prostate cancer: recommendations of the RTOG-ASTRO Phoenix Consensus Conference. Int J Radiat Oncol Biol Phys. 2006;65(4):965-974.
9 Kim AY, Kim CK, Park SY, Park BK. Diffusion-weighted imaging to evaluate for changes from androgen deprivation therapy in prostate cancer. AJR Am J Roentgenol. 2014;203(6):W645-650.
10 Hötker AM, Mazaheri Y, Zheng J, et al. Prostate Cancer: assessing the effects of androgen-deprivation therapy using quantitative diffusion-weighted and dynamic contrast-enhanced MRI. Eur Radiol. 2015;25(9):2665-2672.
11 De Visschere PJ, De Meerleer GO, Fütterer JJ, Villeirs GM. Role of MRI in follow-up after focal therapy for prostate carcinoma. AJR Am J Roentgenol. 2010;194(6):1427-1433.
12 Sella T, Schwartz LH, Hricak H. Retained seminal vesicles after radical prostatectomy: frequency, MRI characteristics, and clinical relevance. AJR Am J Roentgenol. 2006;186(2):539-546.

Quantitative WB-MRI with ADC Histogram Analysis for Complex Response of Bone Marrow Metastatic Disease

Danoob Dalili[1]; Anwar R. Padhani[2]; Robert Grimm[3]

[1] Imperial College Healthcare NHS Trust, St Mary's Hospital, London, United Kingdom
[2] Paul Strickland Scanner Centre, Mount Vernon Cancer Centre, Northwood, Middlesex, United Kingdom
[3] Siemens Healthineers, Erlangen, Germany

Introduction

Bone metastases and bone specific malignancies such as multiple myeloma, remain diagnostically challenging not only for disease detection, but also when monitoring disease response to treatments. Recently, whole-body MRI (WB-MRI) incorporating diffusion sequences has been shown to be able to potentially advance the care of breast and prostate cancer patients who have a high metastatic bone disease prevalence, by improving disease detection [1, 2]. In 2015, WB-MRI was accepted into patient care guidelines by the International Myeloma Working Group [3] for disease detection and prognostication.

The incorporation of diffusion imaging sequences into WB-MRI protocols has been shown to improve both bone disease detection and response assessments. WB-MRI with diffusion sequences has the potential to alter clinical diagnostic thinking when assessing bone disease response. This is because it becomes possible to positively assess the success of therapy benefit in diseased bone, which is not possible when using CT and bone scans. Imaging standards for the conduct and systematic reporting of WB-MRI, including therapy response criteria were recently published [4].

Figure 1: Morphological images and high b-value DWI, maximum intensity projections (MIPs).

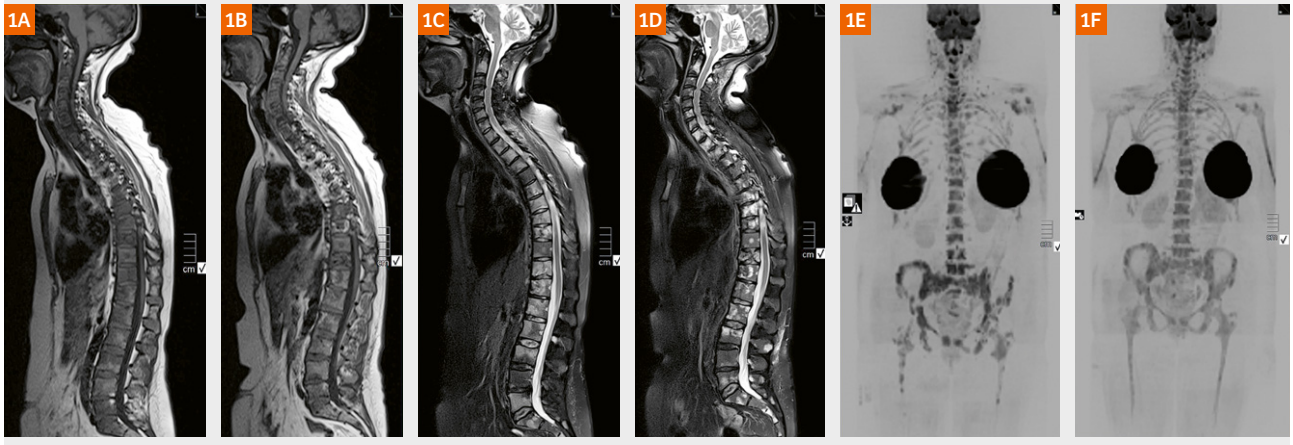

Left 2-columns **(1A, 1B)**: Whole-spine sagittal T1-weighted images show diffuse bone marrow infiltration (1A) with some return of bone marrow fat after chemotherapy (1B).

Middle 2-columns **(1C, 1D)**: Whole-spine sagittal T2w-fs sequences show diffuse bone marrow infiltration (1C) with subtle increases in signal intensity following chemotherapy (1D). The increases in T2w bone marrow signal intensity after therapy are consistent with alternations in tissue water content which is associated with tumor cell kill.

Right 2-columns **(1E, 1F)**: Whole-body b900 3D MIP (inverted scale). The bone marrow is diffusely involved with diffuse regions of high signal intensity in the axial skeleton and in the proximal limb bones before therapy (1E). A global reduction in the b900 signal intensity of bone marrow can be seen, consistent with disease response (1F). There is also uniform increase in extent of signal in the limbs consistent with bone marrow regeneration. Bilateral breast prostheses are also visible.

Uniquely, diffusion imaging brings a degree of objectivity to response assessments, using quantitative apparent diffusion coefficient measurements (ADC; unit $\mu m^2/s$). ADC maps of whole-body disease load, allow objective assessments of bone tumor load and therapy response [5]. There is a high inter and intra-observer agreement of whole-body ADC mapping [6]. Semi-automated threshold-based, quantitative ADC mapping and histogram analysis software, allow deployment of whole-body ADC mapping into the clinic [7].

There is a need for radiologists to understand the biological meaning and likely clinical implications of changes observed in quantitative whole-body ADC maps and histograms. This is particularly the case for malignant bone disease, where diffusion signal changes can arise from the normal bone marrow as well as from malignant tissues, both of which can be intermixed. Several articles have been published in MAGNETOM Flash illustrating the ADC back-mapping technique [7, 8] and tumor therapy response applications [8]. These illustrations have noted that ADC changes reflect on the mechanism of tumor cell death and the re-emergence of tumor cells when therapy resistance arises. In this case report, we demonstrate the ability of the whole-body tumor load software to distinguish ADC changes ascribable to tumor response and bone marrow recovery with successful therapy. Longer-term changes are described in a companion case [9] in this issue of MAGNETOM Flash magazine.

Case study

A 52-year-old woman underwent bilateral mastectomies and reconstructions for multifocal, ER+ bilateral breast cancer in 2010. 4 years later she re-presented with 6 months of bone pain while taking adjuvant Tamoxifen therapy. She was restaged with a whole-body MRI study for disease detection. A response assessment WB-MRI study was undertaken 14 weeks later, following 4 cycles of FEC chemotherapy and bisphosphonates (without growth factor support) (Figs. 1, 2). Unfortunately, 4 months later she developed intracranial metastatic disease and expired.

Continued on page 41.

Figure 2: Morphologic and diffusion-weighted images of the L2 vertebral body.

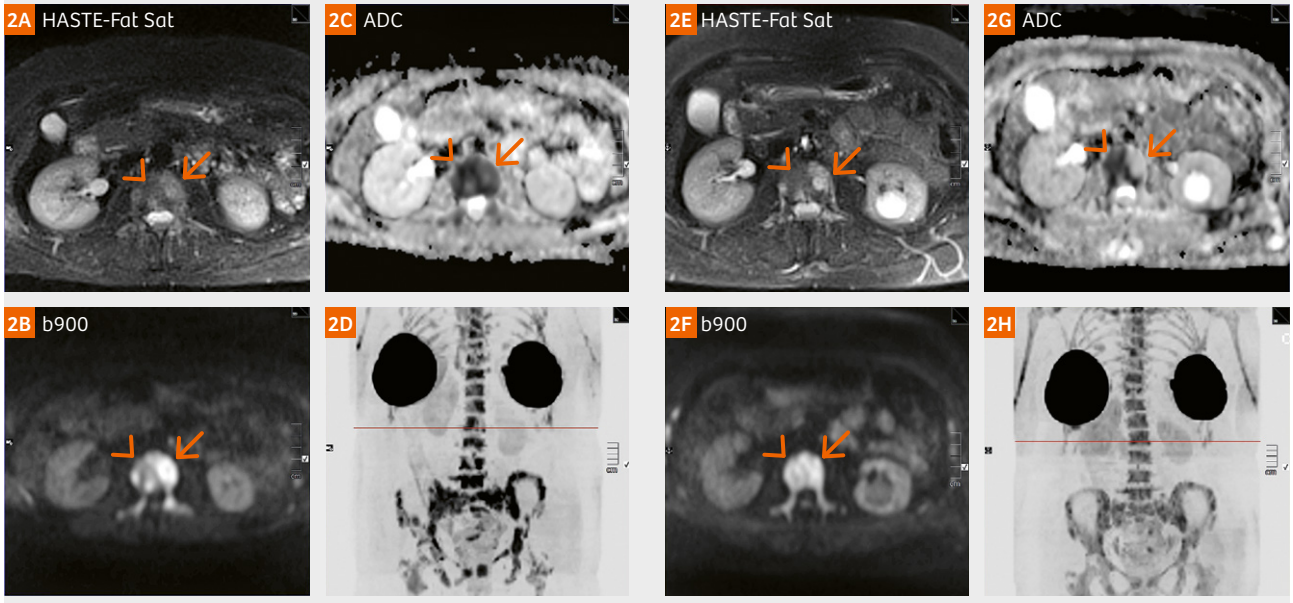

Axial HASTE-Fat Sat, b = 900 s/mm² and ADC images with zoomed whole-body b900 3D MIP (inverted scale) before and after therapy. Axial images are through the L2 vertebral body as indicated by the red reference line. The follow-up images (right 2 columns, **2E-H**) demonstrated excellent response to treatment, with increases in apparent diffusion coefficient (ADC) values for the metastatic deposit in the left side of the vertebral body (arrows). The bone marrow in the right side of the vertebral body (arrow head) demonstrates lowering of ADC values. In this area, the bone marrow T1w-fat percentage (F%) on corresponding Dixon images (not shown) changed from 20% to 26%.

Figure 3: Whole-body tumor load analysis.

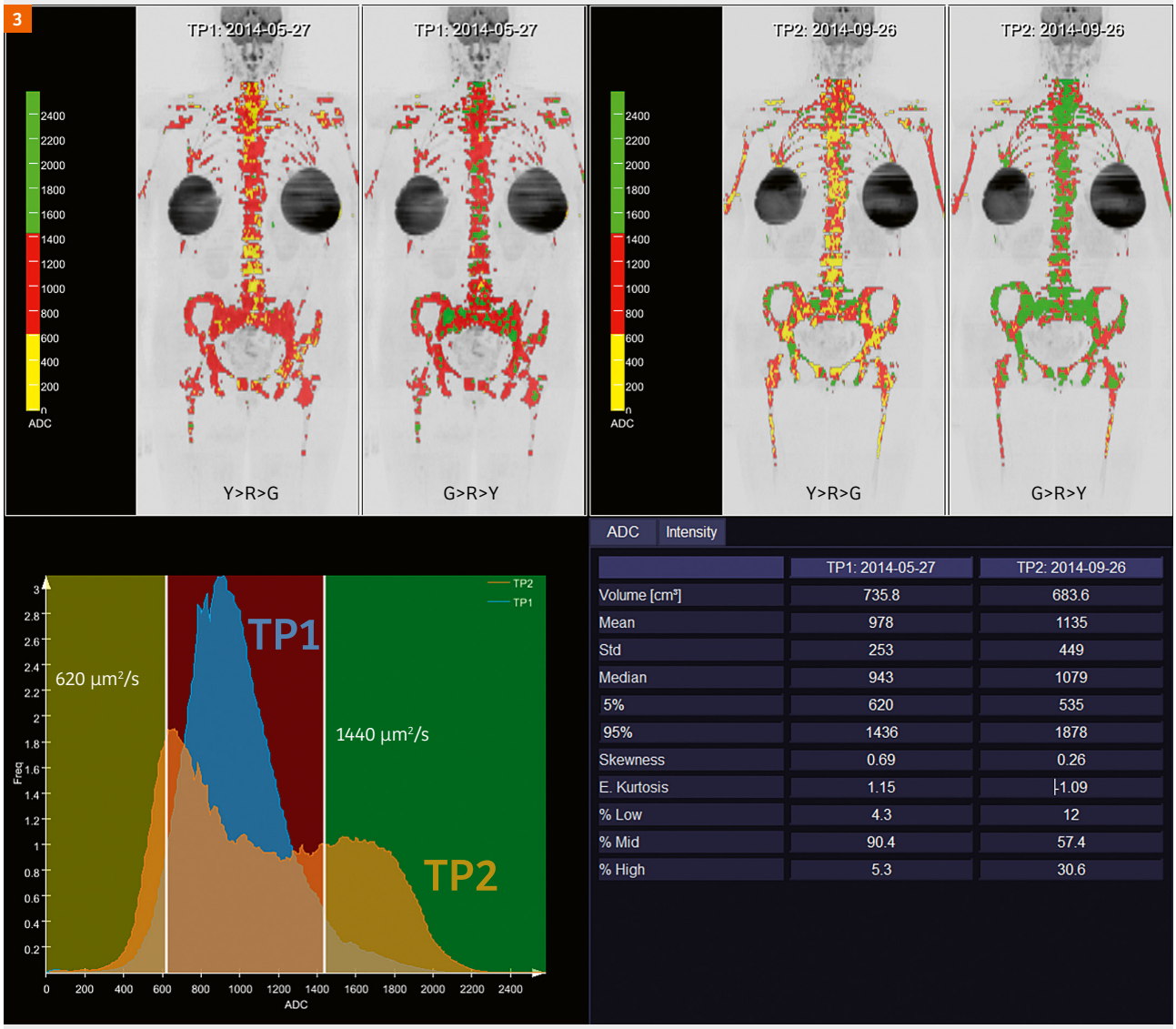

	TP1: 2014-05-27	TP2: 2014-09-26
Volume [cm³]	735.8	683.6
Mean	978	1135
Std	253	449
Median	943	1079
5%	620	535
95%	1436	1878
Skewness	0.69	0.26
E. Kurtosis	1.15	-1.09
% Low	4.3	12
% Mid	90.4	57.4
% High	5.3	30.6

WB-tumor load segmentations were undertaken on *syngo.via* Frontier MR Total Tumor Load software[1] (Siemens Healthcare, released research prototype). The whole-body b900 images were segmented using computed high b-value images of 1000–1200 s/mm², setting a signal intensity threshold of approximately 30 AU. Extraneous signals (such as the brain, thyroid, kidneys, spleen, breast prostheses and bowel) were removed, to leave only recognizable bone sites. The b900 MIP images are overlaid with ADC value classes using the 5th and 95th centile values of the pre-treatment histogram (620 and 1440 µm²/s respectively). Red colored voxels represent untreated disease or those that have no-detected response. Green colored voxels have ADC values ≥ 1440 µm²/s (representing voxels that have increased in ADC values and are 'likely' to be responding). The yellow voxels lie below the 5th centile ADC value of the pre-treatment histogram (620 µm²/s). Thus, yellow voxels represent regions 'likely' to represent normal bone marrow.

736 mL of bone marrow was segmented before therapy and 684 mL after chemotherapy. Note that there is a global increase in median ADC values (943 µm²/s and 1079 µm²/s respectively), a decrease in excess kurtosis (1.15 and -1.1), and broadening of ADC histogram shown by an increase in the ADC standard deviation (253 and 449 µm²/s respectively), of the corresponding relative frequency histograms. There is unimodal distribution of ADC values before (TP1) and a bimodal distribution of the post-treatment (TP2) histogram. Note increasing numbers of yellow and green voxels representing normal bone marrow and cell kill respectively. There are also areas of red indicating residual active disease on TP2.

The color whole-body ADC class back-maps are of two types for each time point. On the left is the ADC color projection focusing on normal bone marrow (yellow voxels; MIP-ADC low image), and on the right of each pair is the ADC color projections focusing on response (green voxels; MIP-ADC high image).

The whole-body MRI scans with diffusion-weighted sequences were undertaken using a 1.5T MAGNETOM Avanto scanner using a published protocol [3]. The baseline scan (TP1) demonstrated extensive metastatic bone only disease (Figs. 1, 2) on morphological T1w and T2w-fs images of the spine.

The follow-up WB-MRI (TP2) demonstrated excellent response to treatment, with decreases in b = 900 s/mm² signal intensity and corresponding increases in apparent diffusion coefficient (ADC) values for individual metastatic deposits (Fig. 2 – arrows). Normal bone marrow return was also noted with increasing fat in the bone marrow (Fig. 2 – arrow heads).

The diffusion-weighted images for both examinations were analysed using threshold-based segmentation with *syngo*.via Frontier MR Total Tumour Load software[1] [7]. The pre-treatment ADC histogram has a unimodal distribution of ADC values (Fig. 3). After 4 cycles of chemotherapy, a bimodal distribution can be seen (Fig. 3). Increased voxels with high ADC values > 1500 µm²/s indicate the presence of tumor cell kill (arrows in Fig. 2). A new peak to the left of the pre-treatment ADC histogram represents the re-emergence of normal bone marrow (Fig. 3).

Discussion

The total tumor load software has been developed to enhance the value of ADC histogram analysis for assessing therapy response. The location of histogram ADC values is undertaken by color-coded projections of ADC classes on the b900 MIP images (MIP-ADC class pairing). In so doing, it is possible to anatomically localize the anatomic site and likely biologic state of the tissues. In this case example, normal bone marrow was assigned to ADC values that are lower than 620 µm²/s [10, 11] and displayed as yellow, voxels between 620 µm²/s and 1440 µm²/s are color coded as red (the 5th–95th centile values of the pre-treatment (TP1) ADC histogram), voxels with an ADC above 1440 µm²/s are shown in green, representing likely response.

The software, allows cycling through these color layers in order to focus the visualization on normal bone marrow (yellow), untreated active disease (red) or likely response (green), respectively (Fig. 4). Since only one color can be projected onto the segmented mask, the following rules are applied for the bone ADC color scheme (from lower to higher ADC values, Yellow-Red-Green).

[1] *syngo*.via Frontier is for research only, not a medical device. *syngo*.via Frontier MR Total Tumor Load is a released research prototype.

ADC color projections focusing on marrow are shown on the left of each MIP-ADC class pair, if at least one voxel of the segmented bone has an ADC of less than 620 µm²/s, it will be assigned the yellow color (MIP-ADC low). Otherwise, it will be colored in red if any ADC is between 620 and 1440 µm²/s, or in green, if all ADC values along the projection are above 1440 µm²/s. Thus, the resulting projected color order for normal bone marrow is Yellow > Red > Green.

ADC color projections focusing on response are on the right of each image pair (MIP-ADC high). If at least one voxel of the segmented bone has an ADC of 1440 µm²/s or higher, it will be assigned a green color. Otherwise, it will be colored in red if the ADC falls between 620 and 1440 µm²/s, or in yellow, if all ADC values along the projection are below 620 µm²/s. Thus, the corresponding projected color order for assessing response is Green > Red > Yellow.

The use of ADC color projections, histograms and descriptive histogram statistics enables an easier to understand and objective method of assessing therapy response in bone marrow malignancies. When complex ADC changes occur simultaneously, as in this case (tumor response and bone marrow recovery), the ability to separate and visualize likely active disease, likely response and bone marrow recovery, can enable the success of treatment to be more effectively assessed. This is particularly useful when diffuse disease is present, when morphological images are often uninformative regarding the presence and extent of therapy response.

4

Color coding of ADC ranges:

Yellow (<620 µm²/s):	likely bone marrow
Red (620-1440 µm²/s):	likely untreated disease
Green (>1440 µm²/s):	likely response

(4A) Color projection focusing on normal bone marrow: Yellow voxels cover red and green voxels.

(4B) Color projection focusing on response: Green voxels cover red and yellow voxels.

Figure 4:
ADC color projection modes. In order for color projections to be able to preferentially visualize normal marrow or likely response, the color order for the ray tracing needs to be adjusted. For ADC color projections focusing on normal bone marrow **(4A)**, the ADC-MIP displays low ADC on top (ie, yellow). For ADC-MIP color projections focusing on response **(4B)**, the ADC-MIP displays high ADC on top (green). In this case the threshold for colors are derived from the pretherapy histogram.

References

1 Woo, S., Suh, C. H., Kim, S. Y., Cho, J. Y., & Kim, S. H. (2017). Diagnostic Performance of Magnetic Resonance Imaging for the Detection of Bone Metastasis in Prostate Cancer: A Systematic Review and Meta-analysis. European Urology. doi:10.1016/j.eururo.2017.03.042.
2 Kosmin, M., Makris, A., Joshi, P. V., Ah-See, M., Woolf, D., & Padhani, A. R. (2017). The addition of whole-body magnetic resonance imaging to body computerised tomography alters treatment decisions in patients with metastatic breast cancer. European Journal of Cancer, 77, 109-116. doi:10.1016/j.ejca.2017.03.001.

Contact

Dr. Danoob Dalili
Specialist Registrar Clinical Radiology
Imperial College Healthcare NHS Trust
St Mary's Hospital
Praed St
London W2 1NY
United Kingdom
Phone: +44 (0) 20 3312 6666
Dalili@doctors.org.uk

Prof. Anwar R. Padhani
Consultant Radiologist and
Professor of Cancer Imaging
Paul Strickland Scanner Centre
Mount Vernon Cancer Centre
Rickmansworth Road
Northwood, Middlesex HA6 2RN
United Kingdom
Phone (PA): +44-(0) 1923-844751
Fax: +44-(0) 1923-844600
anwar.padhani@stricklandscanner.org.uk

3 Dimopoulos, M. A., Hillengass, J., Usmani, S., Zamagni, E., Lentzsch, S., Davies, F. E., & Terpos, E. (2015). Role of Magnetic Resonance Imaging in the Management of Patients With Multiple Myeloma: A Consensus Statement. Journal of Clinical Oncology, 33(6), 657-664. doi:10.1200/jco.2014.57.9961.
4 Padhani AR, Lecouvet FE, Tunariu N, et al. METastasis Reporting and Data System for Prostate Cancer (MET-RADS): Practical Guidelines for Acquisition, Interpretation, and Reporting of Whole-body MRI-based Evaluations of Multiorgan Involvement in Advanced Prostate Cancer. Eur Urol. 2017; 71(1):81-92.
5 Blackledge, M. D., Collins, D. J., Tunariu, N., Orton, M. R., Padhani, A. R., Leach, M. O., & Koh, D. (2014). Assessment of Treatment Response by Total Tumor Volume and Global Apparent Diffusion Coefficient Using Diffusion-Weighted MRI in Patients with Metastatic Bone Disease: A Feasibility Study. PLoS ONE, 9(4), e91779. doi:10.1371/journal.pone.0091779.
6 Blackledge, M. D., Tunariu, N., Orton, M. R., Padhani, A. R., Collins, D. J., Leach, M. O., & Koh, D. (2016). Inter- and Intra-Observer Repeatability of Quantitative Whole-Body, Diffusion-Weighted Imaging (WBDWI) in Metastatic Bone Disease. PLOS ONE, 11(4), e0153840. doi:10.1371/journal.pone.0153840.
7 Grimm R, Padhani AR. Whole-body Diffusion-weighted MR Image Analysis with *syngo.via* Frontier MR Total Tumor Load. MAGNETOM Flash (68) 2/2017, 73-75.
8 Padhani AR. Observing endocrine therapy resistance in metastatic breast cancer with whole body MRI. MAGNETOM Flash (68) 2/2017, 80-83.
9 Dalili D, Joshi P, Grimm R, Padhani AR. Evolution of the malignant bone marrow with successful therapy – quantitative analysis with whole body diffusion MRI. MAGNETOM Flash (69) 3/2017, 43–48.
10 Padhani, A. R., Van Ree, K., Collins, D. J., D'Sa, S., & Makris, A. (2013). Assessing the Relation Between Bone Marrow Signal Intensity and Apparent Diffusion Coefficient in Diffusion-Weighted MRI. American Journal of Roentgenology, 200(1), 163-170. doi:10.2214/ajr.11.8185.
11 Messiou C, Collins DJ, Morgan VA, Desouza NM. Optimising diffusion weighted MRI for imaging metastatic and myeloma bone disease and assessing reproducibility. Eur Radiol. 2011; 21(8):1713-8.

The entire editorial staff at Siemens Healthineers extends their appreciation to all the radiation oncologists, radiologists, technologists, physicists, experts, and scholars who donate their time and energy – without payment – in order to share their expertise with the readers of MAGNETOM Flash and the MReadings.

MAGNETOM Flash – Imprint

Publisher:
Siemens Healthcare GmbH
Magnetic Resonance,
Karl-Schall-Str. 6, D-91052 Erlangen, Germany

Editor-in-chief:
Antje Hellwich
(antje.hellwich@siemens-healthineers.com)

Copy Editing:
Sheila Regan, Jen Metcalf, UNIWORKS,
www.uni-works.org
(with special thanks to Kylie Martin)

Layout:
Agentur Baumgärtner,
Friedrichstr. 4, D-90762 Fürth, Germany

PrePress and Image Editing, Production:
Clemens Ulrich, Paul Linssen,
Siemens Healthcare GmbH

Printer:
Schmidl & Rotaplan Druck GmbH,
Hofer Str. 1, D-93057 Regensburg, Germany

We welcome your questions and comments about the editorial content of MAGNETOM Flash. Please contact us at magnetomworld.team@siemens-healthineers.com

Manuscripts as well as suggestions, proposals and information are always welcome; they are carefully examined and submitted to the editorial board for attention. MAGNETOM Flash is not responsible for loss, damage, or any other injury to unsolicited manuscripts or other materials. We reserve the right to edit for clarity, accuracy, and space. Include your name, address, and phone number and send to the editors, address above.

***MReadings: Prostate MRI* is also available online:**

www.magnetomworld.siemens-healthineers.com/publications/mreadings

Not for distribution in the US

On account of certain regional limitations of sales rights and service availability, we cannot guarantee that all products included in this brochure are available through the Siemens sales organization worldwide. Availability and packaging may vary by country and is subject to change without prior notice. Some/All of the features and products described herein may not be available in the United States.

The information in this document contains general technical descriptions of specifications and options as well as standard and optional features which do not always have to be present in individual cases, and which may not be commercially available in all countries.

Due to regulatory reasons their future availability cannot be guaranteed. Please contact your local Siemens organization for further details.

Siemens reserves the right to modify the design, packaging, specifications, and options described herein without prior notice. Please contact your local Siemens sales representative for the most current information.

Note: Any technical data contained in this document may vary within defined tolerances. Original images always lose a certain amount of detail when reproduced.

Siemens Healthineers Headquarters
Siemens Healthcare GmbH
Henkestr. 127
91052 Erlangen, Germany
Phone: +49 9131 84-0
siemens-healthineers.com

Published by Siemens Healthcare GmbH · Order No. A91MR-1000-137C-7600 · Printed in Germany · 13606 0523 · ©Siemens Healthcare GmbH, 2023

siemens-healthineers.com/magnetom-world